

**SOLUTION CRYSTALLIZATION OF
POLYCARBONATE SURFACES: DUST REMOVAL
FOR SELF CLEANING APPLICATIONS**

BY

[SAEED BAHATAB]

A Thesis Presented to the
DEANSHIP OF GRADUATE STUDIES

KING FAHD UNIVERSITY OF PETROLEUM & MINERALS

DHAHRAN, SAUDI ARABIA

In Partial Fulfillment of the
Requirements for the Degree of

MASTER OF SCIENCE

In

MECHANICAL ENGINEERING

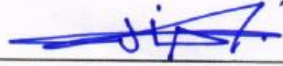
DECEMBER, 2021

KING FAHD UNIVERSITY OF PETROLEUM & MINERALS

DHAHRAN- 31261, SAUDI ARABIA

DEANSHIP OF GRADUATE STUDIES

This thesis, written by Saeed Abobakr Bahatab under the direction of his thesis advisor and approved by his thesis committee, has been presented and accepted by the Dean of Graduate Studies, in partial fulfillment of the requirements for the degree of **MASTER OF SCIENCE IN MECHANICAL ENGINEERING.**

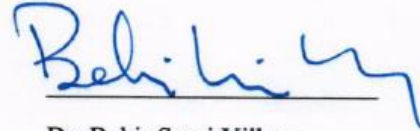


Dr. Khaled Al-Athel
Department Chairman



Dr. Suliman Saleh Al-Homidan
Dean of Graduate Studies

19/12/2021



Dr. Bekir Sami Yilbas
(Advisor)



Dr. Ahmet Z. Sahin
(Member)



Dr. Hussain Al-Qahtani
(Member)



© Saeed Bahatab

2021

This work is dedicated to all the people who took part in my journey and helped me develop to this degree; my parents and family members for standing behind me and pushing me to continue my journey, my thesis advisor Dr. Bekir Sami Yilbas for his understanding and fatherly treatment which helped me through some of the worst times of my life and Dr. Abdullah Al-Sharafi for his brotherly support and encouragement.

ACKNOWLEDGMENTS

This work came about with the support and aid of many people who contributed to the production of this Thesis. I would like to thank Allah who gave me the health and strength to achieve my goal and finish my work. I would, also, like to thank King Fahd University of Petroleum and Minerals which provided me with the research facilities to complete this Thesis. Acknowledgment is further extended to the financial support received from the Deanship of Scientific Research at King Fahd University of Petroleum and Minerals (KFUPM) and King Abdullah City for Atomic and Renewable Energy (K.A. CARE) to accomplish this work.

Deep gratitude is extended to my thesis advisor Dr. Bekir Sami Yilbas for his guidance and support in accomplishing this work. I would also Like to recognize the role of my committee members, Dr. Ahmet Z. Sahin and Dr. Hussain Al-Qahtani, for their advice and assistance. Acknowledgment is, further, extended to Dr. Abba Abobakr and Dr. Ghassan Hasan for their advice and assistance.

Finally, I wish to thank all faculty and staff members of the Mechanical Engineering Department at KFUPM.

TABLE OF CONTENTS

ACKNOWLEDGMENTS	V
TABLE OF CONTENTS	VI
LIST OF TABLES	IX
LIST OF FIGURES	X
LIST OF ABBREVIATIONS	XV
ABSTRACT	XX
ملخص الرسالة	XXII
CHAPTER 1 INTRODUCTION	1
1.1 Background	3
1.1.1 Sand and Dust Storms	3
1.1.2 Dust Accumulation and Cleaning Methods	4
1.1.3 Hydrophobicity	6
1.2 Problem Statement	8
1.3 Motivation	9
1.4 Objectives	10
1.5 Significance	10
1.6 Scope and Limitations	11
CHAPTER 2 LITERATURE REVIEW	13
2.1 Effect of Dust on PV Panels	13
2.1.1 Sand and Dust Storm (SDS) Formation	13
2.1.2 Characteristics of Accumulated Dust on a PV panel.....	21
2.2 PV Degradation	27

2.3	Dust Cleaning Methods	35
2.4	Dust Removal by Self-Cleaning Methods	38
2.4.1	Hydrophobic Surfaces	39
2.4.2	Analysis of Dust Adhesion on Hydrophilic and Hydrophobic Surfaces:.....	40
2.4.3	Free Surface Energy and Adhesion.....	43
2.4.4	Surface Free Energy Calculations	44
2.5	Establishment of Problem	47
 CHAPTER 3 RESEARCH METHODOLOGY		49
3.1	Apparatuses	49
3.1.1	Cutting Machine	50
3.1.2	Grinding Machine	50
3.1.3	SEM Field Emission –Scanning Electron Microscopy (FE-SEM)	50
3.1.4	Mechanical Pipette.....	51
3.1.5	X-Ray Diffraction (XRD)	51
3.1.6	Fourier-Transform Infrared Spectroscopy (FTIR)	51
3.1.7	Goniometer	52
3.1.8	3D Optical Microscope	52
3.1.9	UV Transmittance.....	52
3.1.10	High-Speed Camera	53
3.1.11	Computational Facility.....	54
3.2	Experimental Procedures	54
3.2.1	Sample Preparation.....	54
3.2.2	Crystallization of PC Surface.....	55
3.2.3	Surface Characteristics	57
3.2.4	Dust Picking Mechanisms.....	58
3.2.5	Poly-di-methyl-siloxane (PDMS) Replication of Crystallized Surfaces.....	60
3.2.6	Silicone Impregnated Surfaces	62
 CHAPTER 4 FORMULATION OF SLIDING DROPLET		64
4.1	Numerical Analysis	64
4.1.1	Initial conditions.....	65
4.1.2	Boundary conditions	65
4.1.3	Flow Equations	66
4.2	Numerical Implementation	68
4.3	Analytical Treatment	71
4.3.1	Force Analysis.....	71
4.3.2	Velocity Analysis.....	72
4.3.3	Energy Analysis.....	74

CHAPTER 5 RESULTS AND DISCUSSION	78
5.1 Silicone Oil Impregnation	78
5.1.1 Silicone Oil Impregnation of Crystallized PC Surface	78
5.1.2 Numerical Findings	84
5.2 Mitigation of Dust Particles	96
5.2.1 Crystallized Polycarbonate Surface and Dust Properties	96
5.2.2 Cloaking Procedure of Oil and Water over Dust Particles.....	101
5.2.3 Oil Film Thickness Influence	107
5.3 Carbonated Water Droplet on Dusty Hydrophobic Surface	115
5.3.1 Properties of Hydrophobized Glass Surface and Dust Particles	115
5.3.2 Cloaking Procedure for Carbonated Water	120
5.3.3 Bubble Behaviour Inside Water Droplet.....	122
5.3.4 Effect of Carbonated Water on Dust Removal from the Surface	132
CHAPTER 6 CONCLUSIONS	142
6.1 Dynamics of a Water Droplet on Silicone Oil Film Surfaces	142
6.2 Sliding Water Droplet on Oil Impregnated Surface and Dust Particle Mitigation	143
6.3 Carbonated Water Droplet on Dusty Hydrophobic Surfaces	145
6.4 Future Work	147
REFERENCES	148
VITAE	174

LIST OF TABLES

Table 1 The dust accumulation rate (DAR) on the deposited surface for various environmental conditions [19], [20], [22]–[25], [43], [98]–[100].....	24
Table 2 Acetone Technical Data Sheet.....	56
Table 3 Properties of silicone oil and water used in the computation	68
Table 4 Comparison of velocity field obtained from experiments and simulations for 40 μ L and droplet location of 32 mm from the edge.	89
Table 5 Elemental constitute of dust particles (wt%). Increasing dust particle size causes reduction in alkaline earth metal (Ca) and silicone (Si); however, alkaline metals (Na and K) and chlorine (Cl).....	100
Table 6 Elemental composition of dust particles (wt%).....	118
Table 7 Lifshitz-van der Walls components and electron-donor parameters used in the simulation [185], [186], [189]	118

LIST OF FIGURES

Figure 1 Energy Consumption by Source in the World [11]	2
Figure 2 Global Dust Potential Map [29]	4
Figure 3 Surface Dust Concentration [30]	4
Figure 4 Causes of Dust Accumulation on a PV Surface [33]	5
Figure 5 Categorization of Surface Hydrophobicity [37]	6
Figure 6 The various processes of particle transportation via wind [55].....	15
Figure 7 The physical processes which influence dust emission, transport, and deposition [58]	17
Figure 8 The characteristics of dust accumulation rate (DAR) for a specific exposure period: a) decreasing trend of DAR for increasing exposure periods, b) increasing dust load for increasing exposure periods, c) the DAR and corresponding environmental variation for daily measurements during the winter and summer [98]	25
Figure 9 The chemical composition of the accumulated dust in Doha [98]	26
Figure 10 Surface layers of the soil of accumulated dust on the deposited surface [124]	31
Figure 11 The uniform distribution of the various sizes of dust particles and its effect on a) optical transmittance and b) solar intensity [93]	33
Figure 12 Dust removal techniques from the solar application [127].	35
Figure 13 Electric curtain: a) Three-phase electric curtain and b) The electrical field distribution between the electrodes of the shield [132]	38
Figure 14 Cleaning behavior by a water droplet on the hydrophobic and hydrophilic surface [128].	41
Figure 15 Attachment of plastic sphere particle with the solid surface [144]	42
Figure 16 The work of adhesion during contact interface separation [146]	44
Figure 17 Diagram of surface energy on water contact angle [147].....	45

Figure 18 The wetting of rough structured surface: a) Wenzel’s model b) Cassie-Baxter model [149].....	47
Figure 19 Demonstration of the experimental set-up	60
Figure 20 Poly-di-methyl-siloxane (PDMS) replication through the liquid casting technique	61
Figure 21 View of sliding droplet on an inclined impregnated oil film. The boundary conditions as marked 1 to 5.....	66
Figure 22 Meshes used in the simulations: a) mesh distribution in three-dimensional feature, b) mesh distribution at droplet and oil film sections, and c) mesh distribution in the oil rim and water droplet surrounding region	69
Figure 23 Grid independent test results along y-direction at $x = 0.25$ mm away from droplet centerline for different mesh sizes: a) velocity distribution, and b) pressure variation	70
Figure 24 Scanning electron microscopy (SEM) and atomic force microscope (AFM) images and line scan of the crystallized polycarbonate surface: a) SEM image of various sizes of spherules, b) SEM image of fibrils and spherules, c) AFM image of the surface, and c) AFM line scan over the surface	79
Figure 25 Optical transmittance of polycarbonate, crystallized polycarbonate, and silicone oil-impregnated crystallized polycarbonate samples	82
Figure 26 Optical image of sliding water droplet and silicone film. Red shows the sliding direction of the water droplet. The inclination angle of the sample is 40° , droplet volume is $30 \mu\text{L}$, and the location of the droplet is 25 mm away from sliding initiation on an oil film.....	83
Figure 27 Droplet velocity on impregnated oil film for different droplet volumes. The distance of zero represents the droplet start of sliding on the silicone oil film	85
Figure 28 Comparison of droplet translational velocity as obtained from both experiment and simulations. The distance of zero represents the droplet start of sliding on the silicone oil film.....	85
Figure 29 Droplet rim diameter (diameter on oil film) for different droplet volumes. The distance of zero represents the droplet start of sliding on the silicone oil film	87

Figure 30 Oil film ridge height in the front side (right ridge) and backside (left ridge) of water droplet for different droplet volumes	88
Figure 31 3-dimensional simulation of water droplet velocity on oil film: a) velocity in droplet and film, b) velocity in oil film and c) velocity in the water droplet. Since the maximum velocity magnitude in oil film and droplet are different, they are shown separately to observe flow velocities.....	90
Figure 32 Velocity magnitude over the symmetry plane in water droplet and oil film. The inclination angle of the sample is 40° , the droplet volume is $40 \mu\text{L}$, and the droplet location is at the droplet initial sliding site (i.e. 24 mm from the edge). Since the maximum velocity magnitude in oil film and droplet are different, they are shown separately to observe flow velocities. Simulations are carried out in one solution domain	91
Figure 33 Velocity magnitude over the symmetry plane in the water droplet and oil film. The inclination angle of the sample is 40° , the droplet volume is $40 \mu\text{L}$, and the droplet location is 8 mm from the droplet initial sliding site (i.e. 32 mm from the edge). Since the maximum velocity magnitude in oil film and droplet are different, they are shown separately to observe flow velocities. Simulations are carried out in one solution domain	92
Figure 34 Velocity magnitude over the symmetry plane in the water droplet and oil film. The inclination angle of the sample is 40° , the droplet volume is $40 \mu\text{L}$, and the droplet location is 16 mm from the droplet initial sliding site (i.e. 40 mm from the edge). Since the maximum velocity magnitude in oil film and droplet are different, they are shown separately to observe flow velocities. Simulations are carried out in one solution domain	93
Figure 35 SEM images of crystallized surface: a) micro size spherules, which represent the crystallized structures. Increasing acetone concentration or immersion duration, micro-size spherules become congested while lowering surface contact angle considerably and b) fibrils on spherules (in the red dotted circle). Fibrils are formed from the crystallized sites and they create the Lotus effect reducing contact angle hysteresis.....	98
Figure 36 AFM surface image and line scan: a) micro-image of the surface. The small bright spots represent the spherules and brightness is related to the height of the spherules (brighter the spot corresponds to higher the spherules), and b) line scan, which is taken over the crystallized surface. It is shown as a green line in Figure 36a. It provides information on the	

heigh of the spherules	99
Figure 37 Optical transmittance of untreated, crystallized, and crystallized-oil impregnated polycarbonate. Spherules and fibrils on the crystallized surface cause diffuse reflection and partial absorption of incident UV visible radiation while lowering specular transmittance (wavelength-dependent transmittance). The increasing wavelength of incident optical radiation lowers diffuse reflection and absorption from the crystallized surface	99
Figure 38 SEM Micro-image of dust particles. Dust particles have various shapes and sizes. Small dust particles adhere to large size particles forming clustering-like structures as shown in the red dotted circle. The attachment of small particles demonstrates that these particles have increased polar forces	101
Figure 39 Optical image of dust particle: a) before oil infusion and b) after oil infusion. Infused oil totally covers the dust particle surface, which indicates the positive spreading coefficient of oil over the particle surface ..	105
Figure 40 Infusion height and infusion velocity with time: a) water, and b) silicone oil. h represents infusion height on dust surface and V is the infusion velocity	106
Figure 41 Optical image of silicone oil infusion on water droplets at different times. The time of droplet motion is started and recorded as the droplet is dispensed on the oil-impregnated sample surface	107
Figure 42 Droplet sliding velocity on the inclined oil-impregnated surface for two droplet volume and inclination angles. Oil film thickness is 50 μm	109
Figure 43 Droplet sliding velocity on the inclined oil-impregnated surface for two droplet volume and inclination angles. Oil film thickness is 700 μm	110
Figure 44 Droplet sliding velocity on the inclined oil-impregnated surface with the large dust particle presence for two droplet volumes and tilting angles. Oil film thickness is 50 μm	112
Figure 45 Droplet sliding velocity on the inclined oil-impregnated surface with large dust particle presence for two droplet volumes and tilting angles. Oil film thickness is 700 μm	113
Figure 46 Stages of the droplet on inclined oil film for two oil film thicknesses. The dark color represents the dust particle	114

Figure 47 SEM micrograph and AFM line scan of functionalized silica particles deposited surface: a) SEM micrograph and b) AFM line scan	116
Figure 48 SEM micrograph and size distribution of dust particles: a) SEM micrograph showing various shapes and sizes of dust particles, b) SEM micrograph of dust particles showing small dust particles attachment at large particle surfaces, and c) size distribution of dust particles.....	119
Figure 49 X-ray diffractogram of dust particles	120
Figure 50 Distilled and carbonated water cloaking velocity and cloaking height on dust particle surface with time	122
Figure 51 Bubble velocity inside the droplet predicted from analytical formulation and obtained from experiment for various droplet sizes	130
Figure 52 High-speed camera images of 40 μ L bursting bubble: a) Foam-like bubbles formed in the top region of the droplet, b) large bubble is formation, c) bursting of the large bubble, and d) droplet after large bubble bursting	131
Figure 53 High-speed camera images of bubbles formed around dust particle and reorientation of dust particle due to bubble size and number changing with time on the dust particle surface.....	133
Figure 54 Volume ratio of dust particles inside the droplet. Volume ratio represents total volume occupied by dust particles in the upper part of carbonated water droplet over total volume occupied by dust particles in the upper part of the distilled water droplet	135
Figure 55 High-speed camera images of dust particles inside droplet: a) carbonated water droplet, and b) distilled water droplet.....	136
Figure 56 Bubble velocity with time for different droplet volumes: a) on dusty hydrophobic surfaces, and b) on the clean hydrophobic surface	139
Figure 57 Bubble diameter inside droplet with time for different droplet volumes: a) on dusty hydrophobic surfaces and b) on the clean hydrophobic surface..	140
Figure 58 Dust particle velocity inside droplet with time for different carbonated and distilled water droplet volumes.....	141

LIST OF ABBREVIATIONS

PC	:	Polycarbonate
PV	:	Photovoltaic
SEM	:	Scanning electron microscope
XRD	:	X-Ray Diffraction
SEM	:	Scanning electron microscope
FTIR	:	Fourier-transform infrared spectroscopy
PDMS	:	Poly-di-methyl-siloxane
VOF	:	Volume of fluid
2D	:	Two-dimensional
3D	:	Three-dimensional
SDS	:	Sand and Dust Storms
MENA	:	Middle East and North Africa
CA	:	Contact Angle
DAR	:	The Dust accumulation rate
DC	:	Dirt correction factor
UV	:	Ultraviolet
PET	:	polyethylene terephthalate
fps	:	frame per second
ALE	:	Arbitrary Lagrangian-Eulerian
Ca	:	Calcium
Na	:	Sodium
K	:	Potassium
Cl	:	Chlorine

S	:	Sulfur
Fe	:	Iron
Mg	:	Magnesium
O	:	Oxygen
NaCl	:	Sodium Chloride
KCl	:	Potassium Chloride
CaSO₄	:	Calcium Sulfate
Fe₂O₃	:	Ferric Oxide

Symbol	:	Definition	:	Unit
γ_{LV}	:	Surface tension	:	N/m
γ_{SL}	:	Interfacial energy	:	N/m
γ_{SV}	:	Surface free energy	:	N/m
R	:	Droplet radius	:	m
m	:	Droplet mass	:	kg
E''_{ad}	:	Surface adhesion energy	:	Nm
A_{wet}	:	Wetted area	:	m ²
h	:	Height of center of mass	:	m
α	:	Inclination angle	:	o
g	:	Gravitational acceleration	:	m/s ²
F_{ad}	:	Adhesion force	:	N
F	:	Friction force	:	N
ϕ	:	Wedge angle	:	Degrees
V	:	Droplet volume	:	m ³
v	:	Velocity	:	m/s
a	:	Acceleration	:	m/s ²
I	:	Moment of inertia	:	kgm ²

t	:	Time	:	s
θ_A	:	Advancing contact angle	:	Degrees
θ_R	:	Receding contact angle	:	Degrees
μ_1	:	Dynamic viscosity of air	:	Pa.s
μ_2	:	Dynamic viscosity of water	:	Pa.s
σ	:	The surface tension of water	:	N/m
φ	:	Level set function	:	-
ϵ_{ls}	:	Interfacial thickness parameter	:	m
γ	:	Re-initialization parameter	:	: m/s
θ_w	:	The contact angle of the wetted wall	:	Degrees
α	:	Contact Angle	:	Degrees
θ_c	:	Filling Angle	:	Degrees
δ	:	Inclination Angle	:	Degrees
σ_u	:	the standard uncertainty	:	%
ρ	:	Density	:	kg/m ³
u	:	Velocity	:	m/s
g	:	Gravity Acceleration	:	m/s ²
μ	:	Viscosity	:	Pa.s
F_g	:	Gravitational Force	:	N
F_b	:	Buoyancy Force	:	N
V_{disp}	:	Displaced Volume of the Oil	:	m ³
V_d	:	Droplet Volume	:	m ³
ϕ	:	Solid Fraction	:	-
h_t	:	Film Thickness	:	m
F_{st}	:	Surface tension force	:	N
S	:	Spreading Rate	:	N/m
h_o	:	Cap Height	:	m
r_o	:	Cap Radius	:	m

r_d	:	Droplet Radius	:	-
h_t	:	Film Thickness	:	m
F_{st}	:	Surface tension force	:	N
F_γ	:	The force of Surface Tension	:	N
W	:	Droplet Weight Force	:	N
Ca	:	Capillary Number	:	-
b	:	Slip Length	:	m
u_s	:	Slip Velocity	:	m/s
τ	:	Shear Stress	:	N/m ²
u_f	:	Film Velocity	:	m/s
V_d	:	Droplet Velocity	:	m/s
l_m	:	Distance of Base to Centre of Mass	:	m
E_d	:	Energy Dissipated	:	J/s
r_b	:	Immerse Liquid's Droplet Radius	:	m
l_{rid}	:	Ridge Height	:	m
E_k	:	Kinetic Energy	:	J/s
V_{inf}	:	Infusion Velocity	:	m/s
Oh	:	Ohnesorge Number	:	-
Ca	:	Capillary Number	:	-
C_d	:	Drag Coefficient	:	-
C_s	:	Saturation Concentration	:	%
K_H	:	Henry's Constant	:	-
P_g	:	Gas Partial Pressure	:	Pa
J	:	Desorb Gaseous Flux	:	kg/s
D	:	Diffusion Coefficient	:	-
Λ	:	Ostwald	:	-
P_o	:	Ambient Pressure	:	Pa
P_L	:	Liquid Partial Pressure	:	Pa

Re	:	Reynolds Number	:	-
Bo	:	Bond Number	:	-
Mo	:	Morton Number	:	-
S_c	:	Schmidt Number	:	-
$\frac{dR}{dt}$:	Rate of Bubble Growth	:	m/s
κ	:	Capillary Length	:	m
h/h_o	:	Bubble Film Thinning	:	-
φ	:	Evaporation Coefficient	:	-
x	:	Humidity Ratio of Air	:	%
x_s	:	Humidity Ratio of Saturated Air	:	%
D	:	Diffusion Coefficient	:	-

ABSTRACT

Full Name : [Saeed Abobakr Bahatab]

Thesis Title : [Solution Crystallization of Polycarbonate Surfaces: Dust Removal for Self-Cleaning Applications]

Major Field : [Mechanical Engineering]

Date of Degree : [December 2021]

Climate change causes dust storms with increased frequency. Environmental dust has considerable influence on the performance of devices used in different sectors such as Photo Voltaic and Concentrated Power in the solar energy sector. Although several methods are introduced for dust removal from surfaces, self-cleaning becomes one of the favorable methods. In self-cleaning applications, surface hydrophobicity becomes a necessary condition. In the present thesis, the one-step method is introduced to hydrophobized transparent polycarbonate surfaces. In the process, an immersion technique incorporating acetone with different concentrations is used. The process results in a surface texture composed of various sizes of spherules and fibrils. Since the spherules heights extend within $10\ \mu\text{m} - 15\ \mu\text{m}$ with spacing of a similar order, the texture surface morphology possessed a hydrophobic wetting state with the average droplet contact angle in the range of 135° to 150° with the hysteresis of about 26° . The high hysteresis suppresses the water droplet mobility on the resulting textured surfaces even though the fibrils create a Lotus effect. In addition, UV visible transmittance tests reveal that the optical transmittance of the textured surface reduces considerably. To improve the water droplet mobility and optical transmittance of the textured surfaces, the

silicone oil film with different thicknesses is created over the surface. The droplet mobility (sliding motion) and optical transmittance of the resulting surface are examined. The findings reveal that the droplet mobility, in terms of sliding, and optical transmittance improve significantly. During the droplet sliding tests, a high-speed recording facility and a tracker program are used to quantify the sliding velocity and oil film cloaking of the droplet surface. Since silicone oil spreads over the droplet liquid (water), the silicone cloaking is resulted in partially covering the droplet surface, which creates an adverse effect on the sliding speed. The dust mitigation from the oil film by the sliding droplet is also examined. The findings reveal that the sliding droplet liquid cloaks the dust particles and successfully mitigates them from the oil film.

ملخص الرسالة

الاسم الكامل: سعيد أبوبكر باحطاب

عنوان الرسالة: بلورة المحلول لأسطح البولي كربونات: إزالة الغبار لتطبيقات التنظيف الذاتي

التخصص: الهندسة الميكانيكية

تاريخ الدرجة العلمية: ديسمبر، 2021

يتسبب تغير المناخ في حدوث عواصف ترابية بوتيرة متزايدة. للغبار البيئي تأثير كبير على أداء الأجهزة المستخدمة في مختلف القطاعات مثل الطاقة الفولتية الضوئية والطاقة المركزة في قطاع الطاقة الشمسية. على الرغم من إدخال عدة طرق لإزالة الغبار من الأسطح، فإن التنظيف الذاتي أصبح إحدى الطرق المفضلة. في تطبيقات التنظيف الذاتي، تصبح مقاومة الماء السطحي شرطاً ضرورياً. في الأطروحة الحالية، يتم تقديم طريقة الخطوة الواحدة لأسطح البولي كربونات الشفافة الطاردة للماء. في هذه العملية، يتم استخدام تقنية غمر تشتمل على الأستون بتركيزات مختلفة. ينتج عن العملية نسيج سطحي يتكون من أحجام مختلفة من الكرات والألياف. نظراً لأن ارتفاعات الكرات تمتد في حدود 10-15 ميكرومتر مع تباعد من نفس الترتيب، فإن شكل سطح النسيج يمتلك حالة ترطيب كارهة للماء بمتوسط زاوية ملامسة للقطيرات في النطاق من 135 درجة إلى 150 درجة مع التباطؤ إذا كان حوالي 26 درجة. يمنع التباطؤ العالي حركة قطرات الماء على الأسطح المنسوجة الناتجة على الرغم من أن الألياف تخلق تأثير اللوتس. بالإضافة إلى ذلك، تكشف اختبارات النفاذية المرئية للأشعة فوق البنفسجية أن النفاذية الضوئية للسطح المحكم تنخفض بشكل كبير. لتحسين حركة قطرات الماء والنفاذية البصرية للأسطح المنسوجة، يتم إنشاء فيلم زيت السيليكون بسماكات مختلفة على السطح. يتم فحص حركة القطيرات (الحركة المنزلة) والنفاذية الضوئية للسطح الناتج. تكشف النتائج أن حركة القطيرات، من حيث الانزلاق، والنفاذية الضوئية تتحسن بشكل كبير. أثناء اختبارات انزلاق القطرات، يتم استخدام مرفق تسجيل عالي السرعة وبرنامج تعقب لتحديد سرعة الانزلاق وإخفاء طبقة الزيت على سطح القطرة. نظراً لأن زيت السيليكون ينتشر فوق سائل القطرة (الماء)، ينتج عن إخفاء السيليكون تغطية سطح القطرة جزئياً، مما يؤدي إلى حدوث تأثير سلبي على سرعة الانزلاق. يتم أيضاً فحص تخفيف الغبار من فيلم

الزيت بواسطة القطرة المنزلة. تكشف النتائج أن السائل المنزلق للقطرة يخفي جزيئات الغبار ويخففها بنجاح من فيلم الزيت.

CHAPTER 1

INTRODUCTION

Energy consumption around the world is continuously rising every year. Traditional fossil fuels, such as Coal, gas, and oil, are currently considered the main method of energy generation and responsible for most of the world's requirements according to a statistical study performed by BP plc (The British Petroleum Company plc) [1]. The consumption of energy in the world is illustrated in Figure 1. However, the negative environmental impact of fossil fuels, which include their role in climate change and global warming, along with the increase in fuel prices prompted the rapid growth in renewable energy production [2]. Renewable energy can be mainly categorized under Hydropower, nuclear, wind, solar, biomass, geothermal, and waste energy. The enormous price decline of 60% in the PV cost which was recorded in the period between 2008 and 2011 prompted the solar PV technology to experience the highest growth in the renewable energy sector [3].

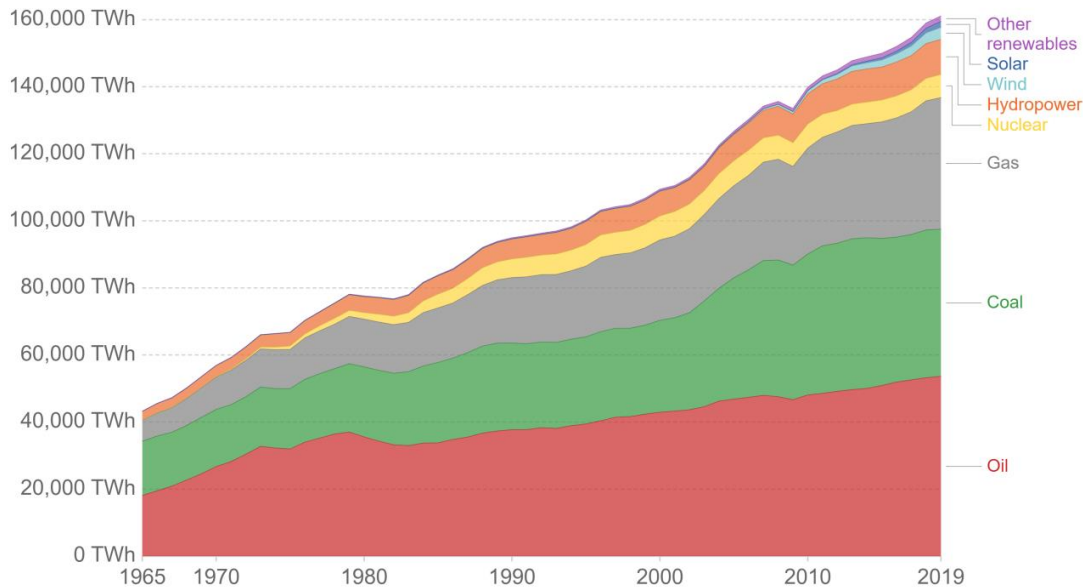
The presence of dust around the world is increasing in frequency. This is more evident in the Middle East and North Africa where the likelihood of encountering dust storms becomes increasingly high. The appearance of dust in the environment can limit the performance of solar energy panels as it can limit the amount of incident solar energy which can reach the panels. The dust stagnant on the surface of the panel can degrade both the efficiency and power output of the solar energy panels [4]. Furthermore, solar power plants are usually implemented in desert areas where vast open lands with open

areas exist which are available for low economical values. These areas are prone to have a dominant dusty environment.

Maintaining a clean surface under harsh environments becomes a requirement for improving the efficiency of solar energy harvesting. Although traditional methods can be utilized to solve this issue, they tend to waste energy, resources, or both. Attaining self-cleaning surfaces can help minimize such wastes. This endeavor can be realized by mimicking the way of nature in creatures that can self-clean their surfaces. Such creatures include red rose petals, lotus leaves, rice leaves, butterfly wings, and fish scales [5-9]. These creatures utilize the hydrophobic property which is essential for self-cleaning surfaces [10].

Energy consumption by source, World

Primary energy consumption is measured in terawatt-hours (TWh). Here an inefficiency factor (the 'substitution' method) has been applied for fossil fuels, meaning the shares by each energy source give a better approximation of final energy consumption.



Source: BP Statistical Review of World Energy
Note: 'Other renewables' includes geothermal, biomass and waste energy.

OurWorldInData.org/energy • CC BY

Figure 1 Energy Consumption by Source in the World [11]

1.1 Background

1.1.1 Sand and Dust Storms

Arid regions, where desert areas are common, witness the meteorological phenomenon known as sand and/or dust storm (SDS). Strong winds can help dust particles that are loosely attached to dry surfaces to travel from one place to another [12]. Sand storms usually refer to desert storms where the dominant soil type contained in those storms is sand whereas finer dust particles, dirt, and rocks are less prevalent. Dust storms are generally referring to finer particles being blown for a long-distance [13]. SDS's negative impact can disturb both the residents and their economy. These impacts include desertification, reduced visibility which in turn affects the methods of transportation, difficulty in breathing, and limited sunlight reaching the surface [14]. Black Sunday, the worst day in the Dust Bowl era where the day turned into the night due to the 20 dust storms which befell the US on 14th April 1935 causing enormous losses where 31 people were killed and more than 2,000 became homeless following the aftermath of that day [15].

The Middle East is considered as one of the worst areas to be plunged by SDS, where approximately 60 dust storms transpired between 2003 and 2011 [16]. The Middle East and North Africa (MENA) are continuously suffering due to the environmental issue of climate change where those regions are moving closer to desertification. Desertification is mainly caused by the increasing temperature influenced by global warming, lack of rainfall, or inappropriate agriculture which will ultimately lead to the conversion of

agricultural land into the desert area [17-28]. The global dust potential and dust concentration maps are shown in Figure 2 and Figure 3 respectively.

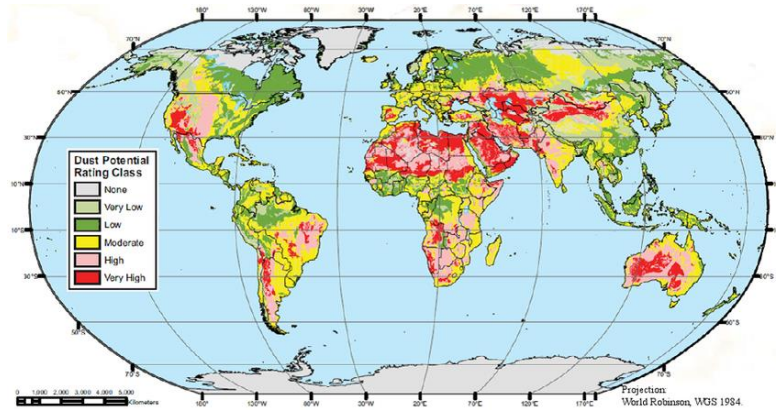


Figure 2 Global Dust Potential Map [29]

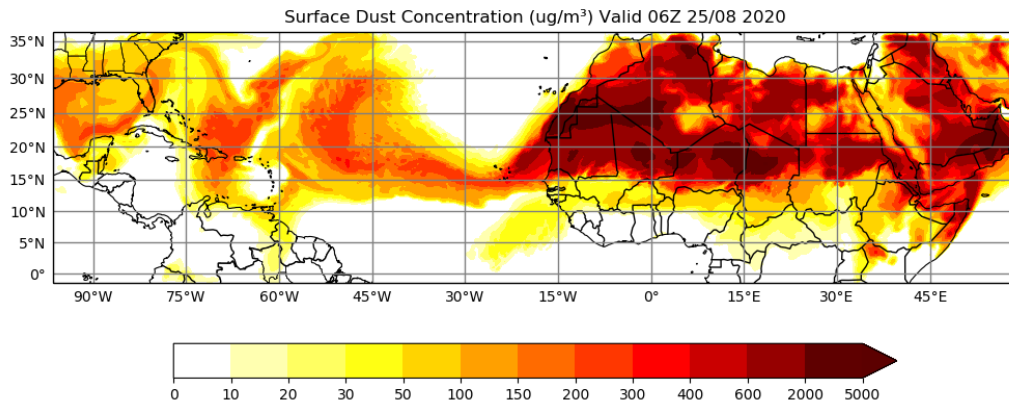


Figure 3 Surface Dust Concentration [30]

1.1.2 Dust Accumulation and Cleaning Methods

The classification of soiling accumulation depends on the local environment and the dust properties and surface characteristics. The local environment is a major contributor to the accumulation of soil where the movement of the wind, changes in the weather, or the presence of natural disasters can affect the state of dust accumulation on the surface. Dust properties such as size, weight, shape, and components can become contributing factors

in this process. Greater weight will increase the difficulty for the wind to push the dust outside the surface. Dust particles comprised of different components lead to different surface energy which affects their adhesion to the surface. The surface material, nano-texture, and alignment are factors that can influence the dust accumulation on top of the surface. Nevertheless, the three main parameters are slightly interdependent as described in Figure 4 [31-32].

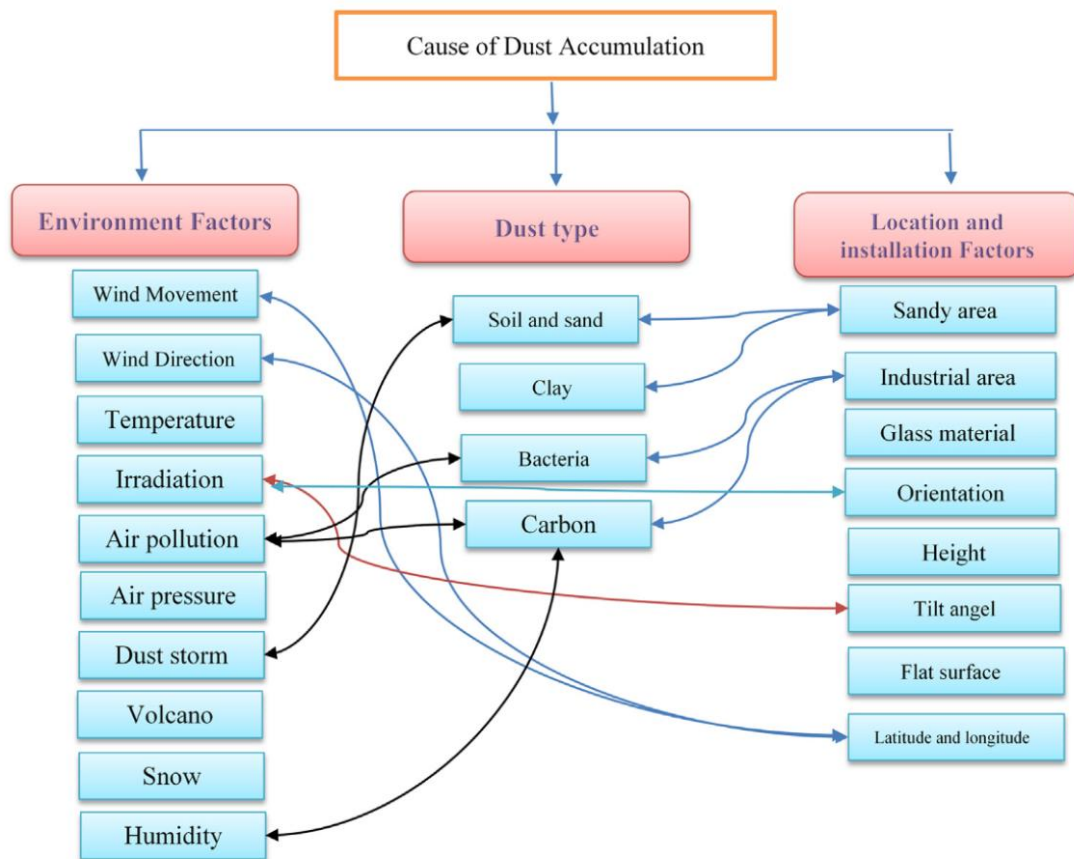


Figure 4 Causes of Dust Accumulation on a PV Surface [33]

The accumulation of dust can seriously degrade the power outcome from the PV panel. Therefore, cleaning methods became an essential part of the PV solar power operating system. The cleaning methods can be mainly classified as passive and active methods.

Active methods require some sort of energy input or resource whether it's the use of a traditional mop, mechanical robot, steam, compressed air, pressurized water, or electrostatic force to perform the cleaning. Passive methods include the reliance on weather conditions such as rain or strong winds to remove dust from the surface or designing a surface texture with a self-cleaning ability utilizing the super-hydrophobic and super-hydrophilic principle to maintain a clean surface [34].

1.1.3 Hydrophobicity

Hydrophobicity is the physical property that doesn't allow a molecule to interact with water [35]. Examples of hydrophobic molecules include alkanes, oils, fats, and nonpolar covalent compounds [36]. A hydrophobic surface is a low surface energy surface that has the ability to repel water. The characteristics of such surface can be recognized through the low surface free energy and the surface texture which is comprised of micro/nano pillars [10]. A surface can be categorized in terms of hydrophobicity into four types depending on the Contact Angle (CA) of a water droplet positioned on the surface. Super-hydrophilic, hydrophilic, hydrophobic, super-hydrophobic surfaces have $\theta < 5^\circ$, $\theta < 90^\circ$, $\theta = 90^\circ - 150^\circ$ and $\theta = 150^\circ - 180^\circ$ CA respectively as demonstrated in Figure 5 [37].

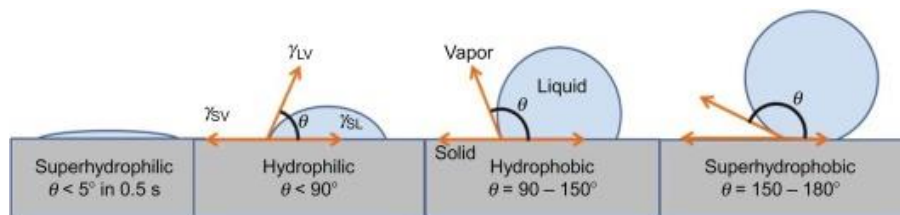


Figure 5 Categorization of Surface Hydrophobicity [37]

Improving the hydrophobicity of a surface can be achieved through physical and chemical reactions which can modify the surface energy of the surface. A variety of methods can be utilized to develop these reactions which are associated with multi-step procedures. These procedures are typically involved with high cost, specialized reagents, and harsh conditions [38-47]. Examples of such methods include phase separation, laser texturing, electrochemical deposition, electrospinning, and solution immersion [38-47]. Utilizing a one-step process to modify the surface texture of a surface is cost-efficient. However, such a process proves to be challenging and requires further research in surface engineering to improve both the process and the resultant characteristics of the produced surface [48].

A one-step method to generate a hydrophobic surface can be achieved by immersing a Polycarbonate (PC) wafer in an Acetone solution. PC is more equipped to handle extremely harsh environments in comparison with glass. PC has high impact resistance, good optical transmittance in visible light, and a low modulus of elasticity [49-52]. Utilizing this method can give PC wafers the hydrophobic property; however, it can also reduce its optical transmittance to a nearly opaque level. This reduction comes as a result of the molecular distortion and optical scattering of the produced surface [46].

Countering this issue can be done via utilizing different solutions. One such solution is to utilize Polydimethylsiloxane (PDMS) in the liquid casting method. PDMS is a silicone-based organic polymer that can be used to copy and reproduce textured wafer surfaces. PDMS is optically clear, non-toxic, and non-flammable. The properties of the PDMS in the liquid form which is used to copy the surface texture can help elevate the optical transmittance and counter the issue in the produced PC wafer. The usage of PDMS has

been viewed in previous studies [48]. However, the process required to reproduce a geometrically complicated surface, such as the acetone-treated PC wafer, requires further investigation. In addition, silicone oil impregnation of PDMS replicated surfaces towards achieving high optical transmittance is one of the challenging problems in self-cleaning applications.

1.2 Problem Statement

Hydrophobic surfaces can be utilized to clean the dust more efficiently. Generating a hydrophobic surface can be achieved through a variety of methods. Generally, the procedure to produce hydrophobic surface results in a reduction of its optical transmittance. In the case of PC crystallization, the optical transmittance falls to a near opaque level.

Utilizing a self-cleaning surface can be vital to the field of renewable energy, especially in cleaning PV panels. The issue of the degrading optical transmittance becomes critical for the PV panel's efficiency. Through the utilization of different procedures, this optical transmittance can be improved. Replicating the Hydrophobic surface using PDMS is one method that can be used to enhance this property. Utilizing silicone oil can be another method to achieve this objective.

The changes brought to the properties of the hydrophobic surfaces due to this enhancement need to be analyzed to assess the value of the produced surface. Therefore, the surface characteristics, such as the surface texture, CA, and optical transmittance, of

these surfaces need to be studied. Droplet behavior while collecting dust over the various surfaces and the effect of residual dust on the surface requires some attention as well.

1.3 Motivation

The accumulation of dust on top of PV panels is a major problem for the efficiency of solar power harvesting. PV solar systems are mainly implemented in desert areas where the dusty climate is dominant. The accumulated dust on the PV panel can limit the amount of incident solar energy which can reach the panels. Consequently, the efficiency and power output of the solar energy panels will be degraded. Cleaning the PV panel surface becomes an essential issue for the enhancement of solar harvesting.

Cleaning methods for dusty PV panels are many. However, they have some type of energy or resource consumption issues related to them. The traditional mop requires manpower to operate; the pressurized water consumes huge amounts of water; other methods share these characteristics in them. This gave rise to the need for a more efficient cleaning system. Utilizing the self-cleaning method which exists in hydrophobic can be considered a valid solution for this problem. The droplet cleaning method consumes small amounts of water and hydrophobic surfaces to efficiently clean the dusty surface. Enhancing the characteristics of the hydrophobic surfaces can significantly improve the efficiency of solar energy harvesting.

1.4 Objectives

The Thesis examines the effect of surface texturing on the produced surfaces and the various methods incorporated to enhance the important surface characteristics in order to maximize the energy harvesting efficiency. The followings are the objectives:

1. Surface texturing of PC wafers through acetone induced crystallization
2. Examine the surface characteristics of the crystallized PC surface
3. Replication of textured surfaces by PDMS and surface characterization.
4. Impregnation of crystallized PC surface by silicone oil and examining the effect it yields on the optical transmittance of the surface
5. Examine the effect of oil film thickness on the impregnated surface
6. Examine the characteristics of the dust particles in the surrounding environment
7. Assessment of silicone oil and water cloaking of dust particles
8. Analysis of droplet picking up dust particles from silicone oil Impregnated surfaces
9. Theoretical and Numerical analysis of droplet behavior on a silicone oil-impregnated surface.
10. Introduce carbonated water to enhance dust picking mechanism

1.5 Significance

Solar energy is the most abundant free energy in the world. In contrast to fossil fuels, solar energy is infinite, non-polluting source of energy that doesn't emit any greenhouse

gas while producing electrical energy. Solar energy systems are becoming more affordable as the cost of solar cells keeps declining. Implementing a solar system may cost a high initial capital; however, the collective cost through the life cycle of the PV panel is relatively cheaper compared to acquiring electricity from the grid. The relatively short payback period for a solar system ensures that energy can be harvested free of charge for more than half of the PV panel's lifecycle. PV panels generally have lifecycles of 25 years.

The amount of electricity that can be harvested from the PV panels can vary depending on various variables. The solar cells' quality, location of energy harvesting, and panel's tilt angle are a few examples of these variables. The accumulation of dust on PV panels is another major variable that is detrimental to the efficiency of solar energy harvesting. Eliminating such variables can enhance the system's performance.

Utilizing the cost-efficient droplet cleaning method to eliminate the accumulated dust on PV panels can help increase the system's efficiency. However, the process of creating the required surface for this method can bring some downsides to the solar energy harvesting efficiency. This thesis visits the various methods to mitigate these downsides and tries to explore the characteristics and behavior of the water droplet in these methods.

1.6 Scope and Limitations

The thesis concentrates on the hydrophobic surface generated from PC crystallization. The thesis will start by introducing the effect of dust accumulation on PV degradation. It will continue to explain the process of dust formation, surrounding environment, and

characteristics. It will further demonstrate some of the dust cleaning methods and concentrate on the droplet cleaning method utilizing hydrophobic surfaces. The thesis will demonstrate the procedure for creating a crystallized PC hydrophobic surface and replicating its surface texture using PDMS. It will further focus on the effect of impregnating the hydrophobic surface using silicone oil.

PC wafers have the dimensions of 7x3 cm. The solution utilized for the surface crystallization is Acetone. PDMS is utilized through the liquid casting technique to replicate the PC crystallized surface. PDMS is used with a 10 to 1 ratio relative to the catalyst. The heat treatment which follows the casting is divided into two stages. The first stage is for the PDMS to be exposed to room temperature for 24 hrs. Whereas, the second is for the PDMS to be exposed to a temperature of 60 °C for 1 hr. The oil used to impregnate the surface is silicone oil. Utilizing an ellipsometer to measure the oil film thickness was one of the initial objectives of this thesis. However, the inert properties of the PDMS become an obstacle as measuring the oil film thickness becomes extremely difficult.

CHAPTER 2

LITERATURE REVIEW

Solar energy harvesting is one of the leading renewable energy sources. The process of dust particle formation, its induced motion in the atmosphere, and deposition on a PV panel surface are the main causes to minimize the efficiency of solar energy harvesting. This prompted many studies to be performed to understand these processes and their effect on the efficiency of the PV panel. These studies became the cornerstone for further studies to be performed in order to mitigate these issues. Cleaning the surface of the PV panel became a clear requirement and enhancing the cleaning techniques became the research field of many studies. These led to the manufacturing of self-cleaning surfaces which reduced the need for frequent cleaning of the surface and subsequently, improved the efficiency of the PV panel.

2.1 Effect of Dust on PV Panels

This section views the process of dust particle formation, characteristics, driving factors, and dynamic behavior. It further views the effect of dust accumulation on a PV panel surface.

2.1.1 Sand and Dust Storm (SDS) Formation

SDS, according to World Meteorological Organization, is the phenomenon where great amounts of dust elevated by surface winds lead to reduced visibility in the range of eye

level to less than a one km altitude [53]. Storms, typically, have different particle sizes which make it difficult to discriminate between the definition of sand and dust storms. Storms dominated by sand particles, which have a particle size larger than 60 microns, tend to govern low altitude zones within some meters above the ground surface and have a limited aerial range [54].

Particle movements are induced via the creep, saltation, and suspension processes. These processes refer to different types of movements which correspond to a particle size where large particles with diameters greater than 500 microns creep the land, medium particles with diameters between 63 and 500 microns experience saltation where particles jump to a height less than 1.5 m while traveling and small particles with diameters less than 63 microns travel to longer ranges while being suspended [55]. During the process of saltation, the particle, which travels via jumping some distance, bombards the soil. Subsequently, Sandblasting processes are created where the particle bombarding the soil fragments into finer particles with smaller diameters which continue the saltation and sandblasting processes to form finer particles till they reach the size where the suspension process prevails [56]–[58]. Figure 6 illustrates the different processes of particle transportation via wind. The processes are interconnected starting from a creeping particle rolling on the ground and losing some of its sizes due to the friction with the ground. The reduced particle and the released fragments follow the saltation and sandblasting processes and eventually reach the suspension process depending on their respective sizes.

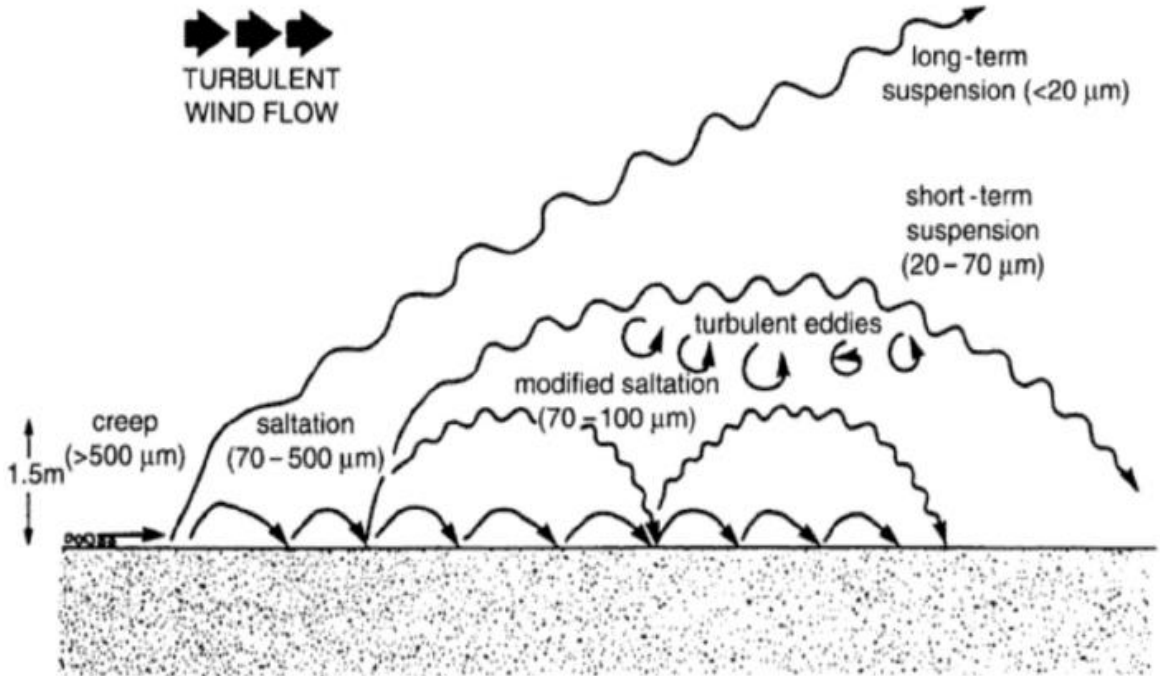


Figure 6 The various processes of particle transportation via wind [55]

Global dust emissions mainly come from natural sources, whereas anthropogenic sources contribute to a minority of about 25% of the dust emissions. Hydrological changes induced by humans constitute the main share of the anthropogenic sources driving SDS. The growing demand for water where natural water sources are absent led to the active participation of humans in the hydrological process to provide water channels from distant natural resources. Consequently, this contributes to the demise of the natural water source and regression of vegetation areas. Vegetation provides protective measures against SDS where the green layer can affect the wind flow and increase the stability of the soil via the recycling of organic substances. The constant abuse of natural resources can lead to degraded land where wind erosion's effect on agricultural productivity is eminent.

Major SDS events worldwide are mainly accounted for by the combination of bad land management and persistent drought [54]. Climate change is another byproduct of human

intervention in the natural process of the world. Industrial waste, chemical emissions, deforestation, and other human activities lead to a world where the global temperature is on the rise, desertification is increasing and wind storms are intensifying. The production of greenhouse gases which is another contributor to climate change is mainly caused by land degradation. The current rise in SDS around the world is mainly prompted by human intervention on the Earth system's balance [54].

A combination of interlinked direct and indirect drivers in the natural ecosystem is the main source for the wide spread of SDS around the world. Many natural factors come to light when considering SDS emissions which include climate, surface roughness, and soil state [58]. Wind erosion, the main driver for SDS emissions, through different processes, can produce and elevate the dust particles to a height where they could be easily transported. However, the wind speed recorded a decline in the area with latitude less than 70° during the recent decades which minimizes the risk of SDS [54]. The surface roughness of vegetation and non-erodible elements such as rocks and pebbles becomes a barrier against wind erosion [58]. Figure 7 depicts the factors and impacts related to SDS emissions.

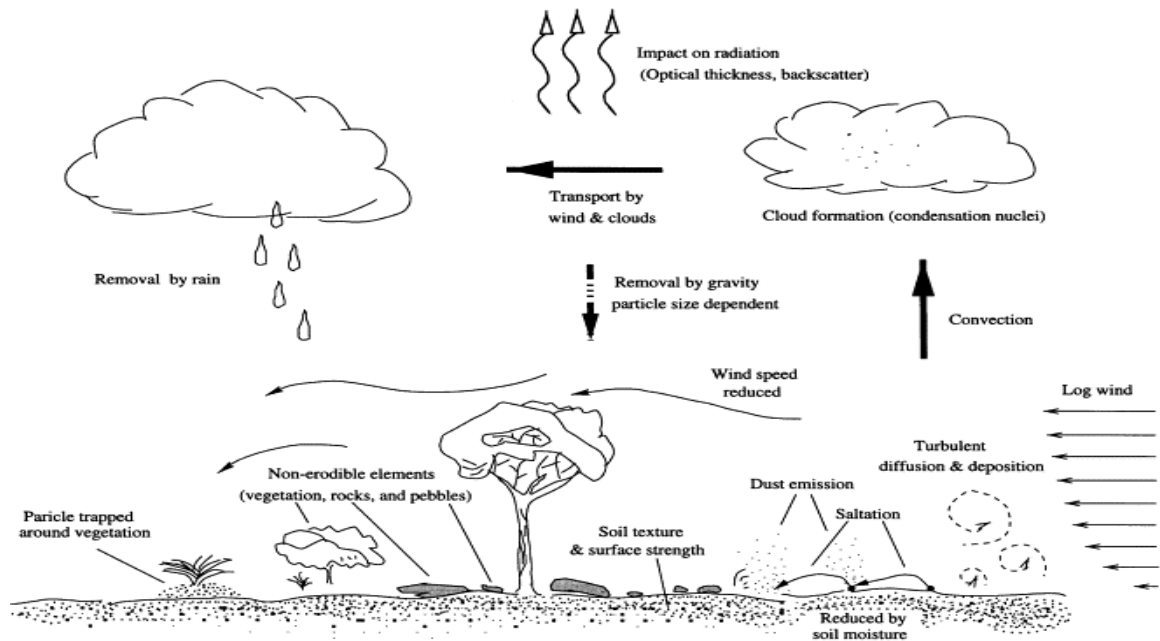


Figure 7 The physical processes which influence dust emission, transport, and deposition [58]

The soil state, which describes its composition, texture, aggregation, and crusting, can determine the degree of freedom for the wind to erode it. Soil is mainly composed of minerals, organic matter, water, and air. The diverse ratios of the composition can determine the properties of the soil which are typically different in various regions [59].

Soil texture is a method to describe the sensation of the soil material which can be fine smooth soil or coarse gritty soil. This term can be further used to classify the soil based on the particle size measured where the major classifications, which are developed by the U.S. Department of Agriculture, are separated into four groups. Gravel, sand, silt, and clay, which respectively refer to soil particle sizes of greater than 2 mm, 0.05 to 2 mm, 0.002 to 0.05 mm, and less than 0.002 mm [60].

Soil aggregation is the process of compounding various soil particles into a secondary unit where soil organic matter plays the main role in binding the mineral particles to form a bigger soil [61]. Different factors cause the formation and stabilization of soil

aggregates which include the quality and quantity of soil organic matter, mineralogy, clay content, and moisture content [62], [63]. The Stability of aggregates, which is a suitable measure of soil structure, refers to the ability to resist outside forces such as wind erosion that attempt to disintegrate them. Aggregate stability has a direct influence on water infiltration, plant emergence, and soil erosion [64]. Aggregate with low structural stability, which can be mainly attributed to organic matter deficiency in the soil, promote the dispersion of soil particles which, subsequently, could travel to the pores of the aggregate and clog them. Consequently, the clogged pores of the soil, which inhibit the infiltration of water to the soil, coupled with an arid or semi-arid climate, which leads to more compact soil, produce soil crust. Soil crust is soil with a high bulk density, thin layer surface, and high penetration resistance [65].

The fraction of surface winds greater than the erosion threshold, which is set by the local properties of the surface, is responsible for the dust source activity [56]. Most natural dust source areas are defined by the combination of high erodibility of the surface material and the arid climate which decreases the protection provided by vegetation cover. Therefore, depressions, inland drainage basins, in arid areas dominate most major dust sources. This is credited to the geomorphic dynamics and surface materials that have wind-erodible nature [66].

Bullard et al. (2011) identified seven basic geomorphic areas which are generally found in arid and semi-arid areas. These areas can be easily recognized from remotely detected information. The susceptibility to wind erosion in these areas differs owing to their diverse surface characteristics. These geomorphic types are lakes, high relief alluvial

deposits, low relief alluvial deposits, stony surfaces, sand deposits, loess, and low emission surfaces.

A great risk of dust emission is present in dry lakes with unconsolidated sediments and ephemeral lakes (lakes that are only filled with water for a period of time depending on external conditions such as rainfall). The dry lakes may experience selective removal of fine particles reducing the erodible materials in the dry lake which, subsequently, lowers the risk of dust emission. The ephemeral water bodies are considered as a significant dust source to the renewal of sediments that they bring to the lake.

Alluvial plains can exhibit dust emission relative to the status of their sediment deposits. These plains are mainly flat plains that are a product of the accumulation of sediments over a long period of time. Substantial dust emissions are present in unarmoured, high relief deposits where periodic rains, which introduce fresh sediment into the deposit, are present. Substantial dust emissions can also be generated in unincised, low relief deposits which permit the replenishment of sediments.

Sand deposits, which are mainly subcategorized into Sand sheets and Aeolian sand dunes, can contribute to the risk of dust emissions. Low relief sandy deposits areas are identified as sand sheets. Sand sheets are susceptible to wind erosion due to the arrangement and size of the sand sediments. Nevertheless, wind erosion is restricted by coarse sands, shallow water, or vegetation which also reduces the risk of dust emissions [66]. Wind-worked deposit with distinct relief is identified as Aeolian sand dunes. The activity level, type, and environmental history are the main factors in producing dust emissions that are generated from the sand dunes. Older sand dunes are bigger and more stable dune

structures where fines may accumulate within the dunes. However, young sand dunes are smaller and active dunes where little fine material is contained within the dunes. The young dunes with little fines are not major dust sources [66]. However, the risk of dust emission will increase in arrears which exhibit a disturbance of older dunes. The presence of mobile dunes near infrastructures whether it was caused by SDS or sand movement goes against human interest. Dune destabilization is mainly caused by the vegetation cover reduction which is largely credited to drought, burning, unsustainable harvesting, grazing, and cultivation [67].

Loess is a depositional landform where silt-sized sediments are the main component and mainly have Aeolia origin [68]. They can significantly contribute to dust emissions with the aid of disturbance or reduced vegetation [66].

Historic data suggest a doubling of global dust loads over the 20th century which is primarily attributed to vegetation cover and/or climate change around the globe [68]. Stanelle et al. (2014) studied how the changes in vegetation cover and climate can be related to dust emissions over the period from the late 19th century and today.

They utilized a climate-aerosol model (ECHAM6- HAM2) combined with a new scheme specifically designed to use vegetation cover in order to derive potential dust sources. The design had the ability to differentiate between emissions from agricultural and natural dust sources [69]. The simulations suggest that the global annual dust emissions have increased by 25% over that time period. Climate change was accountable for approximately 56% of this change, whereas vegetation land cover change was accountable for approximately 40%. However, large regional differences for this change

were present. The present dust emissions were visibly dominated by agriculture in North America whereas climate change was the dominant factor in North Africa⁰⁰. These results demonstrate that human intervention has a high impact on dust emissions. Subsequently, this will lead to large implications for biogeochemistry and climate in the future [68].

2.1.2 Characteristics of Accumulated Dust on a PV panel

The characteristics of accumulated dust and its effect on the degradation of the PV panel are a function of the dust loading on the PV panel. The Dust accumulation rate (DAR) on the surface of a PV panel is mainly influenced by the weather conditions, distribution of aerodynamic particle size, and airborne particle concentration. These factors are all variables that depend on the PV panel's surrounding environment [70]. The exposure time can also be considered as the main factor on the PV panel's DAR [71].

Several studies were performed to correlate the DAR on a PV panel. A study performed in Athens, the Greek capital, recorded dust deposition masses of 100- 1000 mg/m² for a 2- 8 weeks exposure period [72]. Another study performed in Dhahran, Saudi Arabia, recorded dust deposition masses of 6184 mg/m² for an outdoor exposure period that extended from February to December [73].

Additional studies were performed in various locations. Mesa, Arizona (USA), recorded a DAR of 132 mg/(m² day) [74]. Colorado, USA, recorded a DAR of 1- 50 mg/(m² day) [23]. Whereas Minia region, Egypt recorded a DAR of 150 - 300 mg/(m² day) [24]. These results were observed depending on the location and tilt angle of the PV panel. Furthermore, in Colorado, USA, dust accumulation rates of 5-20 and 10- 80 mg/(m² day)

on 40° inclined glass surfaces have been recorded at the Erie site and Commerce City, respectively [77].

The characteristics of accumulated dust have a major effect on PV degradation. Studies conducted in a laboratory environment have proven that the dust physicochemical properties have a major impact on PV energy harvest which is related to PV dust soiling [78]–[85]. Studies performed in the laboratory using artificial dust have recognized 15 forms of dust pollutants. Six pollutants among the 15 types appear to have a bigger influence on PV performance degradation than their contemporaries at a specific surface loading. These six pollutants include ash, red soil, limestone, silica, calcium carbonate, and sand [86].

The advancement of soiling mitigation technologies requires studying and defining the physicochemical characteristics of accumulated dust. The chemical composition of the accumulated dust along with particle size distribution can help in determining the interaction process between the PV surface and the dust particles which, subsequently, reflects on the usefulness and efficiency of the PV soiling mitigation technologies [87]–[90]. Whereas many theories suggest the possibility to mitigate PV soiling by converting the surface of the PV module into hydrophobic or hydrophilic, the particle properties have a clear effect on the affinity of particles to PV surfaces.

The importance of determining the deposited dust characteristics can thus be shown from the previous aspects [91]. PV soiling mitigation can also be accomplished utilizing active methods which include the dust particles removal of from the PV surface using mechanical or electrostatic devices. Defining the properties of the dust particles can be

used to assess the adhesion force of the particles on the PV surface, along with the dust particle motion pattern in an electric field [90], [92].

Dust particle size distribution which is deposited on the PV surface is another major factor in soiling-related PV degradation is also dependent on dust [18], [93], [94]. The dust particle size has a significant effect on the absorption, scattering, and reflectance of incident light on solar cells which, subsequently, affects the performance degradation of the PV panel. The larger dust particles show a greater tendency of resuspension than smaller dust particles even at moderate wind speed which in turn promotes the accumulation of smaller size dust particles on the PV surface [95]. Therefore, performance degradation of PV panels due to soiling is more significant in finer dust particles than larger dust particles which are accumulated for the same dust load. The greater specific surface area, exhibited in the finer dust particles, allows the particles to be more uniformly distributed compared to the coarser dust particles. The uniform distribution, subsequently, reduces the gaps between the dust particles where the light can reach the PV surface which minimizes the amount of light reaching the PV cell [96]. Weber et al. (2014) stated that a 1-50 μm range of particle size is expected for the accumulated dust deposited on the PV surface. However, accumulated dust on PV panels in desert environments has limited research on particle size distribution[95].

The characterization of naturally accumulated dust and its influence on PV degradation can be difficult to specify. This is driven by the complex phenomenon of dust accumulation which varies with the varying locations of the PV panel where the environmental and weather conditions are diverse [89], [97]. Therefore, understanding the naturally accruing dust accumulation can be only achieved via extensive studies in

different locations with varying environmental conditions and exposure time. Several studies have been carried out in diverse conditions which include the exposure period, disposition surface, tilt angle, and location of the study. The resulting DAR on the deposited surface of these studies are shown in table-1 [19], [20], [22]–[25], [43], [98]–[100].

Table 1 The dust accumulation rate (DAR) on the deposited surface for various environmental conditions [19], [20], [22]–[25], [43], [98]–[100]

Location	Sampling period	Deposition surface	Exposure period	Tilt angle, orientation	DAR (mg m ⁻² d ⁻¹)
Doha, Qatar	Jan-Oct 2015	PV modules (1.2 × 0.6 m ²)	Daily	22°, South	215–306
			Biweekly		155
			Monthly		140
			Bimonthly		120
			Six-month		80
Bankok, Thailand	Apr-May 1998	Plastic sheets (30 × 30 cm ²)	6 days- one month	15°, South	125–440
Minia region, Egypt	1999	Glass plates (7 × 7 cm ²)	Weekly	0°, Horizontal	230–330
				20°, South	150–200
Rumah, Saudi Arabia	Jan-Dec 2015	Glass plates (5 × 5 cm ²)	Weekly for 12 months	0°, Horizontal	25–190
Baghdad, Iraq	Sept 2014	PV module	Daily	30°, South-west	210
			Weekly		57
Athens, Greece	Aug-Sept 2009	PV modules (988 × 448 mm ²)	2–8 weeks	30°, South	15–20
Mexico City	Dec 2012-May 2013	Glass plates (60 cm ²)	Weekly	0°, Horizontal	65 (24–102)
Colorado, US	Aug 2011-Jun 2014	Glass plates (10 × 10 cm ²)	1–5 weeks	0°, Horizontal	20–50
				40°, South	12–35
Mesa, AZ, US	20–22 Oct 2014	PV module	2 days	33°, South-west	132
Commerce City, US	Aug 2011-Jun 2014	Glass plates (10 × 10 cm ²)	1–5 weeks (mostly 2 weeks)	0°, Horizontal	10–120
				40°, South	10–80
Erie, CO, US	Nov 2012-May 2014			0°, Horizontal	5–60
				40°, South	5–20

Wasim et al., conducted an extensive study where the quantity and physicochemical characteristics of dust particles of varying exposure periods for a specific tilt angle of a PV surface were targeted. Their study which was conducted in Doha, Qatar showed a decreasing trend of DAR and increasing dust load for increasing exposure periods which is displayed in Figure 8.a and Figure 8.b. Figure 8.c Shows the DAR and corresponding

environmental variation for daily measurements during the winter and summer sampling period [99].

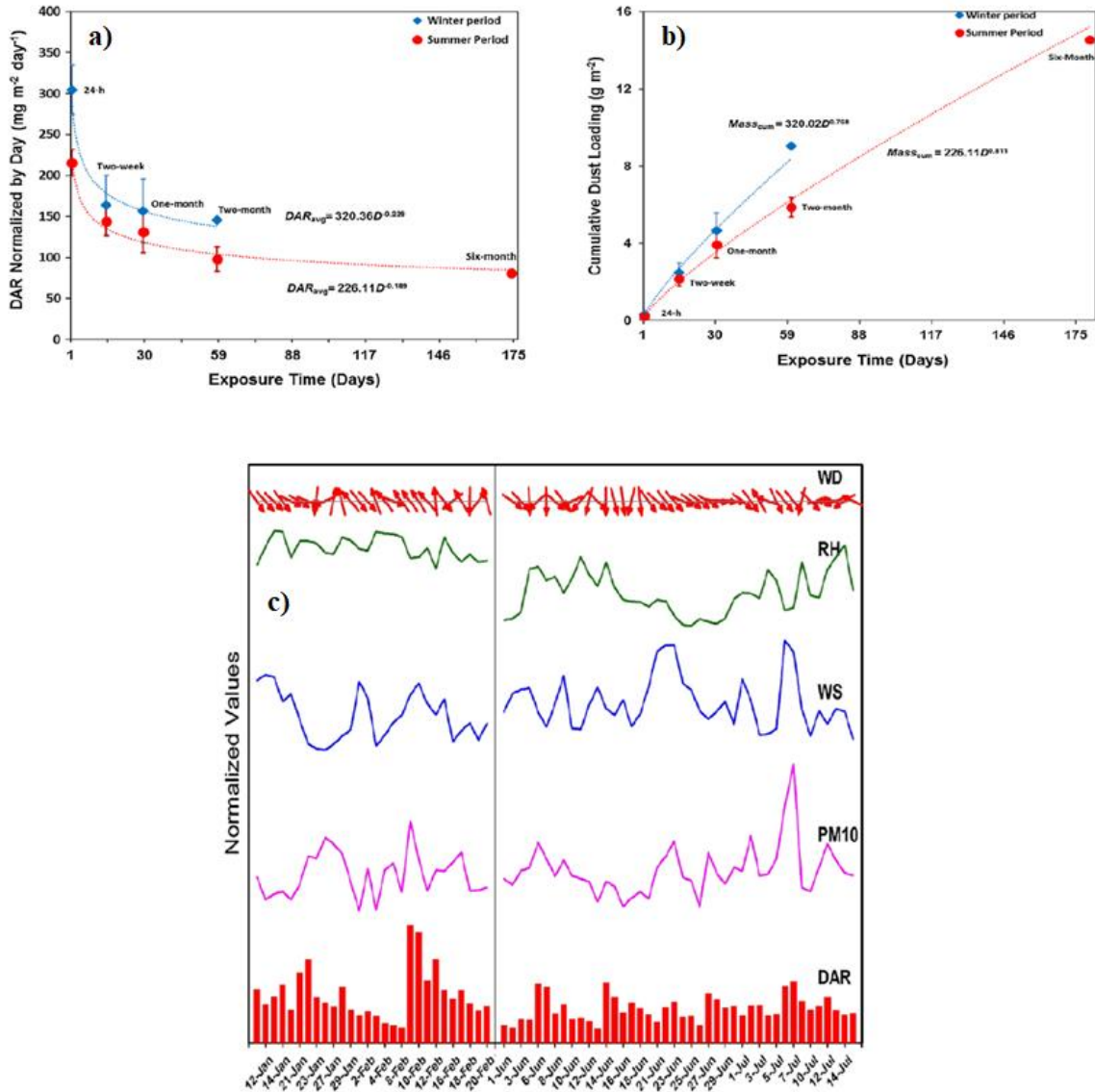


Figure 8 The characteristics of dust accumulation rate (DAR) for a specific exposure period: a) decreasing trend of DAR for increasing exposure periods, b) increasing dust load for increasing exposure periods, c) the DAR and corresponding environmental variation for daily measurements during the winter and summer [98]

XRD analysis of accumulated dust samples where the chemical composition of the accumulated dust is determined and shown in Figure 9. The analysis shows a nearly stagnant value for the major mineral composition. The major minerals of the chemical

composition for all collected dust samples are dolomite ($\text{CaMg} [\text{CO}_3]_2$), calcite (CaCO_3), and quartz (SiO_2). More than 70% of the dust particle contents were dominated by both dolomite and calcite compounds of the accumulated dust samples. The less dominant minerals are quartz and gypsum with the remainder of other primary silicate minerals (i.e., cristobalite, albite, palygorskite, and kaolinite). The chemical composition, however, varies substantially for various locations and climate zones in the region. The dominant minerals observed in their study are credited to construction projects in the local environment where these minerals are associated with cement, limestone, concrete, marble, and Portland [98].

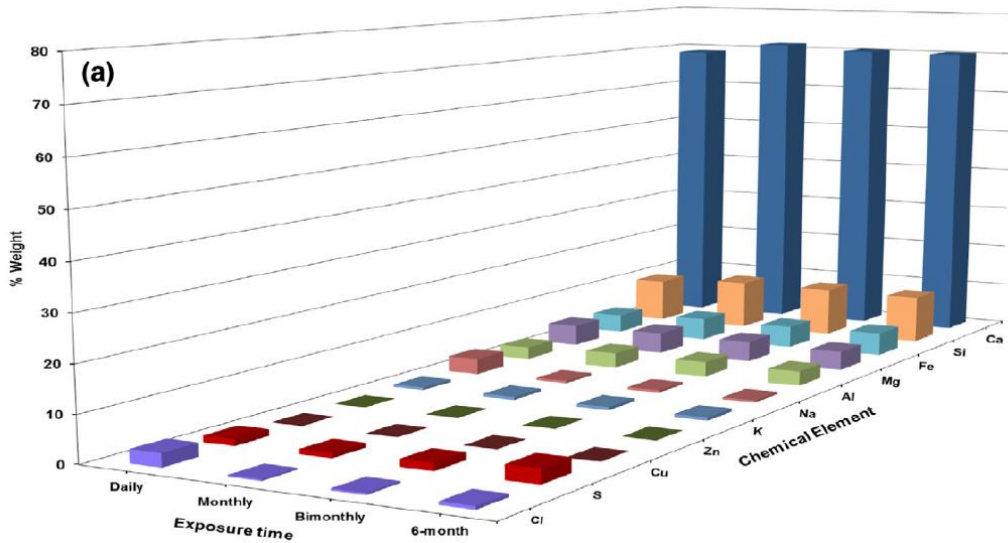


Figure 9 The chemical composition of the accumulated dust in Doha [98]

2.2 PV Degradation

Solar Panels are devices that have the ability to harvest one of the most abundant renewable energies on the planet, solar energy. They utilize the ability of photovoltaic (PV) cells which comprise the most fundamental structure of a solar panel, to convert optical electromagnetic radiation energy to electrical energy. This process utilizes the effect of the semiconductor materials, typically silicon, in the PV cell [101]. The inherent properties of the semiconductor material limit the PV system's efficiency to a range of 15- 20 % of the provided energy [97]. Varying performance levels can be exhibited by the PV panel due to various factors such as environmental conditions, system design, installation panel orientation, and others. Among the environmental factors to be considered, dust is a major factor that should be considered for the optimization of the PV panel's efficiency. Kaldellis and Kokala [72] observed that the intensity of the solar radiation on the PV panel surface is the key factor that contributes to a PV panel's electrical output. However, dust can limit the intensity of the energy harvested by the panel which can further degrade its efficiency by up to 15%. The effects of dust causing the degraded PV panel's efficiency can be subcategorized into the effects of deposited dust on the PV panel's surface and the scattering dust in surrounding atmosphere.

Solar radiation experiences a quantity reduction phase in its journey throughout the atmosphere before reaching the PV panel. The solar radiation's reduction is attributed to the properties exhibited by light waves while traveling through a medium which includes absorption, transmission, scattering, reflection, and refraction. The atmosphere, which acts as a medium between the energy source and the PV panel, contains many obstacles

which inhibit the amount of energy delivered to the PV panel such as particles, air molecules, water vapor, dust, and other variables where the light wave properties take effect [102]. Therefore, the dust scattered in the atmosphere can negatively influence the direct component of solar radiation [103] which, subsequently, increases the diffuse irradiance component [103], [105]. It can be further inferred that the amount and nature of the pollutant can impact the reduction in solar radiation energy [5]. Consequently, the rural areas where pollution is a less prominent factor collect more global radiation compared to the urban areas [105]–[108]. Climate changes such as wind and rainfall can minimize the suspended particles' concentration in the atmosphere which can increase the available solar radiation for PV panel harvesting [109], [110].

The incident irradiance on PV modules affects the electrical behavior and output delivered by the panel [106]. The electrical characteristics of a PV cell can be recognized by the Power vs. voltage (P-V) and current vs. voltage (I-V) curves under varying levels of radiation. The amount of solar insolation on the surface of the PV panel, which is the solar power received by a unit area of a PV cell, is directly proportional to the output power. Therefore, increased solar insolation leads to an improved efficiency [111], [112]. Subsequently, a decreased amount of solar insolation due to the previously mentioned factors can lead to a degraded efficiency of a PV cell. Jiang, Lu investigated the relationship between the output efficiency and solar insolation in PV cells and observed a reduction in output efficiency ranging from 4.4% to 11.6% for solar radiation which ranged from 300 to 760 W/m² [79].

This phenomenon that scattered dust can reduce solar insolation is further proved via the collected data of previous studies conducted on various environments. The solar insolation in the city of Amman, Jordan diminished by approximately 5 MJ/m^2 in the period between 1983 and 1988 which was attributed to the weather condition of sand storms experienced in that area [102]. Similarly, cities such as Hong Kong and Central Mexico City which exhibits significant photochemical smog or industrial aerosol exhibit large solar insolation reduction compared to other cities around the globe [113].

Deposited dust on a PV panel surface can further scatter, reflect or absorb some of the incoming solar radiation [114]. Experiencing these negative light wave properties can affect the amount of light transmitted to the collection surface. The ratio of light intensity that passes through a specific material compared to passing without the presence of such material is defined as light transmittance [115], [116]. Subsequently, the cover glass of the PV panel which contributes to the light transmittance can also be a factor in the solar PV system's efficiency.

Dust accumulation on a PV panel surface has a clear contribution to the reduction of surface transmittance of the PV panel. The increasing dust deposition on a glass surface results in an exponential reduction of surface transmittance until the transmittance reaches its lower limit where the effect of increasing the amount of dust deposition on surface transmittance vanishes [76], [117]–[120]. Studies conducted on the effect of deposited dust on surface transmittance showed that an approximate deposited dust density of 0.5 mg/cm^2 and 1.6 mg/cm^2 results in a surface transmittance reduction of approximately 11- 24% and 38- 53% respectively [19], [24], [117].

Dirt correction factor (DC) can be utilized to estimate the solar radiation absorbed by the collector. DC is defined as the contaminated to clean surface transmittance ratio which is applied to the total incident radiation. The value of the dirt correction factor was recorded for various conditions such as location, design, installation, and exposure period and was observed to lie in the range between 0.7 and 0.925 [71], [76].

The tilt angle of the surface can contribute to the surface transmittance reduction of the PV surface. The increasing tilt angle will help remove the deposited dust from the surface due to the effect of gravitational force which will, subsequently, decrease the transmittance reduction [76], [117]. It was observed that the minimum surface transmittance reduction for a 90° surface tilt angle was recorded as 4.94%. Whereas the maximum surface transmittance reduction for a 0° surface tilt angle was recorded as 27.62%. Sample surfaces that were not cleaned during the study experienced a greater reduction in surface transmittance where the surface experiences approximately double the reduction and an increase of 0.736 mg/cm² dust deposition density for a horizontal tilt angle compared to a surface that was cleaned during the study [117]. Hegazy [76] demonstrated that samples installed at smaller tilt angles (< 40°) experience a significant transmittance degradation, whereas a further increase of the tilt angle of the sample will result in a rapid decrease of surface transmittance. A study conducted outdoors showed a variation of transmittance reduction between the top and bottom of a tilted glass sample where the lower part experiences greater reduction. This could be attributed to the incomplete cleaning of the sample following a rainfall where the deposited dust was only cleaned from the top and was settled at the bottom level of the sample [121].

Rainfall can bring both negative and positive effects on the PV panel surface. The negative effect comes as a result of the wet deposition process where the property of the rain to entrap the air pollutants and deposit them on the PV panel surface is utilized [97]. Nonetheless, the polluted modules can be cleaned by rainfall. Zorrilla et al. [122] showed that the daily reduction of irradiance caused by dust deposition can exceed 20% during long dry periods. Cuddihy et al. [123] observed that soiling accumulation on a PV panel surface can be comprised of three different layers. The top surface layer which is built up loosely can be removed by rain without additional interference. Therefore, this type of deposition layer realizes its maximum accumulation during dry weather, and following a rainfall, it will experience a minimum accumulation. The rain-resistant layer which is formed in about 1-2 months of dry periods can be further categorized into two layers where the secondary surface layer can be removed by washing whereas the primary surface layer requires abrasive scrubbing to clean the accumulated dust deposits from the surface. Figure 10 illustrates these surface layers of soil [124].

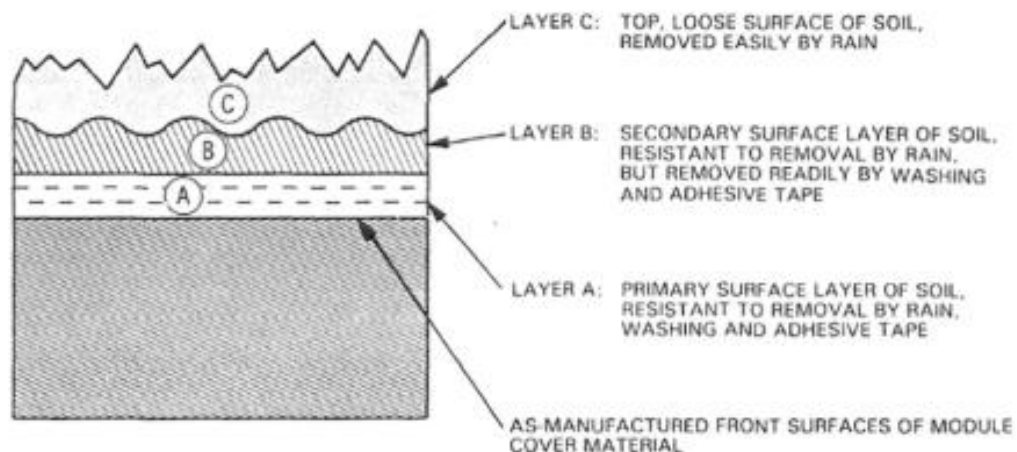


Figure 10 Surface layers of the soil of accumulated dust on the deposited surface [124]

The overall contribution of the rainfall to the surface transmittance and its effect on accumulated dust is determined by its pattern. Evidently, a low quantity of rainfall leads to minimum utilization of the natural cleaning procedure of a PV panel surface. Furthermore, such a pattern typically increases the dust adhesion on the PV panel surface. Panel surfaces that experienced heavy dust accumulation prior to the rainfall faced with a low rainfall pattern will experience the transformation of dust into mud which will further attract dust and subsequently require a more extensive cleaning procedure [125]. Whereas, frequent and intense rainfall can entrap more pollutants from the panel surface leading to maximum utilization of the natural cleaning procedure of a PV panel surface.

The properties of dust particles can affect the surface transmittance reduction of the PV panel surface. Finer dust particles can be aligned in a more uniform manner compared to coarser dust particles. The uniform distribution of the finer dust particles can further minimize the open area where the incident solar radiation can penetrate to the collector surface. Theoretical manifestation of this phenomenon was obtained by Mazumder et al. [120] where they utilized Eq. 2.1 and Eq. 2.2 to deduce the surface transmittance of increasing dust deposition for three different dust diameters. The equations employ particle concentration (N_0), particle diameter (d), and extinction efficiency (Q_{ext}) to measure the surface transmittance. Whereas experimental validation for this theory was obtained by El-Shobokshy et al. [93]. Figure 11 respectively demonstrates these validations.

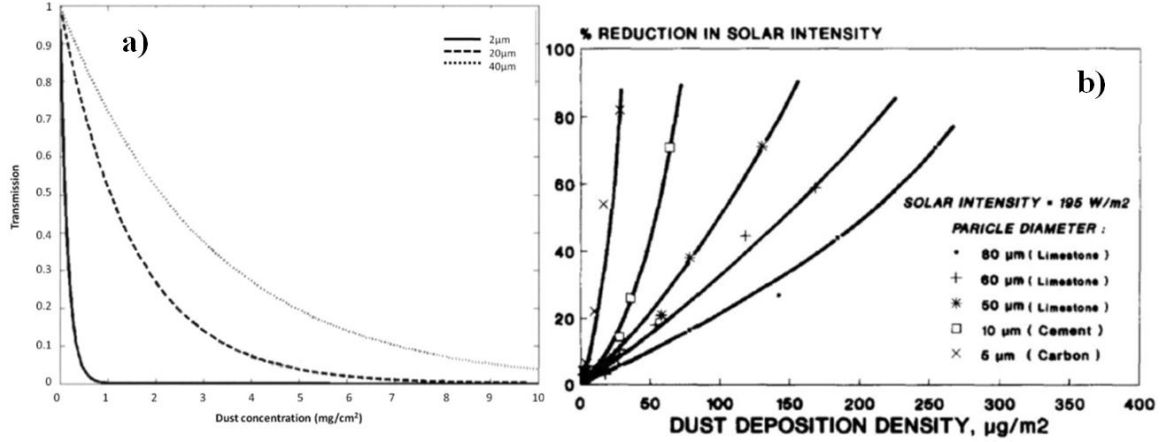


Figure 11 The uniform distribution of the various sizes of dust particles and its effect on a) optical transmittance and b) solar intensity [93]

$$\tau = \frac{I}{I_0} = \exp(-NA_p Q_{ext}) \quad (2.1)$$

$$NA_p Q_{ext} = \sum_i \pi(N_0)_i \left(\frac{d_i}{2}\right)^2 (Q_{ext})_i \quad (2.2)$$

Ramli et al. performed an extensive study to determine the effect of dust layers covering a PV panel surface on the power loss experienced by the PV Panel. They first performed measurements of the electrical output of a clean PV panel to serve as a reference and performed an analytical model for their study where they confirmed similar results for both procedures. The PV module is then exposed to outdoor environmental conditions and measurements were collected for various time periods.

The dust accumulated for a time period of one week resulted in a slight decrease of power output by approximately 2.05% compared to the reference surface and approximately 1.04% compared to the analytical model. The power loss of the PV panel becomes more evident as the dust accumulates on the surface of the PV panel for two weeks when the dust layer becomes clearly visible. The dust accumulated for a time period of two weeks

resulted in a decrease of power output by approximately 10.8% compared to the reference surface and approximately 9.25% compared to the analytical model. This power loss combined with an average ambient temperature of 36.89 ° C and average relative humidity of 52.24%, qualifies the PV surface to be termed as a surface with the dusty condition.

The following two weeks of dust accumulations encountered a brief period of drizzle. Combined with the previous dusty condition of the surface the PV panel experienced further dust accumulations and an extreme loss of power output. The dust accumulated for a time period of four weeks resulted in a significant decrease of power output by approximately 87.29% compared to the reference surface and approximately 87.29% compared to the analytical model. This power loss combined with an average ambient temperature of 36.11 ° C and average relative humidity of 44.77%, qualifies the PV surface to be termed as a surface with the dusty condition.

They, further, tested the power loss experienced during rainfall and cloudy conditions. The high humidity caused by the rainfall contributes to a significant power loss of the PV panel. The rainfall environmental condition resulted in a significant decrease of power output by approximately 43.03% compared to the reference surface and approximately 41.85% compared to the analytical model. This power loss combined with an average ambient temperature of 28.97 ° C and average relative humidity of 76.32%, demonstrates the effect of the presence of water vapor in the air on the power loss experienced by a PV panel. The cloudy environmental condition, also, resulted in a significant decrease of power output by approximately 53.69% compared to the reference surface and

approximately 48.75% compared to the analytical model. This power loss combined with an average ambient temperature of 34.06 ° C and average relative humidity of 60.45%, demonstrates the effect of the interference of the clouds in the PV panel’s harvesting of solar power [126].

2.3 Dust Cleaning Methods

The significant power loss experienced by the PV panel in the MENA region is mainly caused by the accumulation of dust particles on PV surfaces. The effect of Dust accumulations on PV surfaces prompted further research and studies in the field of enhancing the dust cleaning techniques in order to recover the original performance of the PV panel and enhance its efficiency. Various cleaning methods can be utilized to perform this task. Figure 12 demonstrates some dust removal techniques which are utilized to clean the PV panel surface.



Figure 12 Dust removal techniques from the solar application [127].

However, the various cleaning methods can be utilized more effectively in various conditions. Some of these cleaning methods can further enhance other climate factors and improve the surrounding conditions of the PV panel. The dust cleaning of the PV panel for shaded and cloudy weather is most suitably performed using aerodynamic streamlining and robotic cleaning methods. The dust cleaning of the PV panel for hot, sunny, and arid weather is most suitably performed using a sprinkler, robotic cleaning, and electrostatic cleaning methods. These cleaning methods are, also suitable for cold and moist weather as well as dry weather. The dust cleaning of the PV panel for snowy weather is most suitably performed using Anti-reflective coating and inverting cleaning methods. The dust cleaning of the PV panel for rainy and humid weather is most suitably performed using anti-reflective coating methods. The dust cleaning of the PV panel for desert areas is most suitably performed using aerodynamic streamlining and vibrating cleaning methods [128].

The natural methods of dust cleaning of the PV module surface are rainfall, wind, and gravity. The most effective cleaning agent for dust is water which is evident in the reduction of dust effect on PV panel following high rates of rainfall. Regions with wet climates, such as Singapore, have the minimal effect of dust accumulation [121]. Rainfall occurs occasionally and in specific regions which is the reason it can't be depended on to mitigate the issue, especially in dry regions.

Wind can also act as a cleaning agent as it has the ability to pull dust particles off the PV surface and partially improve its performance. Mekhilef et al. [129] contributed to the decrease in the relative humidity of the surroundings and higher heat dissipation from the PV panel surface to the increased wind velocity. The wind is also a cleaning method that

can't be completely depended upon as it mainly occurs in windy regions and can sometimes carry dust particles and increase the issue of dust accumulations instead. The wind direction and speed have an obvious effect on the performance of the PV module [121], [130], [131].

Gravity can be utilized as a cleaning method via altering the inclination angle of the PV panel. However, controlling the tilt angle needs to be strictly maintained at specific angles for various regions in order to obtain maximum solar harvesting efficiency from the PV panel. Therefore, the search for an optimal inclination angle for each specific location needs to be determined in order to incorporate the gravitational effect in cleaning the surface of the PV panel [121].

Mechanical methods utilized for dust removal from the surface of the PV panel include the use of removable covers, blowing, and mechanical wiping. Electromechanical methods incorporate vibrating or shaking of the PV module array, as well as, utilizing ultrasonic or subsonic waves to damage the dust adhesion.

The electrostatic cleaning methods which are used to reduce the effect of dust on PV panels were first proposed by NASA. The surface of the PV panel is attached with an electrodynamic screen which was manufactured from UV- radiation resistant transparent plastic sheets, such as polyethylene terephthalate (PET). Conducting electrodes, which are manufactured from transparent indium tin oxide sheets, were connected to the surface of the PV panel in parallel or spiral configuration. AC voltage source is used to connect the electrodes and yield an electromagnetic field which causes the dust particles to repel from the surface of the PV panel. Figure 13 displays the electric curtain method suggested by NASA. Gaofa et al. [132] Mazumder et al. [133] concluded that the

efficiency of dust removal using a PET surface with an electrostatics screen was 80% which gave a boost to the solar cell performance of close to 90%.

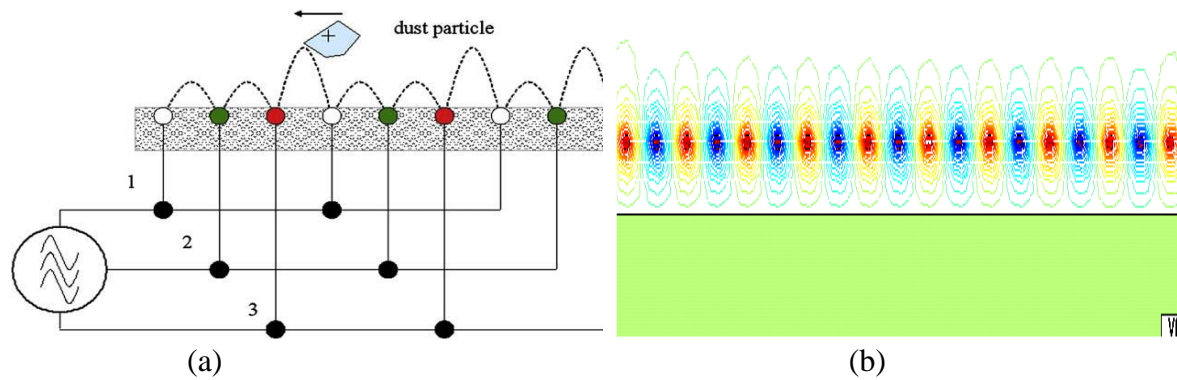


Figure 13 Electric curtain: a) Three-phase electric curtain and b) The electrical field distribution between the electrodes of the shield [132]

2.4 Dust Removal by Self-Cleaning Methods

Modifying surface texture on a micro and nano-scale to fabricate surface is researched in order to develop self-cleaning surfaces which can also optimize the optical properties of the surface. Creating a super-hydrophobic/hydrophilic surface utilizing this method can show its effect on wettability and water droplet mobility. This type of surface can improve the efficiency of the cleaning and, consequently, decrease the rate of performing necessary cleaning. Super-hydrophobic surfaces contain micro- or nano-structure surfaces which are coated with a thin film of low surface energy substance or vice versa [134]. Many efforts are recently contributed to mitigating the dust removal issue utilizing this method.

2.4.1 Hydrophobic Surfaces

A considerable amount of research was launched to examine the characteristics of hydrophobic PC surfaces. Jang et al. were able to modify PC utilizing hydrophilic/hydrophobic coatings in order to fabricate microdevices on the PC surface. They were able to utilize hydrophilic treatment of PC in order to create micro-channels that have the ability to resist organic solvents [135]. Soliveri et al. investigated the self-cleaning polymeric materials which integrate both the hydrophobic and photoactive approaches. They were able to demonstrate the possibility of generating multilayer polymeric/TiO₂ composites which have both photo-oxidation and anti-sticking properties [136]. One method to improve the hydrophobicity of a surface is via the utilization of an ultraviolet laser in order to modify the surface texture of PC surfaces which was accomplished by Jiang et al. They utilized the laser to surface texture of the PC into periodical V shape groves [137]. Zhou et al. examined the characteristics of the PC hydrophobic surface which underwent the process of crystallization. They discovered that the utilization of a solvent-induced method to crystallize the material surface enhanced the surface hydrophobicity of PC [138]. Bhagat and Gupta claim that the superhydrophobic property, which was generated after the micro texturing of PC surfaces, can only be accredited to the physical modification of the surface [139]. Alteration of PC surface by hierarchical micro/nano-structuring was inspected by Saarikoski et al. The results showed a considerable increase of the water contact on the hierarchical micro/nano-structure. Furthermore, the surface reflection decreased with nano-patterning and the transmittance of the PC increased [140]. Yu et al. inspected the micro-phase separation in the polyacrylate-polydimethylsiloxane copolymers for anti-

icing. This separation was associated with the accumulation of PDMS chains upon the polymer surfaces. Therefore, the hydrogen bond interaction between the surface and water could be weakened. Subsequently, the hydrophobic surface will exhibit lower contact angle hysteresis [141].

Soz et al. studied the superhydrophobic polymer surface which was constructed using hydrophobic fumed silica to implement spin coating on the surface. They found that the average roughness of the hydrophobic surface and the surface structure was influenced by both the polymer substance's nature and chemical structure [142]. Huang et al. showed that the presence of nanopillars increases the CA in a hydrophobic surface which was processed using the nanoporous alumina template [143]. Liu et al. demonstrated the ability of a thermally stable PDMS superhydrophobic surface to recover its hydrophobicity post-oil-contamination which is accredited to their high thermal stability expiated below 500 °C [144].

2.4.2 Analysis of Dust Adhesion on Hydrophilic and Hydrophobic Surfaces:

Various parameters can significantly affect the interactions between the particle and the surface. They comprise particle size, particle shape, surface roughness, and adhesion bond which exists between the particle and the surface [145]. Furthermore, the cleaning behavior of the water droplet on a hydrophobic surface and a hydrophilic surface differ greatly. Such behaviors are demonstrated in Figure 14.

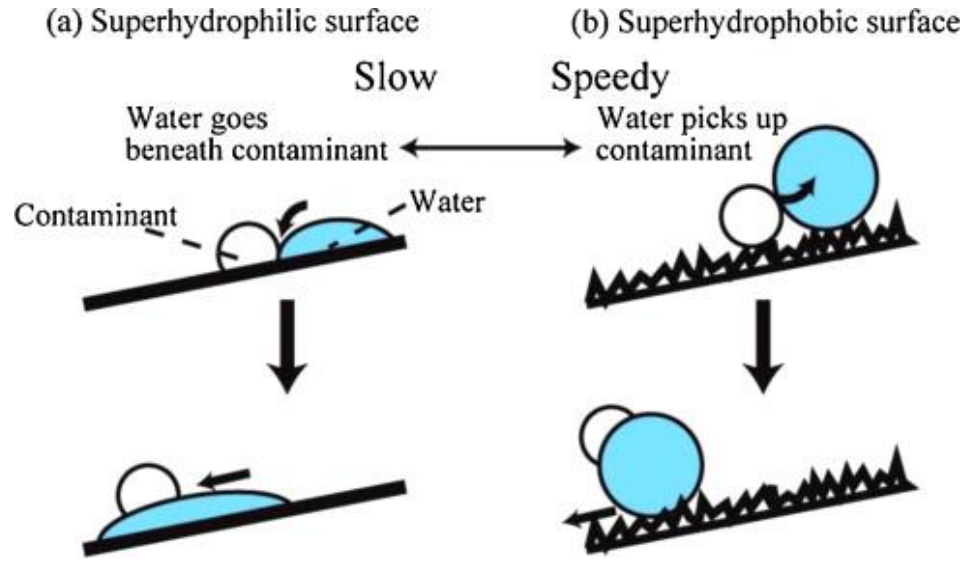


Figure 14 Cleaning behavior by a water droplet on the hydrophobic and hydrophilic surface [128].

Adhesion forces, which exist between small particles and surfaces, are typically resulted from the attractive forces of van der Waals forces, electrostatic forces, and capillary forces. The Van der Waals forces are essentially generated from the intermolecular attraction between the surfaces and the dust particles molecules. This is an attractive type of force that acts to inhibit the resuspension of small particles. The generation of capillary forces is attributed to the formation of a water meniscus around the particles in a humid environment. This capillary force is much higher than van der Waals forces. The electrostatic forces are always present between particles where electrical charging can occur when the coulomb charge of two particles is different and the distance between them is shortened [145]. Therefore, the adhesion force is the summation of these three forces.

$$F_{ad} = F_{vdw} + F_c + F_{es} \quad (2.3)$$

where is F_{ad} the total adhesion force, F_{vdw} is the van der Waals force, F_c is the capillary force and F_{es} is the electrostatic force. The electrostatic force is 10 times smaller than the

van der Waals forces which can further increase in magnitude by 5 times under compression force where the contact between the particles and the surface is increased. The electrostatic forces have minimal contributions to the adhesion forces when external forces are provided.

Hertz studied the interaction of the particle and the surface concerning two elastic spheres [143]. Upon applying a normal force on an elastic sphere, the contact area between the sphere and the surface becomes circular which is demonstrated in Figure 15. Hertz model defined the radius of the contact circle area a_H as:

$$a_H = \left(\frac{Pd_p}{2K} \right)^{1/3} \quad (2.4)$$

where d_p is the spherical particle diameter and K is young's modulus that given as:

$$K = \frac{4}{3} \left(\frac{1-\nu_1^2}{E_1} + \frac{1-\nu_2^2}{E_2} \right)^{-1} \quad (2.5)$$

where ν and E are the Poisson's ratio and Young's modulus, respectively.

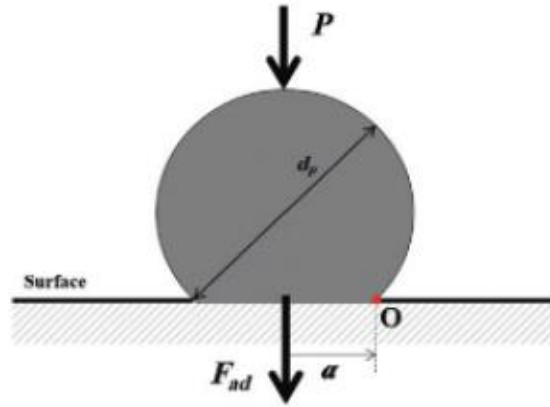


Figure 15 Attachment of plastic sphere particle with the solid surface [144]

The decline in the surface energy creates an attractive molecular force that occurs between the two contacting surfaces. Contacting the elastic sphere results in a balance of energy between the released surface energy and the stored elastic energy. The free energy

loss can, therefore, be represented as E_s and the force F_s can utilize the following expressions:

$$E_s = -\pi a^2 \Delta\gamma \quad (2.6)$$

$$F_s = \frac{dE_s}{d\delta} \quad (2.7)$$

Combining these equations with Hertz analysis gives:

$$F_s = \pi R \Delta\gamma \quad (2.8)$$

$$a = \left(\frac{3 F_s R}{4 E^*} \right)^{\frac{1}{3}} \quad (2.9)$$

where R is the radius of the sphere and $1/E^* = \left(\frac{1}{E_1} + \frac{1}{E_2} \right)$

This model can be valid as long as the Hertz assumption is valid. Further modifications were later introduced to the Hertz analysis to the effect of high elastic modulus spheres and adhesion.

2.4.3 Free Surface Energy and Adhesion

Free surface energy is the energy commonly related to the bond between atoms and the surface. Forming a bond between two materials of varying surface energies per unit area γ_1 and γ_2 creates an interfacial energy per unit area γ_{12} in the interface between them. The required energy to detach the two surfaces per unit area from each other is the work of adhesion which can be represented in Dupré equation [146]:

$$W_{ad} = \Delta\gamma = \gamma_1 + \gamma_2 - \gamma_{12} \quad (2.10)$$

$$\gamma_{12} = |\gamma_2 - \gamma_1| \quad (2.11)$$

where $\Delta\gamma$ represents the decrease in the free surface energy of the scheme per unit area (negative value in mJ/m^2) which indicates that the interfacial energy per unit area γ_{12} has greater magnitude compared to the materials' surface energies per unit area γ_1 and γ_2 . $\Delta\gamma$

can represent the cohesive work which is equal to 2γ for two identical materials in contact. This theory suggests that higher surface energies of surfaces equate to stronger bonds between them. Therefore, the theory of adhesion proposes materials with low $\Delta\gamma$ and low surface energy (γ). Figure 16 demonstrates the total energy variation throughout the separation process of two contacting surfaces.

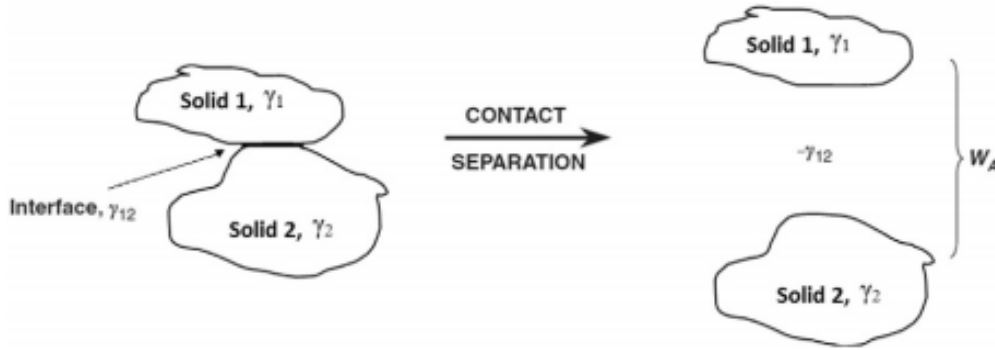


Figure 16 The work of adhesion during contact interface separation [146]

2.4.4 Surface Free Energy Calculations

Surface energy can, also, be identified as the extra energy at the surface. The surface energy of contacting solid and liquid is generally ranged between 0.05 J/m^2 to 0.2 J/m^2 . Whereas solids and vapor in contact have less than 2 J/m^2 surface energy. the distortion of solid surfaces will lead to a variation of the surface energy which is caused by the stretching of the interatomic bonds of the solid surface [146]. This distortion can be written as:

$$GS = \gamma + \frac{\partial G}{\partial A} \quad (2.12)$$

A critical situation when different phases meet together (gas, liquid, and solid). The surface energy of the material can be obtained from Young's equation which associates the surface tensions between the three phases:

$$\gamma_{SV} = \gamma_{SL} + \gamma_{LV} \cos \theta_Y \quad (2.13)$$

$$\cos \theta_Y = \frac{\gamma_{SV} - \gamma_{SL}}{\gamma_{LV}} \quad (2.14)$$

where γ_{SV} is the surface energy of solid related to vapor, γ_{SL} is the surface energy of solid related to liquid and γ_{LV} is the surface energy of liquid related to vapor and θ_Y represents Young's contact angle between the liquid and the surface which is demonstrated in Figure 17. Therefore, the contact angle can greatly influence the surface energy according to Young's equation [146].

Combining Dupre's equation with Young's equation can represent the adhesive work of solid to liquid (W_{sl}). Therefore, the contact angle between solid and liquid is directly related to the strength of adhesion which enables the measurement of the adhesion energy via the use of the contact angle [146].

$$W_{sl} = \gamma_{SV} + \gamma_{vl} - \gamma_{sl} = \gamma_{vl}(1 + \cos \theta) \quad (2.15)$$

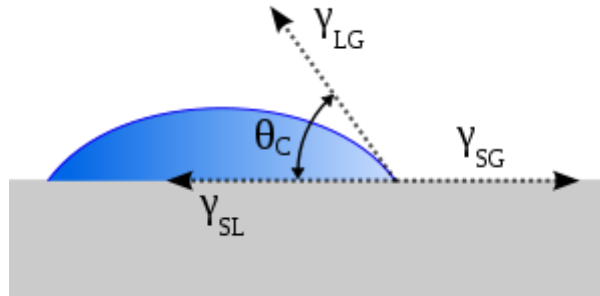


Figure 17 Diagram of surface energy on water contact angle [147]

Rough surfaces have diverse effects on the contact angles of wetting liquids. Therefore, modifying Young's equation is necessary to incorporate the practical working conditions. Wenzel and Cassie–Baxter are the two main models which attempt to define the wetting of textured surfaces.

Wenzel's model, which is demonstrated in Figure 18.a, describes the homogeneous wetting condition. The following equation for the contact angle on a rough surface can represent Wenzel's model [146]:

$$\cos \theta^* = r \cos \theta \quad (2.16)$$

where r is the roughness parameter and θ^* is the apparent contact angle. Combine this formula with Young's equation:

$$r \left(\frac{\gamma^V - \gamma^{SL}}{\gamma^{LV}} \right) = \cos \theta^* \quad (2.17)$$

The apparent contact angle (θ^*) corresponds to the stable equilibrium. θ^* is the Young contact angle for an ideal surface. The roughness ratio, (r) is a measure of how surface roughness affects a homogeneous surface. Wenzel's equation can demonstrate the contact angle of a rough surface, however, it can't represent the hysteresis present in the contact angle [148].

Cassie–Baxter model, which is demonstrated in Figure 18.b, describes the heterogeneous surface wetting condition. This is a more complex model where various materials are involved in order to measure the apparent contact angle. The following equation for the contact angle on a rough heterogeneous surface can represent the Cassie–Baxter model.

$$\cos \theta^* = r_f f \cos \theta_Y + f - 1 \quad (2.18)$$

where r_f the roughness ratio of the wet surface area and f is the contact fraction of solid surface area wet by the liquid [148] where the summation of all contact fractions equals one. This model can also be represented in the following equation format:

$$\gamma \cos \theta^* = \sum_{n=1}^N f_i (\gamma_{i,sv} - \gamma_{i,sl}) \quad (2.19)$$

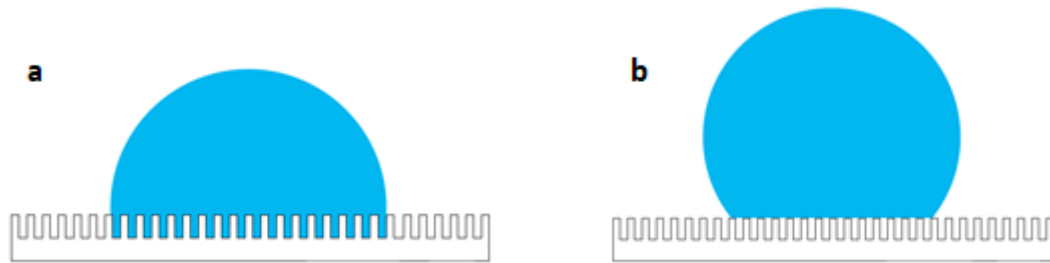


Figure 18 The wetting of rough structured surface: a) Wenzel's model b) Cassie-Baxter model [149]

2.5 Establishment of Problem

Energy harvesting applications such as PV panels have a great requirement for the solar radiation to pass through the surface which makes the enhancement of optical transmittance a major factor when creating self-cleaning surfaces. The process of generating a hydrophobic surface creates surface textures that minimize the incident optical radiation via scattering, diffusing and partial absorption. Improving the optical transmittance of the textured surface can be achieved via introducing optically matching fluids, such as oils. The sliding velocity of the water droplet which travels on top of the oil film has a major role in mitigating the dust particle which is disposed of on the surface. The sliding velocity is affected by the volume of the water droplet, the tilting angle of the surface, and the shear rates through the water-oil boundary. The mitigation of the dust particle can, also, be affected by the oil and water infusions over the surface of the dust particle. The dust particle can be, successfully, mitigated when the water infusion height is greater than the oil infusion height. Therefore, the study of particle mitigation from the oil-impregnated optically transparent surface becomes essential.

The sliding droplet's dynamic behavior over the silicone oil film, which is situated on the crystallized PC surface, is inspected. Furthermore, the dust removal mechanism exhibited by the sliding water droplet is examined. The spreading factor of silicone on the crystallized PC surface and the silicone oil infusion over the dust particles are examined. Furthermore, the effect of the oil film thickness and the orientation of the dust particle on the mechanisms of dust particle mitigation. The effect of silicone oil impregnation on the optical transmittance of the surface is evaluated by observing the resulting changes of the surface transmittance.

CHAPTER 3

RESEARCH METHODOLOGY

The major drawback of crystallized PC is the degradation of the surface transmittance. The crystallization of the PC surface creates the Nano-pillars which are the main cause of converting the PC surface into a hydrophobic surface. The space created between these Nano-pillars is also responsible for the degradation of the surface transmittance. This chapter explains the necessary apparatuses and procedures to study the methods proposed to mitigate the issue of surface transmittance degradation and the aftereffects of these procedures on the hydrophobic surface. The Process of enhancing the optical transmittance of an Acetone treated PC wafer goes through the following stages. The first stage requires the production of the hydrophobic PC surface and the study of the resulting characteristics of the surface. The second stage goes toward replicating the resulted PC surface using PDMS and the study of the effect this process brings to the surface characteristics. The final stage is achieved by introducing silicone oil to the surface and the study of its influence on the surface and the dust removing mechanism.

3.1 Apparatuses

Achieving the desired objective requires the use of various apparatuses to perform several mechanical, chemical, and physical procedures. These procedures performed in the study include the crystallization of the PC surface, surface, and dust particle characterization and the analysis of the droplet dynamics on the hydrophobic surface.

3.1.1 Cutting Machine

The preparation of PC wafers required to create the crystallized hydrophobic surface encompasses the procedure of cutting the PC plate into small PC wafers. This Procedure utilizes the Vertine universal band sawing machine. The hydraulically powered machine has a cutting capacity of 350 mm and a 16 mm width saw blade. The workplace table of the machine has a size of 500 x 400 mm.

3.1.2 Grinding Machine

The preparation of PC wafers required to create the crystallized hydrophobic surface encompasses the procedure of grinding and polishing the PC wafers' edges. This Procedure utilizes the MoPao 160E Metallographic sample grinding-polishing machine. The machine is suitable for pre-grinding, grinding, and polishing metallographic specimens using various grinding plates. The machine is equipped with a cooling system that prevents overheating and damage to the specimen. The machine, which has a microprocessor adjustable speed, can operate at a revolution speed of 50 to 600 rpm.

3.1.3 SEM Field Emission –Scanning Electron Microscopy (FE-SEM)

FE-SEM is a machine used to investigate the microstructure, morphology examination, and chemical composition of the test specimen. FE-SEM is an advanced scanning technology that utilizes field emission to convey an extremely magnified schematic of the test surface structure in order to ensure a more accurate analysis. A JEOL 6460 scanning electron microscope with a field emission, resolution of 10 nm, beam voltage of 0.4 - 40 kV, and magnification of 10× to 300 000× was employed.

This technique provided magnified SEM micrographs for clean and dusty crystallized poly-carbonate surfaces. Nevertheless, using this machine may require additional steps, such as the gold coating technique, to prepare the samples for the test procedure.

3.1.4 Mechanical Pipette

The water droplets utilized in the experiment were controlled by Transferpette® S Pipette. This mechanical dispenser was utilized due to its high degree of accuracy, four-digit volume display, easy calibration technology, and superior auto-cleavability. The droplet volume can be controlled for various procedures with a volume step resolution of 0.1 μL .

3.1.5 X-Ray Diffraction (XRD)

XRD is an analytical characterization method utilized to identify the phase of the crystalline samples. This characterization method is utilized in inspecting the various elements contained in the environmental dust particles. The apparatus mainly consists of the X-ray tube, the detector, and the sample holder.

The utilized XRD equipment was the D8 advanced diffractometer model which was manufactured by Bruker, USA. It performs the analysis with $\text{CuK}\alpha$ radiation at default settings of 30 mA, 40 kV and a ranged scanning angle (2θ) between 20° - 90° .

3.1.6 Fourier-Transform Infrared Spectroscopy (FTIR)

FTIR uses infrared radiation which is transmitted or absorbed by the sample. This apparatus is comprised of an interferometer, energy source, sample holder, and light detector. The acquired spectrum indicates a molecular fingerprint of the examined

specimen. This analysis delivers various information which includes: detecting unidentified materials, the consistency or quality of a specimen, and the number of components in a mixture.

3.1.7 Goniometer

The apparatus has the ability to measure the contact angle between the solid surfaces and the water droplet. This contact angle, consequently, expresses the wettability of the solid surface by a liquid via incorporating Young's equation. The test utilizes controlled volume water droplets dispensed in various locations on the test surface and repeated to obtain a more accurate reading.

3.1.8 3D Optical Microscope

The 3D optical microscope is a white light interferometry microscope that forms comprehensive three-dimensional pictures through the use of the light photons beam. 3D imaging can offer a graphic inspection of the sample surface which can provide a comparison technique to assess the differences between the clean and dusty samples. This procedure can demonstrate the effectiveness of the water droplet cleaning method. Furthermore, the apparatus can be utilized to perform metrology applications of surfaces, obtain quantitative measurement and provide non-contact measurement.

3.1.9 UV Transmittance

The apparatus utilized for this procedure is a spectrophotometer which has the Jenway model 6705 scanning UV or visible light. This device has the ability to measure reflectance via the use of a single-point detector. The apparatus has the ability to identify

the transmittance and absorbance of the sample surface at a particular wavelength. The components of the apparatus comprise of sample chamber, filter wheel light source monochromatic, and detection system. The optical properties of the manufactured hydrophobic, clean and dusty, surfaces can be assessed using the UV transmittance measurements.

3.1.10 High-Speed Camera

High-speed cameras are high specification cameras that are specially designed to capture slow-motion videos. This allows for smaller details to be clearly demonstrated which, consequently, aids in engineering analysis where minor changes responsible for certain effects occur at high speeds which typical video cameras can't capture. Utilizing this type of camera can clearly show the dynamic motion of a water droplet on an inclined hydrophobic surface. It can, further, show the cloaking process of the dust particle. The main high-speed camera used in most of the test procedures has the SpeedSense 9040 model and is manufactured by Dantec Dynamic in Denmark. Some procedures utilized the. SpeedSns camera has the ability to obtain 1000 fps (frame per second) and the disadvantage of capturing black and white footage only. Whereas, the high-speed camera function of an iPhone mobile has the ability to obtain 240 fps and the advantage of capturing colored footage. Higher fps which results in more obtainable details and colored footage can each be utilized to fit the requirements of different test procedures.

3.1.11 Computational Facility

A high Processing computer is required to perform the various analytical calculations required in this study. The utilized computer has the Intel(R) Core (TM) i7-6700 CPU with a processing speed of 3.41 GHz. It also has an installed Ram of 8.00 GB which allows the analytical calculations of COMSOL to be performed. Obtaining the experimental footage from the high-speed camera requires the use of Phantom's PCC 2.14 program. Analyzing the droplet dynamics requires the use of Tracker and Excel Programs.

3.2 Experimental Procedures

The study of the various effects of introducing the crystallized hydrophobic surface goes through different experimental procedures. Modifying the surface texture, replicating the surface, and introducing the silicone oil to the hydrophobic surface require the usage of various experimental procedures as well. These Procedures are summarized in this section to understand the source of the obtained results in this study.

3.2.1 Sample Preparation

PC sheets are difficult to handle in a study that focuses on the microscopic level. The first issue is to prepare samples in appropriate sizes which can be later utilized to study the effects produced on the surface texture. Therefore, The PC sheet is cut into 7 x 3 cm wafers using the Vertine universal band sawing machine. The edges of these wafers are subsequently grinded and polished using the MoPao 160E Metallographic sample grinding-polishing machine. This procedure is performed in order to observe the resultant

characteristics of the surface with ease. The samples are cleaned with soap and water and dried using an air jet.

3.2.2 Crystallization of PC Surface

Modifying the surface texture of the PC surface can be achieved using the one-step method of immersing the PC wafer in an Acetone bath. The properties of Acetone used in this experiment are demonstrated in table 2. In order to optimize the usage of Acetone, water is used to calibrate the amount required to immerse PC wafers in the bath. The PC wafer needs to be immersed in the Acetone bath steadily for a period of time which is realized by utilizing a 3D designed base that can perform such a task. Next, the wafer needs to be cleaned with distilled water and immediately dried using an air jet. From repeated experiments, it's found that the air jet velocity which is used to dry the sample plays an extremely important role in the finished product. Higher air jet velocity produces a surface with a higher contact angle and lower transmissibility, whereas, lower air jet velocity produces the opposite effect. The most difficult part of this method is that the handling of the sample during the procedure which requires a great deal of caution. The sample surface should never come in contact with the fingers of the technician who is performing the procedure which prompts the need to grab the sample carefully by its edges. It's further preferred to always handle the sample by the corners during the procedure.

The properties of the main materials utilized in this procedure have inherent advantages and deficiencies which may require careful treatment. Polycarbonates (PC) are a group of thermoplastic polymers containing carbonate groups in their chemical structures. PC is a form of plastic that is both strong and lightweight; however, it's also very susceptible to

scratching. It weighs less than both acrylic and glass; however, it's more expensive than either of these materials. It is frequently used to produce bulletproof windows. The most common products of PC are DVD and CD.

Acetone is a colorless liquid which is also known as Propanone. It's a solvent used in the manufacture of plastics, cosmetics, and personal care. Nail polish removers are the most common application of Acetone. This liquid occurs naturally in the human body as a byproduct of metabolism. Acetone can easily mix with water and evaporates quickly in the air. Acetone is generally recognized to have low acute and chronic toxicity. Therefore, the process of immersing the PC wafer in the Acetone bath is performed in a fume hood where the exposure to hazardous or toxic fumes is limited.

Table 2 Acetone Technical Data Sheet

Property	Value
Molecular Weight (g/mol)	58.08
Boiling Point @ 760 mmHg, 1.01 ar	56.3°C (133.3 °F)
Flash Point (Setaflash Closed Cup)	-18°C (-0.4°F)
Freezing Point	-94.7 °C (-138°F)
Vapor pressure@ 20°C — extrapolated	182 mmHg
Specific gravity (20/20°C)	0.792
Liquid Density @ 20°C	0.79 g/cm ³
Vapor Density (air = 1)	2
Viscosity (cP or mPa•s @ 25°C)	0.33
Surface tension (dynes/cm or mN/m @ 25°C)	23.1
Specific heat (J/g°C @ 25°C)	2.44
Autoignition temperature	465 °C (869 °F)
Evaporation rate (n-butyl acetate = 1.0)	14.4
Solubility, @ 25°C Solvent in water (%)	100
Hansen solubility parameters	
_Total	9.8
_non-polar	7.6
_Polar	5.1
_Hydrogen bonding	3.4
Partition Coefficient, n-octanol/water (log Pow)	-0.24
Flammable limits (vol.% in air) Lower	2.15

3.2.3 Surface Characteristics

The texture characteristics of the surface are analyzed using various testing procedures in order to determine the wetting state and topology of the resulting surface. The tests which are carried include the use of scanning electron microscope, X-ray Diffraction, goniometer, 3D optical imaging, and UV transmittance. The texturing process is optimized towards the surface topology resulting in a hydrophobic wetting state with low contact angle hysteresis.

SEM requires the sample to be gold coated in order for the apparatus to be able to clearly capture the surface topology which is a destructive procedure for the other tests. Therefore, the other procedures are carried out first. Utilizing the goniometer, we can place the test sample on top of the worktable where the orientation in 3D degrees of freedom can be manipulated. The device can steadily release a dispensed water droplet of controlled size on the test surface where the magnified image of the droplet and its contact to the surface is captured. The contact angle obtained can be further utilized to obtain the surface tension of the test sample via incorporating the young's equation. The 3D optical imaging is carried out by placing the test sample on top of the worktable where the orientation in 3D degrees of freedom can be manipulated. Using the attached program, the lenses of the apparatus are controlled to have a focused image of the surface texture. Upon starting the test procedure, the apparatus captures various 2D images at adjacent heights and collects these images to provide the 3D model of the surface texture of the test sample. XRD is carried by directing a laser beam at the surface of the test sample where it's reflected by the molecule structure of the test sample at a certain degree angle which is later determined by the detector. These angles express the molecule

crystalline structure of the test sample which can be further analyzed to determine the elemental components of the surface. The UV transmittance of the surface can be obtained by first carrying the test procedure for an empty chamber to calibrate the apparatus. The procedure then continues by placing the test sample in the enclosed chamber of the apparatus where a laser beam of varying wavelength is released on the test sample and its reflectance is determined. The machine then records the varying transmittance for the varying wavelength. A fixture was designed and built to hold the oil-impregnated sample while enabling tilting the sample at the required angle. A high-speed system (Dantec Dynamics SpeedSense 9040) was employed to obtain the droplet movement over the impregnated oil surface.

3.2.4 Dust Picking Mechanisms

A test setup is designed to analyze the dynamics of the water droplet on top of varying surface textures (Figure 19). The test sample is placed on a 3D printed base where the inclination of the test sample can be controlled. The mechanical dispenser is fixed at the top position of the inclined test sample using a support stand. A high-speed camera is utilized to capture the dynamic motion of the water droplet and its connection to the surface of the test sample. The process is carried out for various droplet volumes and sample inclination angles. Similar test procedures with minor changes are carried for crystalline PC, PDMS replicated, and oil-impregnated surfaces where the test surface is observed for clean and dusty surfaces. The images collected by the high-speed camera are transferred to the computer using the attached program where further analysis of the droplet dynamics is performed using the Tracker program. The polycarbonate (p-hydroxyphenyl) sheets were cut in $30 \times 60 \times 1$ (width \times length \times thickness) mm³ preparing

the samples. Diluted acetone (30% by volume) solution is prepared and samples were immersed into acetone solution for four minutes towards the crystallization of the surface. The crystallized surfaces were analyzed in terms of texture properties and wetting. for the sliding of the water droplet on the oil-impregnated surface. The recording system was operated at 8,000 frames-per-second (fps) with a high image resolution (1280 × 800) and the pixel had 14 μm × 14 μm size. The sliding droplet repetitions were estimated through the experimental repeats while the error resulted was within 3%. The experimental uncertainty ($\pm u$) related to the droplet height/width and speed was assessed incorporating the experimental repeats. The confidence level of 96% was obtained from the repeats of experiments and the standard uncertainty (σ_u) was determined via [150]:

$$\sigma_u = \sqrt{\int_{x_0}^{x_n} (x - \mu_e)^2 p(x) dx} \quad (3.1)$$

where μ_e represents the expected mean value of x (measured response), n is the number of points in measured data, and $p(x)$ corresponds to the probability distribution function, which was evaluated from the instantaneous correlation plane while adopting all recorded data for sliding droplet. To determine the probability distribution function diameter, the data distribution was fitted in a Gaussian function and the standard uncertainty was obtained via Eq. 3.1. The final estimation was normalized by the total pixel numbers that contributed to the cross-correlation peak. Moreover, the bias uncertainty of 0.04 pixels was adopted because of the complexities in evaluating the extremely small peaks in the probability distribution function. The standard uncertainty was found at 3%.

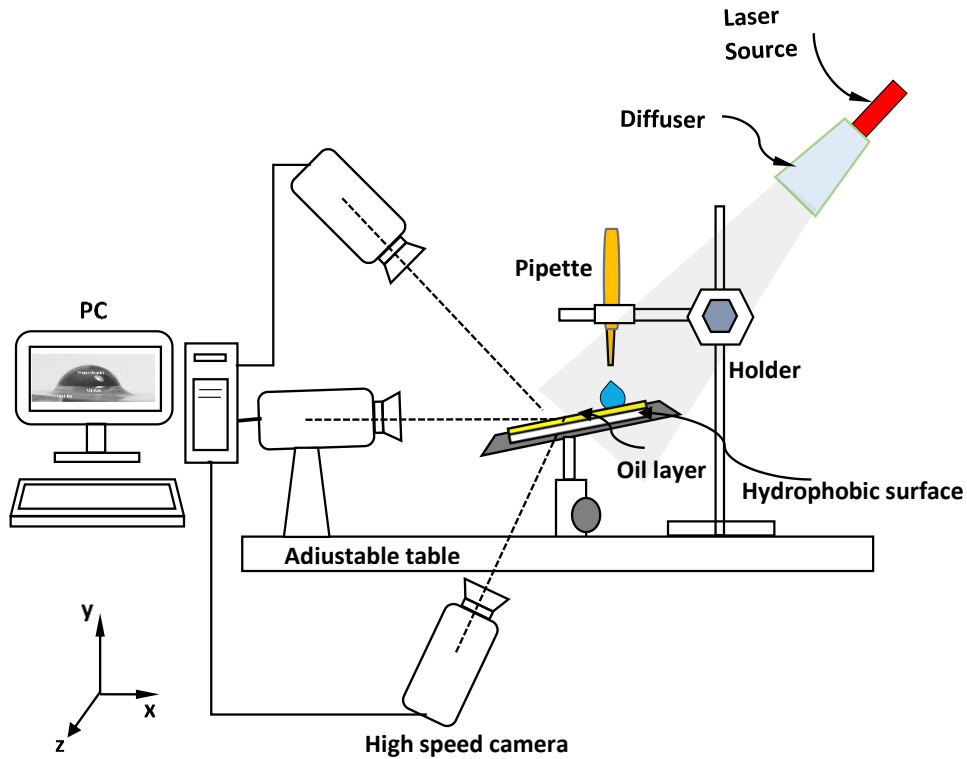


Figure 19 Demonstration of the experimental set-up

3.2.5 Poly-di-methyl-siloxane (PDMS) Replication of Crystallized Surfaces

The surface resulting from the crystallized PC has the issue of extremely lowering the optical transmittance of the surface. In order to enhance the transmittance of the surface, the liquid casting technique is used to replicate the surface topology. This technique utilizes the characteristics of PDMS to copy the surface texture. Before starting the procedure, a boundary cover to prevent the liquid from dispersing is placed upon the resulted PC surface. The resulted PC surface has a curvature towards the center. Covering the air gap in the cover which is a result of the surface curvature can be accomplished using a glue gun. The procedure starts when the PDMS liquid is mixed with a catalyst in a ratio of 10 to 1. The mixture needs to be stirred extensively in order to remove the air pebbles in the mixture. The mixture is placed on top of the surface texture which needs to

be copied to produce the image of the surface. Different heat treatments are performed to produce optimal conditions for this process. The mixture is left at room temperature for various times periods 0, 24, and 48 hrs. respectively. The mixture is, then, placed in an oven at 50 °C for 2 hrs. The mixture which is now in a solid form is peeled off the PC surface. The produced PDMS surface represents the image of the surface of interest. The previous procedure is repeated to create the original surface. The characteristics of the resulting surface including the optical transmittance are analyzed using similar analytical tools. A general illustration of a PDMS replication procedure through the liquid casting technique is shown in Figure 20.

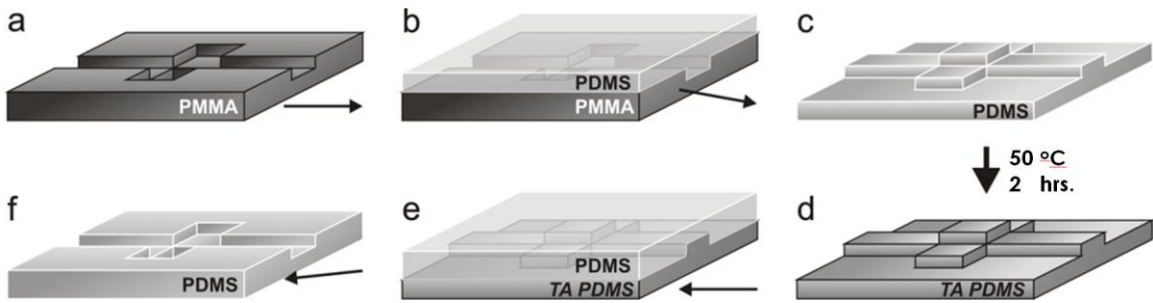


Figure 20 Poly-di-methyl-siloxane (PDMS) replication through the liquid casting technique

This procedure, while indeed providing a minimum enhancement to the optical transmittance of the surface, created many defects for the surface texture which resulted in a 4% reduction of surface contact angle and limited the motion of a water droplet on the surface. The copied surface texture had important details at the Nano level where the inherent deficiencies of the simple procedure of peeling the PDMS sample after the replication can be clearly observed.

3.2.6 Silicone Impregnated Surfaces

Further improvements to the optical transmittance are necessary. Achieving this can be done by applying a Nano-layer of silicone oil on the surface of the test sample. The silicone oil with a viscosity of 10 cst, density 935 kg/m^3 , and surface tension 35 mN/m was used to impregnate the crystallized sample surfaces. The dip-coating procedure was used for the oil impregnation of the surfaces of samples. The silicone oil impregnation is carried multiple times from various angles to ensure the complete coverage of the surface texture. This will result in a thick layer of silicone oil which doesn't serve the purpose of the study. Therefore, the resulting oil film is thinned by inclining the sample surface at a right angle for various time periods where it was convenient to utilize the 24 hrs and 1 hr period which later corresponded to 50 and $700 \text{ }\mu\text{m}$, respectively. The oil film thickness was evaluated via ellipsometer (M-2000 J.A. Woolam Co.) during each impregnation test. The ellipsometer measurements relied on the polarization of the incident monochromatic light onto the oil film. The film thickness measured was about $0.7 \text{ }\mu\text{m}$ with the roughness of the oil film being 0.42 nm . Oil impregnation of the surface was performed in order to observe the effect of oil thickness on the resulting characteristics of the surface. Silicone oil cloaking of dust particles and cloaking velocity is measured using a high-speed camera. Similarly, water cloaking for the dust particles is analyzed and the cloaking velocity is also measured using the high-speed camera. The water droplet behavior on silicone oil-impregnated surfaces is examined using the previous experimental procedures. The water droplet and silicone oil cloaking of the dust particles are, further, analyzed simultaneously and possible mechanisms for dust particles removed by the water droplet from the silicone oil deposited surface are explored. It should be noted that

if the cloaking velocity of the silicone oil becomes greater than that of the water, the particles will remain entrapped by the silicone oil film. Hence, the assessment of cloaking velocities of dust particles due to silicone oil and water remains critical for self-cleaning applications of the resulting surface.

CHAPTER 4

FORMULATION OF SLIDING DROPLET

4.1 Numerical Analysis

Incompressible flow is considered to simulate the flow field developed in the droplet fluid and the silicone oil film using the conditions of the experiment. To adopt a two-phase flow situation resembling oil and water phases, Arbitrary Lagrangian-Eulerian (ALE) moving mesh formulation is incorporated in the simulations. Since there is no external thermal influence (heating) and the flow system is assumed to be in temperature equilibrium (as monitored by a thermal camera, the change in temperature during the experiment is negligible), an isothermal flow condition is considered. Hence, the continuity and momentum equations of flow being utilized in the computation can be expressed as follows:

$$\nabla \cdot \bar{u} = 0 \quad (4.1)$$

$$\rho \frac{\partial \bar{u}}{\partial t} + \rho(\bar{u} \cdot \nabla)\bar{u} = \nabla \cdot [-p\bar{I} + \mu(\nabla\bar{u} + (\nabla\bar{u})^T)\bar{I}] + \bar{F}_g + \bar{F}_b \quad (4.2)$$

$$\bar{F}_g = \rho\bar{g} \quad (4.3)$$

$$\bar{F}_b = \rho_{si} \cdot \bar{g} \cdot \frac{V_{disp}}{V_d} \quad (4.4)$$

where: ρ is density, \bar{u} is velocity, \bar{g} is acceleration vector due to gravity, p is gauge pressure, μ being viscosity, \bar{F}_g represents gravitational force per unit volume, \bar{F}_b is the

buoyancy force which acts only in the droplet domain, ρ_{si} is the density of silicone oil, V_{disp} is the displaced volume of the oil layer, V_d is the droplet volume, and t is time.

4.1.1 Initial conditions

Initially, both the droplet and oil layer are considered to be at rest, i.e. the velocity is considered as zero. However, because of the gravitational influence, surface tension, and buoyancy forces, the water droplet and oil layer start moving along the inclined plane. Hence, the simulation of the flow field developed in the droplet, and the oil layer is carried out for the droplet sliding action on the oil. The initial pressure in the droplet fluid is taken as the Laplace pressure and the study is conducted for the oil surface inclination angle of 4° .

4.1.2 Boundary conditions

As demonstrated in Figure 21, the droplet and oil external boundaries (i.e. boundary (3)) are defined to have a constant pressure that is equal to the atmospheric pressure. At the interface of the film and the surrounding air, velocity and pressure continuity are assumed to satisfy the continuity and momentum transfer. Symmetry boundary conditions are defined at boundaries (2) and (4) (i.e. Eq. 4.8 - Eq. 4.10). Inlet and outlet boundary conditions are applied at the boundaries (1) and (5) according to the velocities predicted from the experiments (i.e. Eq. 4.6 and Eq. 4.7).

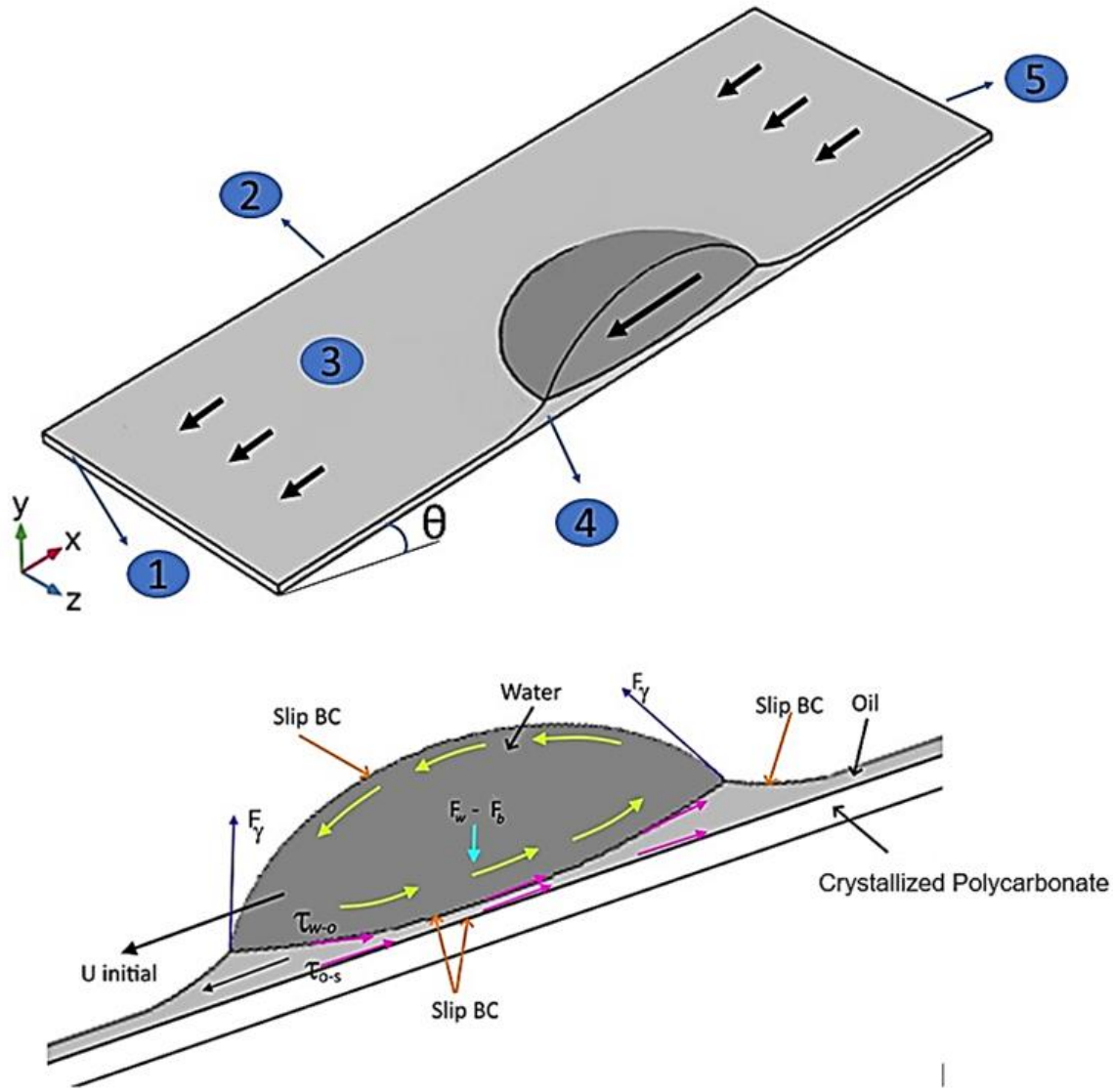


Figure 21 View of sliding droplet on an inclined impregnated oil film. The boundary conditions as marked 1 to 5

4.1.3 Flow Equations

The fluid domains are considered to be freely deformable and the water-oil/oil-solid interfaces are considered to have the Navier slip boundary condition which allows for a non-zero velocity at the contact line that is proportional to the local shear-stress (i.e. Eq. 4.8, Eq. 4.9 and Eq. 4.11). For the water-oil interface, the slip length is estimated by balancing the shear stress at the interface resulting from the change in interfacial

velocities on the water and oil sides. Therefore, the Marangoni shear is considered at the interface as expressed in Eq. 4.12.

On the other hand, the slip length at the oil-solid interface mainly depends on the texture characteristics of the hydrophobic surface. A good estimation comes from:

$$b \sim \frac{\mu}{\mu_o} (1 - \phi) h_t \quad (4.5)$$

where μ represents droplet liquid (water) viscosity, μ_o is the silicone oil viscosity, ϕ is the solid fraction of the crystallized surface, and h_t is the thickness of the film [151]. Hence, the following boundary conditions were adopted for the simulations:

$$\bar{u} = -U_0 \bar{n}_{inlet} \quad (\text{Oil inlet velocity}) \quad (4.6)$$

$$\left(-p\bar{I} + \mu(\nabla\bar{u} + (\nabla\bar{u})^T) - \frac{2}{3}\mu(\nabla\bar{u})\bar{I} \right) \cdot \bar{n}_{wall} = -p_0 \bar{n}_{outlet} \quad (\text{Oil pressure outlet}) \quad (4.7)$$

$$\bar{u} \cdot \bar{n}_{wall} = 0 \quad (\text{No penetration at wall}) \quad (4.8)$$

$$\bar{K} = \left(-p\bar{I} + \mu(\nabla\bar{u} + (\nabla\bar{u})^T) - \frac{2}{3}\mu(\nabla\bar{u})\bar{I} \right) \cdot \bar{n}_{wall} \quad (4.9)$$

$$\bar{K} - (\bar{K} \cdot \bar{n}_{wall})\bar{n}_{wall} = 0 \quad (\text{Slip condition on exterior \& symmetry boundaries}) \quad (4.10)$$

$$\bar{\tau}_{wall} \cdot \bar{T} \cdot \bar{n}_{wall} = -\frac{1}{\beta} \bar{u} \cdot \bar{\tau}_{wall} \quad (\text{Navier-slip boundary conditions}) \quad (4.11)$$

$$(\bar{n}_{wall} \cdot \tau)_o = (\bar{n}_{wall} \cdot \tau)_w F_{st} \quad (\text{Shear stress at interface}) \quad (4.12)$$

where: \bar{n}_{wall} is the unit normal vector at the slipping boundary, $\bar{\tau}_{wall}$ is the unit tangential vector at the slipping boundary, \bar{I} is the identity tensor, U_0 is the oil inlet velocity, p_0 is the oil outlet pressure, τ is the stress tensor ($N m^{-2}$), F_{st} is the surface tension force, and \bar{K} is related to the curvature of the boundary.

The surface tension force can be expressed as:

$$F_{st} = \gamma_{o-w}(\nabla_{int} \cdot n_{wall})n_{wall} - \nabla_{int}\gamma_{o-w} \quad (4.13)$$

where: $\gamma_{o-w}(\nabla_{int} \cdot n_{wall})n_{wall}$ is the interfacial force per unit area, γ_{o-w} is the droplet-oil surface tension, and $\nabla_{int}\gamma_{o-w}$ is the tangential stress.

4.2 Numerical Implementation

The governing equations, initial and boundary conditions for the study are implemented in the commercial finite element package (COMSOL Multiphysics software). Table 3 gives the silicone oil and water properties incorporated in the computations.

Table 3 Properties of silicone oil and water used in the computation

Property	Silicone Oil	Water
Density (ρ) kg/m ³	935	1000
Viscosity (μ) Pa.s	0.92×10^{-2}	0.7644×10^{-3}

The droplet and oil ridge geometries at different locations are examined experimentally through the recorded data. Consequently, the droplet and oil ridge geometries are reconstructed from the images obtained with the high-speed recording system, and the numerical study is conducted with the reconstructed and meshed geometries as demonstrated in Figure 22. The ALE two-phase (water-oil) flow system is adopted for the study and the computation is carried out in a 3-dimensional coordinate system. However, to reduce the computational efforts and expensive meshes used in the simulations, the equations are solved utilizing the 3D plane symmetry of the geometry.

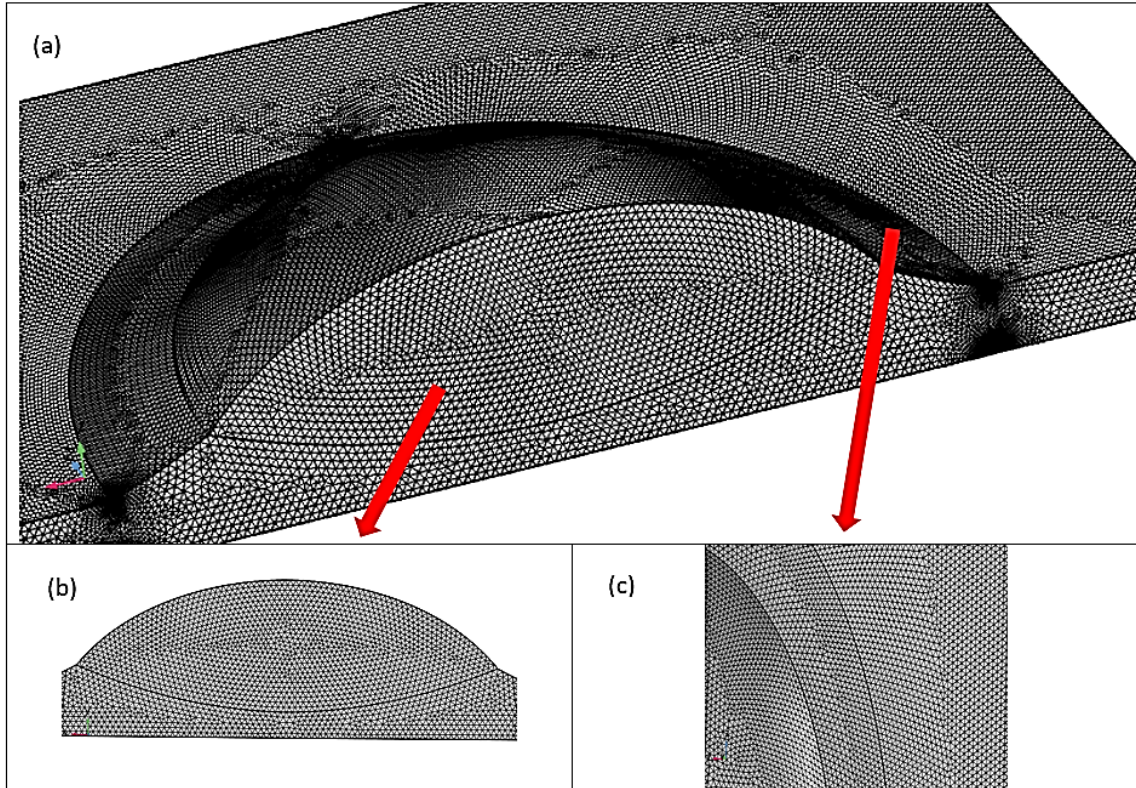


Figure 22 Meshes used in the simulations: a) mesh distribution in three-dimensional feature, b) mesh distribution at droplet and oil film sections, and c) mesh distribution in the oil rim and water droplet surrounding region

The second-order Euler backward difference scheme is used to discretize the time derivatives in the flow equations. The numerical accuracy of the approach is limited by the mesh volume and time increment. Hence, a time step as small as 10^{-8} s is adopted for the numerical solution ensuring the convergence of the time derivatives. The computational domain is meshed with second-order (or quadratic) tetrahedral elements which are illustrated in Figure 22 and the grid-independent tests demonstrate that the solution for the velocity field and pressure converged with 341,297 elements as shown in Figure 23.

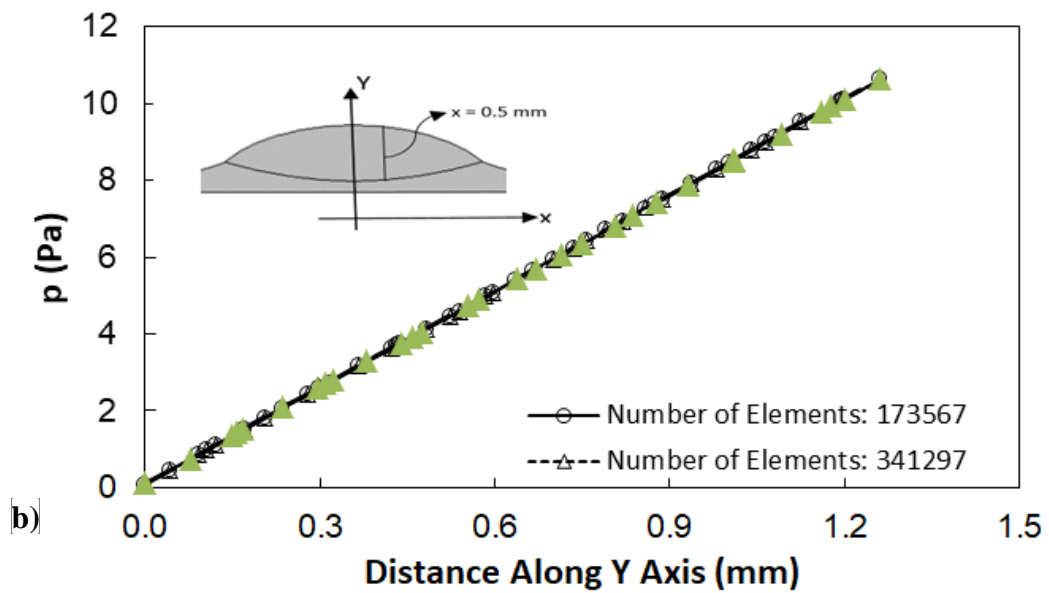
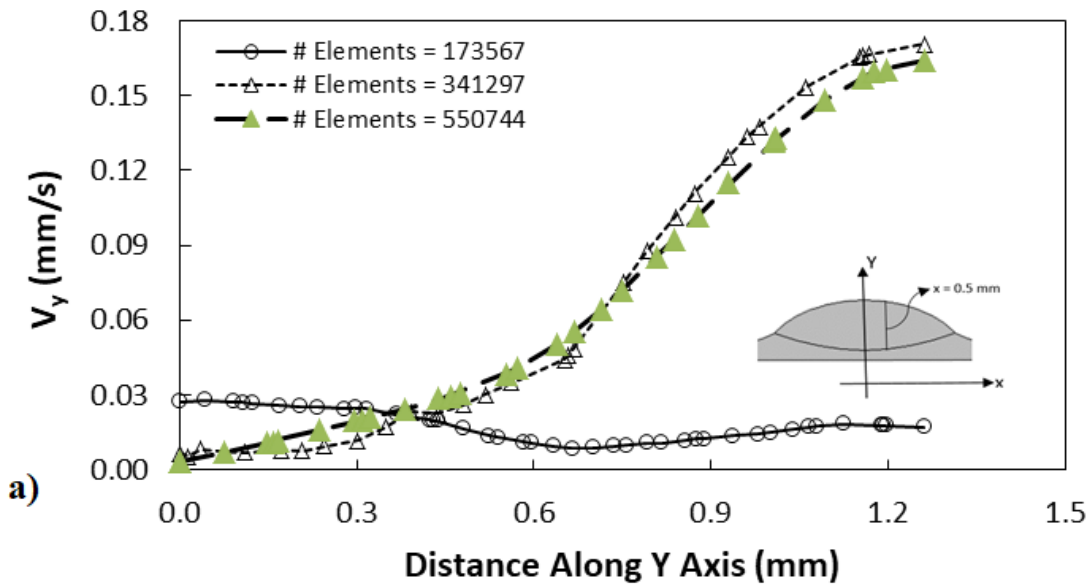


Figure 23 Grid independent test results along y-direction at $x = 0.25$ mm away from droplet centerline for different mesh sizes: a) velocity distribution, and b) pressure variation

4.3 Analytical Treatment

The initial shape of the droplet emerging from the oil film forms a spherical cap and the cap geometry has a water-oil-air contact rim of the radius of

$$r_o = \sqrt{(2r_d - h_o)h_o} \quad (4.14)$$

where h_o represents the cap height from the oil surface, r_o is the cap radius, and r_d is the droplet radius that represents the cap height resembled.

4.3.1 Force Analysis

The force balance provides the volume of an immersed droplet in the oil, which is

$$F_\gamma \sin(\theta_c + \alpha) + F_B - W = 0 \quad (4.15)$$

where F_γ represents the force of surface tension, F_B is the buoyancy force, and W is the droplet weight force. Here, α is the contact angle around the rim (water-oil-air contact line) and θ_c is the filling angle representing the rim angular location about the vertical (normal) axis [151]. The balance of forces along with the vertical direction results in:

$$2r_o\gamma_{-si} \sin(\theta_c + \alpha) + \frac{1}{3}(4r_{d0}^3 - h_o^2(3r_o - h_o))\rho_{Si}g - \frac{4}{3}\rho_w g r_{d0}^3 = 0 \quad (4.16)$$

where ρ_{Si} is the density of silicone oil, γ_{-si} is interfacial resistance between silicone oil and droplet water. The cap-height (h_o) of the droplet can be estimated via combining Eq. 4.14 and Eq. 4.16. Subsequently, the rim radius (r_o) can be determined from Eq. 4.14. For 30 μ L droplet ($r_d \cong 1.84$ mm), $r_o = 1.8$ mm and $h_o = 1.48$ mm can be obtained from the force balance equation. The close examination of the experimental data reveals $r_o \cong 1.78$ mm and $h_o \cong 1.46$ mm for 30 μ L droplet. Hence, predictions from the formulation give close values to the experiments.

4.3.2 Velocity Analysis

The inclination of the crystallized sample results in the flow of impregnated oil in the direction of inclination (δ) because of the gravitational effect. The energy potential of oil on the inclined surface for the inclination angle of $\delta \leq \pi/2$ is related to the capillary number, $Ca = \frac{\mu_o u}{\gamma_o}$, where u is the oil velocity and μ_o is silicone oil viscosity [155]. The

variation of the oil velocity ($\frac{\partial h_f}{\partial t}$) on the inclined sample can be formulated through:

$$\frac{\partial h_f}{\partial t} = \nabla \cdot [h^3 \nabla \nabla^2 h_f] - L_D \nabla \cdot [h^3 \nabla h_f] + \frac{\partial h_f^3}{\partial x} = 0 \quad (4.17)$$

$$h_f = \bar{h}_f / h_c \quad (4.18)$$

$$L_D = (3Ca)^{1/3} \cot \delta \quad (4.19)$$

where h_f represents the non-dimensional thickness of the film, \bar{h}_f is the thickness of the film, h_c corresponds to the thickness in film upstream, x is the space variable on the inclined film surface, L_D represents the non-dimensional variable, Ca is the capillary number, and δ is the film inclination angle [157]. The analytical solution of equation (4.17) which solves for the oil film velocity is difficult to obtain; however, the method used by Yilbas et al. [158] is incorporated to obtain the oil film velocity. Hence, the oil film velocity becomes about 0.019 mm/s for the inclination angle of 4° . The experimental measurement of the oil film velocity for 4° inclination angle, using a tracker program incorporating the high-speed recorded data, is about 0.016 mm/s; hence, the velocity predictions and measurements are closer in values.

On the other hand, the flow of oil film and partially immerse/floating water droplet motion do not possess the same velocities. This creates a viscous shearing acting on the droplet while modifying the droplet motion on the oil film. In addition, the crystallized

polycarbonate surface has a surface texture consisting of micro/nano spherulites and fibrils and as the film thickness becomes less downstream of oil film flow, the water droplet can contact the textured surface. This gives rise to a slip condition, because of the hydrophobic nature of the crystallized surface, over the area of contact and the slip length, mainly, depends on the texture parameters such as solid fraction [154], [159]. The slip length (b) can be obtained from Eq. 4.5. The solid fraction (ϕ) of the crystallized surface can be evaluated from atomic force microscopy data, which is about $\phi = 0.35$. Since droplet fluid and silicone oil viscosities are 0.7644×10^{-3} Pa.s and 0.92×10^{-2} Pa.s, respectively [160], and the oil thickness is about 0.7 mm, the slip length yields about $b = 37 \mu\text{m}$. The slip velocity (u_s) is correlated to slip length through

$$u_s = \frac{b}{\mu} \tau_{w-i} \quad (4.20)$$

where τ_{w-i} is the interfacial shear stress between the droplet and crystallized surface [151], which could be streamlined by the Couette flow analogy in terms of the film velocity (u_f), hence, it yields

$$u_s \sim \frac{b}{h_t} u_f \quad (4.21)$$

Because of the difference in velocities of the droplet and the film, shear can be formed over the immersed surface of the droplet while influencing the droplet motion in the film. The shear stress on the water droplet surface can be approximated by:

$$\tau_{w-i} \sim \mu \frac{(V_d - u_f)}{l_m} \quad (4.22)$$

where V_d is droplet velocity and l_m represents the space between the water droplet base and the mass center of the droplet [161]. In addition, the shear stress at the film-crystallized-solid interface is about

$$\tau_{w-i} \sim \mu_o \frac{(u_f - u_s)}{h_t} \quad (4.23)$$

Moreover, the shearing stress at the water droplet and the oil at the interface must have the same order; hence, linking the shear across the water-oil film at the interface yields:

$$\frac{V_d}{u_f} \sim 1 + \frac{\mu_o}{\mu} \frac{l_m}{h_t} \left(1 - \frac{b}{h_t}\right) \quad (4.24)$$

However, the value of the term b/h_t is about 0.052 and $\frac{\mu_o}{\mu} \frac{l_m}{h_t} \gg 1$; therefore, the relationship results in the higher droplet velocity than the film velocity ($V_d > u_f$), which is also noted from the experimental data. Due to the shear created at the droplet-oil interface, the droplet suffers from the pinning due to the silicone oil ($V_d > u_f$). Hence, the work is done by the droplet against the pinning (W_L), which can be expressed as:

$$W_L = 2\pi\gamma_{w-o}r_o \cos(\theta_c + \alpha)\Delta L \quad (4.25)$$

where ΔL is the length scale within the inclined oil surface [152]. Moreover, during the water droplet motion, additional energy dissipation takes place because of the interfacial fluid resistance at the ridges of the oil rim formed around the droplet because of oil infusion on the droplet surface, the air drag over the droplet cap, and lateral component of the oil surface tension around the rim.

4.3.3 Energy Analysis

The energy dissipated due to viscous influence is related to [162]:

$$E_{d-\mu} \sim \mu_w \frac{V}{l_m} \pi r_b^2 \quad (4.26)$$

where r_b corresponds to the droplet radius at the immerse liquid. The droplet feature can be used towards formulating the ratio of the droplet radius over the vertical length from the droplet bottom to the droplet center of mass (l_m), i.e. [151]:

$$\frac{r_b}{l_m} = \frac{4 \sin \theta (2 + \cos \theta)}{3 (1 + \cos \theta)^2} \quad (4.27)$$

Furthermore, the dissipation of energy because of shearing between the oil and the droplet having different velocities can be related to [151]

$$E_{d-\tau} \sim \mu \left(\frac{V_d - u_f}{l_m} \right) \pi r_o^2 \quad (4.28)$$

This can be further approximated in terms of the ridge height (l_{rid}) in the sections of the meniscus around the oil ridge and the water droplet [151]. Hence, it yields:

$$E_{d-\tau} \sim \mu_o \left(\frac{V_d - u_f}{l_{ridge}} \right) 2\pi r_o l_{rid} \quad (4.29)$$

$$E_{d-\tau} \sim \mu_o (V_d - u_f) 2\pi r_o \quad (4.30)$$

The force of drag acting on the partially immersed water droplet by the oil can be formulated via Faxen's law [162]; hence, the force of drag becomes

$$F_D \sim 6\pi\mu_o h_{oil} (V_d - u_f) \quad (4.31)$$

where h_{oil} represents the immersion height of the water droplet in oil, which is evaluated from the experiment as $\sim 62 \mu\text{m}$. Moreover, the cap of the water droplet is in the air and the air drag is created, which takes the form

$$F_{D-air} \sim C_d \rho_a A_c V^2 \quad (4.32)$$

where C_d represents drag coefficient $\sim (0.2 - 0.5)$, ρ_a is the air density, A_c being the droplet cap cross-section exposing to air, which is evaluated via the cap height (h_o) and the cap diameter at the rim ($2 \times r_o$). A_c becomes about $2.54 \times 10^{-6} \text{ m}^2$ for $30 \mu\text{L}$ droplet.

Therefore, the change of the water droplet potential energy is partially dissipated by the viscous effects, and the remaining contributes to the droplet kinetic energy change. The overall energy dissipated during immersed water droplet motion along the incremental length scale ΔL in the plane of the oil surface becomes:

$$E_d \sim \Delta L \left(\mu \frac{V}{l_m} \pi r_o^2 + \mu \left(\frac{V - u_f}{l_m} \right) \pi r_o^2 + \mu_o (V - u_f) 2\pi r_o + 6\pi \mu_o h_o (V - u_f) + C_d \rho_a A_c V^2 \right)$$

Simplifying the previous equation results in the following equation:

$$E_d \sim \Delta L \left(\frac{\mu \pi r_o^2}{l_m} (2V - u_f) + \pi \mu_o (V - u_f) (2r_o + 6h_o) + C_d \rho_a A_c V^2 \right) \quad (4.33)$$

The droplet pinning in the immersed oil film due to the interfacial tension of the droplet fluid and oil is in the order of

$$E_T \sim 2\pi \gamma_{w-si} r_o \cos(\theta_c + \alpha) \Delta L \quad (4.34)$$

However, the kinetic energy of the partially immersed droplet at any point on the oil surface is

$$E_k = \frac{1}{2} m_d (V_d - u_f)^2 \quad (4.35)$$

where m_d represents the droplet mass, which is

$$m_d = \rho_w \frac{4\pi}{3} r_{do}^3 \quad (4.36)$$

where r_{do} is the radius of spherical water droplet before immersing in the oil film. The droplet potential energy change within the incremental length scale ΔL in the plane of the oil surface is:

$$E_p \sim \rho_w \frac{4\pi}{3} r_{do}^3 g \Delta L \sin \delta \quad (4.37)$$

where δ being the tilt angle of the oil-impregnated sample. Consequently, using the energy balance within the length scale ΔL , the droplet velocity can be determined. The water droplet (translational) velocity predicted from the energy balance formulation is about 1.45 mm/s while it is about 1.51 mm/s from the experiments for 30 μ L droplet after 48 mm transition along with the oil film with 4° inclination angle. Hence, the velocity of droplets resulting from the energy balance agrees with the experimental high-speed data obtained using the tracker program. The ratio of the dissipated energy because of

shearing influence over the droplet potential energy variation is about 4%. In addition, the ratio of dissipated energy due to the droplet pinning, which is created by interfacial surface tension, over the change of the droplet potential energy is about 7%. Hence, the energy dissipated because the interfacial tension becomes higher than that of the viscous effects. Nevertheless, the overall water droplet energy loss is almost 11% as the droplet slides over the oil-impregnated crystallized polycarbonate surface.

CHAPTER 5

RESULTS AND DISCUSSION

5.1 Silicone Oil Impregnation

Sliding water droplet on silicone oil-infused crystallized polycarbonate is examined and the flow characteristics in the silicone oil and the droplet are analyzed. The experimental tests are conducted and water droplet mobility on the impregnated surface is recorded using the high-speed monitoring system and droplet velocity is analyzed utilizing the tracker program. The numerical simulations of flow are also carried out by adopting the experimental conditions.

5.1.1 Silicone Oil Impregnation of Crystallized PC Surface

The solution crystallization method is used to texture the polycarbonate wafer surfaces. Figure 24.a and Figure 24.b show SEM micro image of the crystallized polycarbonate surface and Figure 24.c and Figure 24.d depict the AFM micro-image and line scan of the crystallized surface. The crystallized surface has a topology with spherules and fibrils which is illustrated in Figure 24.a. The creation of spherules is because of the growth of crystals radially at the nucleation sites on the surface. The initiation of the nucleation site occurs via diffusion of acetone in the nanopores sites on the polycarbonate surface. It is worth noting that the polycarbonate wafer surface has a nano-porous-like texture [155], [156] while the Hildebrand solubility parameter of acetone is in the range of 20.1 - 20.3

$J^{1/2} \text{cm}^{-3/2}$ [157] and has the miscible feature. Acetone diffusion causes a swollen layer at the polycarbonate surface and the transition glass temperature of polycarbonate in the neighborhood of the diffusion becomes small. This results in the plasticizing of swollen film material on the surface [157]. The acetone diffusion is governed by none-Fickian nature and the acetone diffusion occurring into the plasticized film takes place at a constant speed towards the amorphous polycarbonate solid [158], [155].

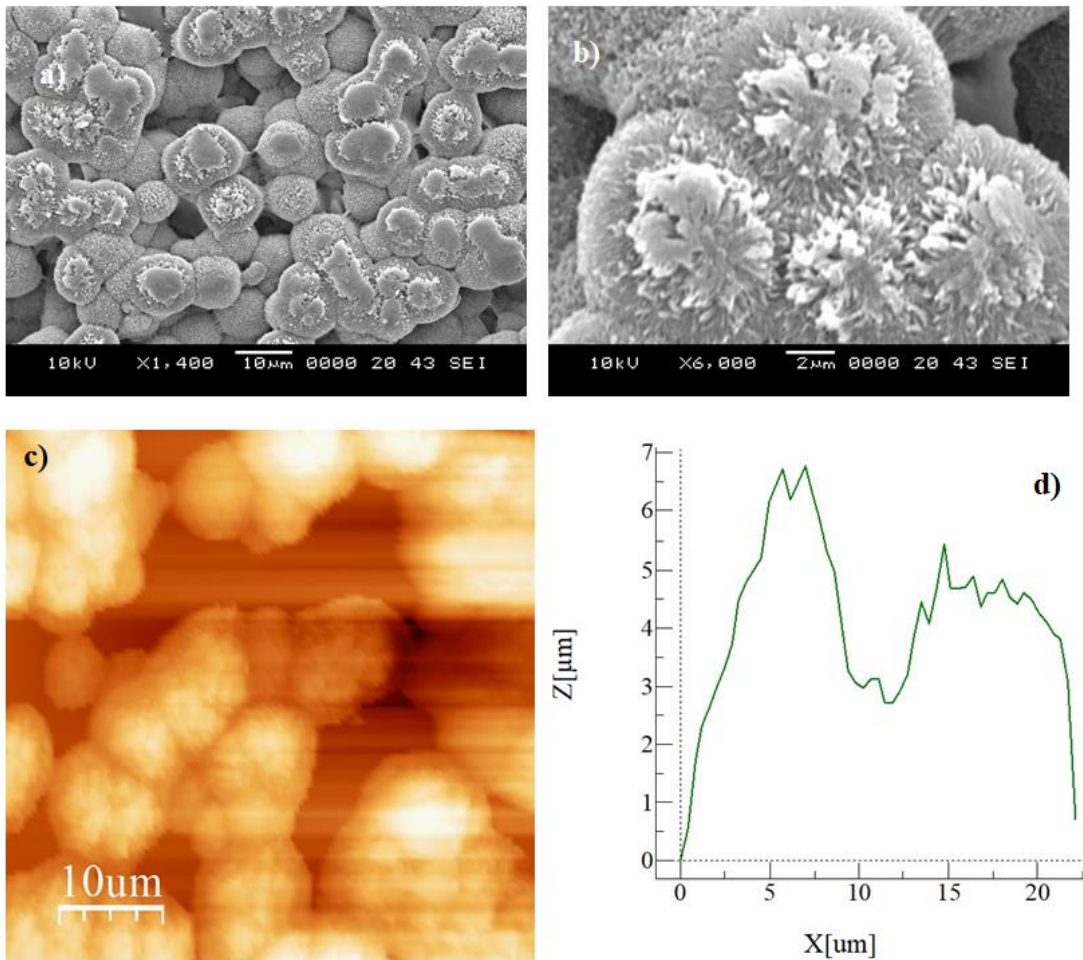


Figure 24 Scanning electron microscopy (SEM) and atomic force microscope (AFM) images and line scan of the crystallized polycarbonate surface: a) SEM image of various sizes of spherules, b) SEM image of fibrils and spherules, c) AFM image of the surface, and c) AFM line scan over the surface

Moreover, initiation sites for crystallization on the polycarbonate surface demonstrate branching during the radial growth. Some branches result in excessive crystal growing

while developing big spherules on the polycarbonate surface, which is mostly true as the duration of diffusion extends [155], [156]. It is worth noting that crystallization takes place via the processes of initial nucleation, prime construction, and second phase growing [163]. The nucleus for the initiation of the crystallization occurs as the polymer chains align in a parallel way and the growth of crystals starts spontaneously as the nucleus approaches the critical size [163] while developing bundle-like and lamellar structures in the crystallization sites [164]. Once the setting time for acetone diffusion is over, the crystallized samples are taken out of the crystallization container. The sample surfaces have almost hierarchical distributed spherules and fibrils appear over the surface. This can also be seen in the AFM line scan which is shown in Figure 24.d. The fibrils, which have whiskers like textures on the spherules surface, can create sites reducing the droplet contact surface of the spherules while increasing droplet motion. However, the area covered by the fibrils is small on the spherules surface which is illustrated in Figure 24.b and their contribution to droplet mobility become small. The average roughness of the surface is about $4.62 \mu\text{m}$. The contact angle which was measured to be $132^\circ \pm 4^\circ$ has resulted in hysteresis of $38^\circ \pm 5^\circ$. Hence, the crystallized sample surface possesses a hydrophobic state. Since the contact angle hysteresis is considerably large, droplet pins on the inclined surface. The crystallized surfaces are impregnated with silicone oil. The use of silicone oil provides water droplet sliding on the oil surface without undergoing resistance unlike the non-oil impregnated crystallized surface and improves the optical transmittance of the crystallized sample. On the other hand, the state of oil impregnation on the crystallized surface can be described via one of the followings: i) oil can partially wet the crystallized surface and some unwetted (dried) regions can occur on the wafer

surface, or ii) oil wets the surface and oil impregnation does not encapsulate the surface, or iii) oil wets the surface while the crystallized surface is encapsulated by the oil. The surface encapsulation results in total coverage of fibrils and spherulites on the crystallized surface by the oil. The stages of liquid impregnation of surfaces depending on the surface properties, such as roughness parameter, and interfacial shear between the liquid and the solid surface [155], i.e.:

$$\frac{(\gamma_s - \gamma_{o-s})}{\gamma_o} = f\left(\frac{(1-\varphi)}{(r-\varphi)}\right) \quad (5.1)$$

where f demonstrates the functional relation, φ represents the fraction of the projected area of the surface as occupied by solid and r being the roughness parameter and it resembles the fraction of spherules area to the projected area on the oil-solid surface. In addition, γ_s is solid surface free energy, γ_{o-s} is interfacial tension of oil-solid, and γ_o is oil surface tension. To determine the interfacial energy between the solid and oil, the Hemi-Wicking condition can be introduced [155], [158], [163], [165], i.e. the contact angle at the interface is related via Young's equation as,

$$\cos\theta_{s-o} = \frac{r(\gamma_s - \gamma_{s-o})}{\gamma_o} \quad (5.2)$$

The fraction of solid projection area is obtained from the AFM microimage of the surface which is shown in Figure 24.c and it yields about $\varphi = 0.32$. It is also shown that for oil impregnation of the surface, the following conditions should be met:

$$\theta_{s-o} < \cos^{-1}\left(\frac{1}{r}\right) \text{ and } S_{s-o} \geq 0 \quad (5.3)$$

where S_{s-o} is the spreading rate of silicone oil on the crystallized surface [151]. The oil spreading rate over the surface is determined as $S_{os(a)} = 13.5 \text{ mN/m}$, which demonstrates the spreading of silicone oil on the crystallized sample. The oil-free energy on the sample

surface is evaluated adopting the contact angle technique [166], [167], which results in about 18.8 mN/m. Hence, silicone oil encapsulates the crystallized surface. In addition, oil impregnation experiments also demonstrate that silicone oil completely encapsulates the textured (crystallized) polycarbonate surface. The thickness of the impregnated oil is evaluated via an ellipsometer (M-2000 J.A. Woolam Co.). The thickness of the oil is in the order of $0.7 \mu\text{m} \pm 0.01 \mu\text{m}$. The optical transmittance of the crystallized surface and the oil-impregnated surface is evaluated using a UV visible spectrometer (Jenway 67 series).

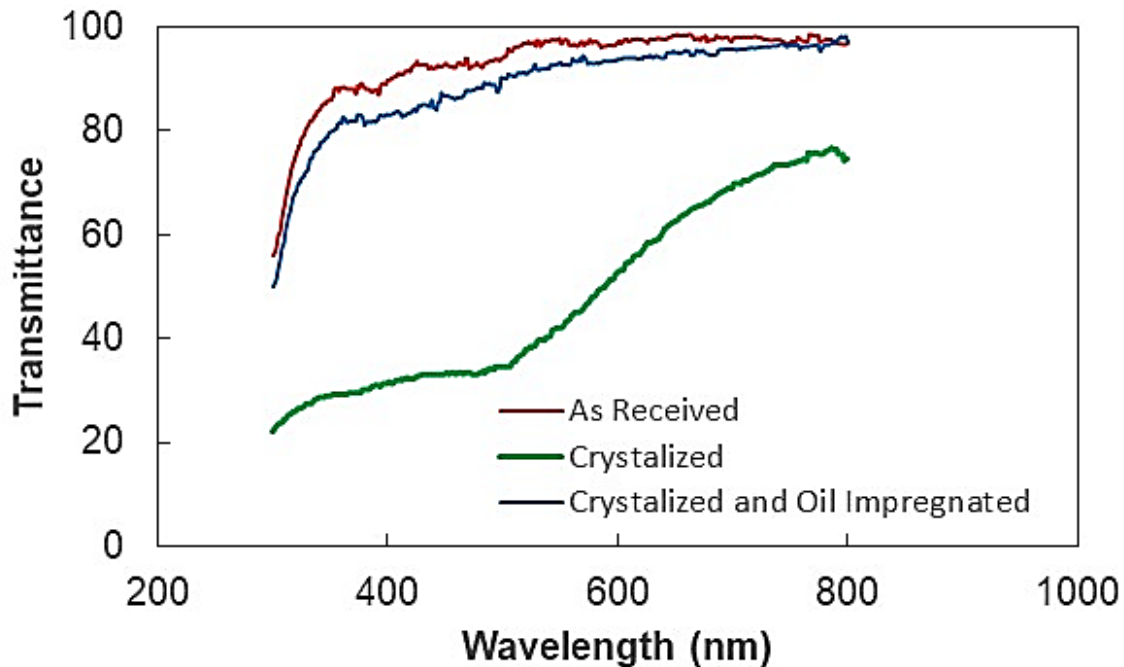


Figure 25 Optical transmittance of polycarbonate, crystallized polycarbonate, and silicone oil-impregnated crystallized polycarbonate samples

Figure 25 shows the optical transmittance of the crystallized polycarbonate sample before and after oil impregnation. In addition, the optical transmittance of as received polycarbonate surface is also provided in Figure 25 for comparison. Optical transmittance of the crystallized sample becomes considerably less than that of the as-received

polycarbonate, which may be because of diffusion and scattering of the incoming optical radiation by the surface texture, such as by the spherules and fibrils. However, oil impregnation recovers notably optical transmittance of the crystallized samples.

As the water droplet is formed on the oil, it is partially immersed and floats on the oil layer. Around the water droplet interface (air-oil-water contact line) oil infusion takes place because of oil spreading over the water droplet. Oil infusion can be seen in Figure 26, where the optical image of the partially immersed water droplet and oil rim is shown. In order to initiate oil infusion, the spreading coefficient (S_{o-w}) of oil must remain greater than zero. The spreading coefficient is:

$$S_{o-w} = \gamma - \gamma_{w-o} - \gamma_o \quad (5.4)$$

where γ is the surface tension of water, γ_{w-o} is the oil and water interfacial tension, and γ_o is the surface tension of oil. The interfacial tension between silicone oil and water is 42.15 mJ/m^2 [168] and the surface tension of water and silicone oil is 72 mN/m and, 18.85 mN/m , respectively [169].

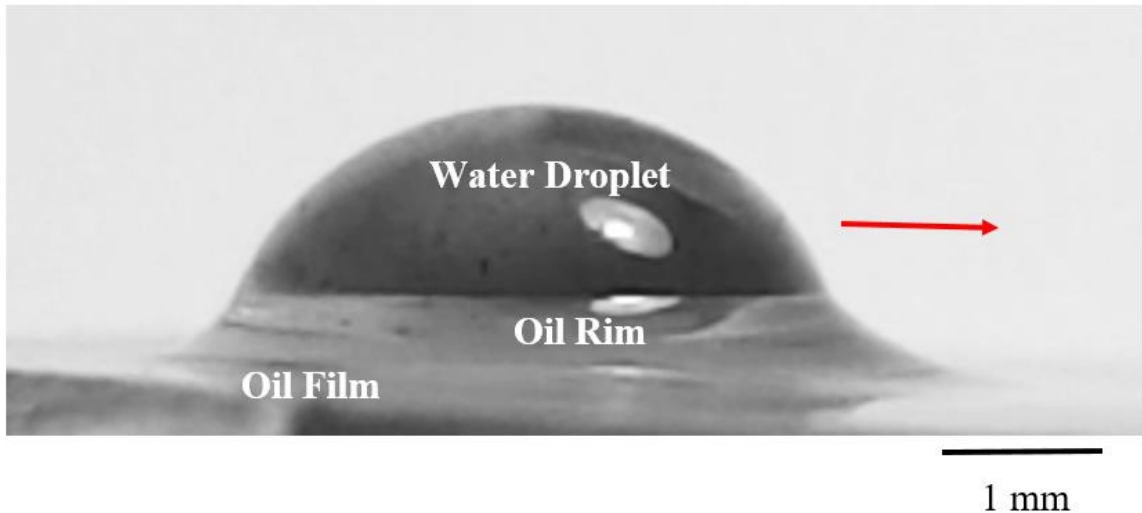


Figure 26 Optical image of sliding water droplet and silicone film. Red shows the sliding direction of the water droplet. The inclination angle of the sample is 40° , droplet volume is $30 \mu\text{L}$, and the location of the droplet is 25 mm away from sliding initiation on an oil film

Inserting the values results in the spreading coefficient (S_{o-w}) of 11 mN/m, which is positive; hence, silicone oil infuses over the surface of the droplet. During the silicone oil infusion, an oil ridge is formed around the rim of the water droplet (Figure 26) because of the vertical pulling force created by the tension at the oil-water interface.

5.1.2 Numerical Findings

Figure 27 shows the variation of droplet (translational) velocity with the distance on the oil film, which is inclined at 4° , for different droplet volumes. It is worth mentioning that the droplet velocity represents the relative velocity reference to the oil film velocity, which is about 0.016 mm/s. Increasing the length scale on the oil film enhances the droplet velocity, which becomes more apparent for 30 μL droplet. Increasing droplet velocity with enlarging distance on the oil is associated with the balance of the gravitation, drag, and adhesion forces. The losses related to oil and air drag of the partially immersed water droplet reduce as the droplet volume reduces; however, the force due to gravity increases with increasing droplet volume. Hence, reducing droplet volume causes a low force of gravity and sliding the water droplet. However, the increase (rise) of the droplet velocity along the oil becomes high for small volume droplets, i.e. 30 μL . Moreover, Figure 28 shows that the experimentally predicted droplet translational velocity compares well to that of the simulation. This is because the model was calibrated utilizing the experimental data on the droplet geometric and sliding characteristics. Nevertheless, the simulation becomes useful in predicting the flow field within the droplet and oil layer.

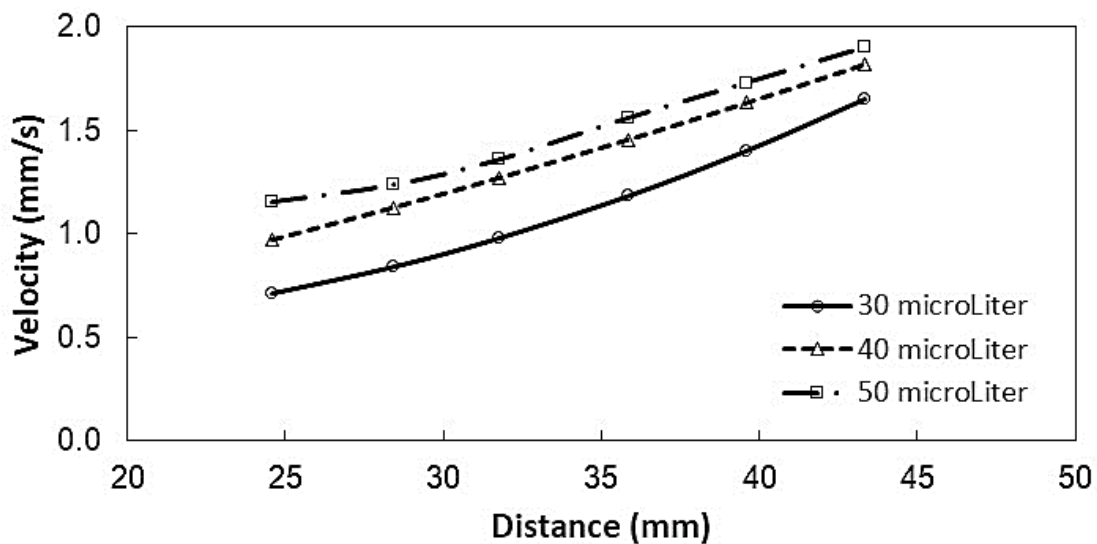


Figure 27 Droplet velocity on impregnated oil film for different droplet volumes. The distance of zero represents the droplet start of sliding on the silicone oil film

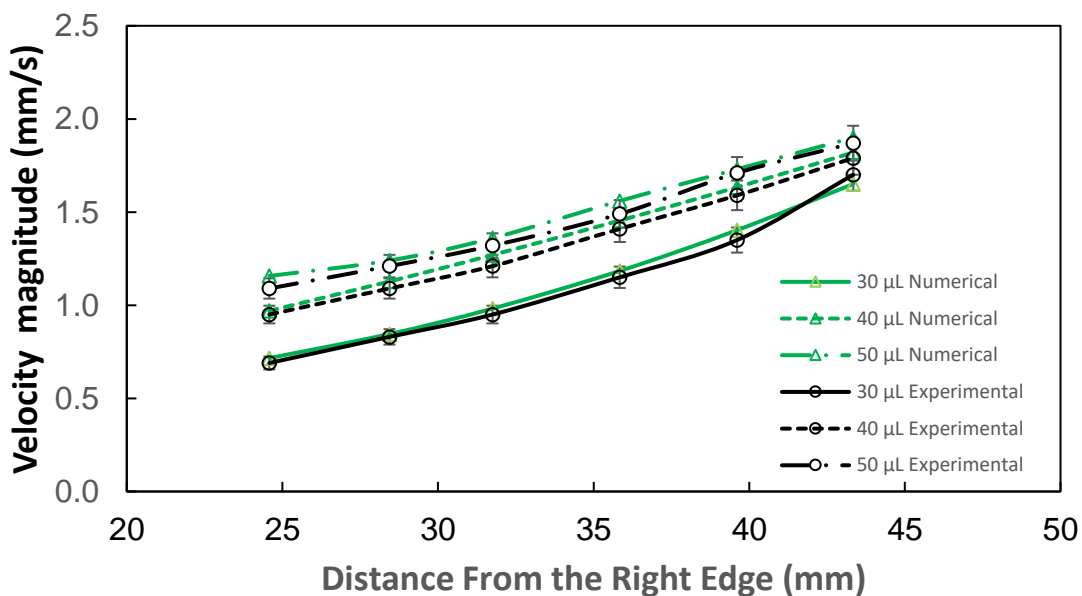


Figure 28 Comparison of droplet translational velocity as obtained from both experiment and simulations. The distance of zero represents the droplet start of sliding on the silicone oil film

Although the ratio of the sum of drag and pinning forces is almost 11% of the potential energy change of the droplet over the oil film, increasing droplet volume increases the sum of drag and pinning forces acting on the sliding water droplet due to a substantial increase of the droplet rim diameter on the oil film. This is observed from Figure 29, in which the variation of droplet rim diameter is shown with distance on the oil film. In this case, increasing droplet volume from 30 μL to 50 μL , the rim diameter increases by almost 30%. Hence, increasing rim size enhances the pinning and drag forces, which modifies the droplet velocity along with the distance on the oil surface. This becomes more apparent for large volumes. It is worth noting that 30 μL water droplet velocity increases almost three times at the end of the sliding length (44 mm); however, the velocity increase becomes almost 1.5 times for 50 μL droplet. In the case of Figure 30, the oil ridge height increases as the droplet volume increases. The ridge height in the frontal region of the droplet becomes larger than that of the back region of the droplet. Moreover, the oil ridge formation along the droplet circumference remains important in terms of the adhesion (pinning force) which can be found using Eq. 4.39 [152]. The ridge height around the oil rim changes because of the oil build-up in the front region of the water droplet as the droplet transition continues on the inclined oil film. This can be observed from Figure 30, in which the ridge heights at the droplet frontal (right ridge) and droplet back (left ridge) are shown for three volumes. Enlarging distance within the oil film results in increased ridge height at the droplet frontal region while ridge height at the droplet back reduces. However, the change in ridge heights is not significantly considerable within the inclined oil surface for 30 μL droplet. As the droplet volume increases, the difference between the frontal and back ridge heights becomes large. This

demonstrates that as the larger volume water droplet slides over the oil film, the ridge height at the droplet back region decreases more than the ridge height increase at the droplet frontal region. This creates varying shear resistance in the air and oil sides simultaneously as the droplet slides over the oil film.

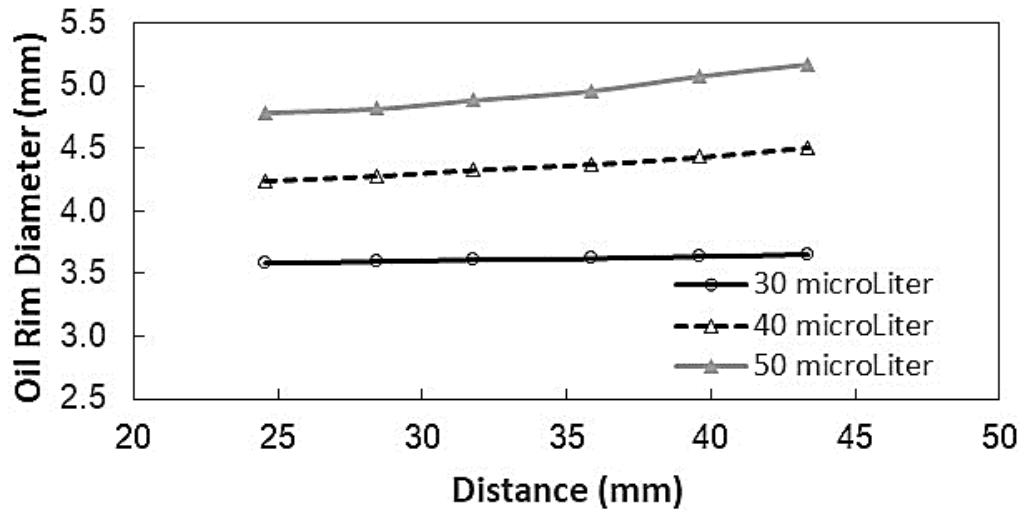


Figure 29 Droplet rim diameter (diameter on oil film) for different droplet volumes. The distance of zero represents the droplet start of sliding on the silicone oil film

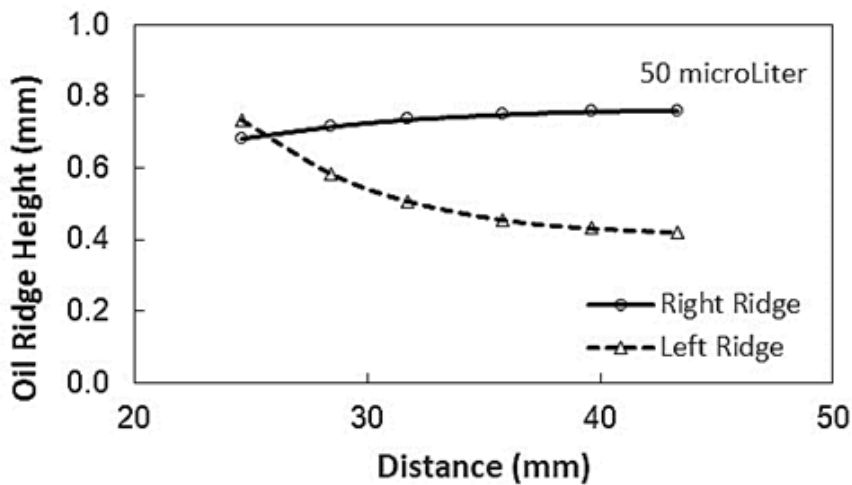
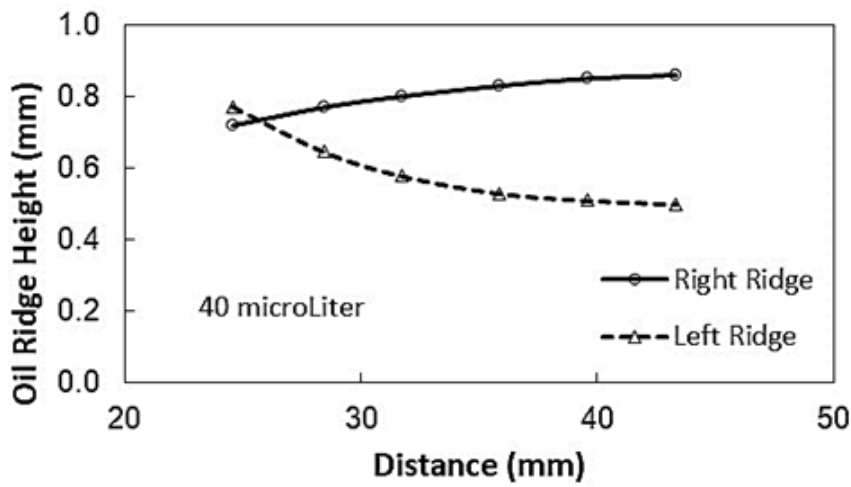
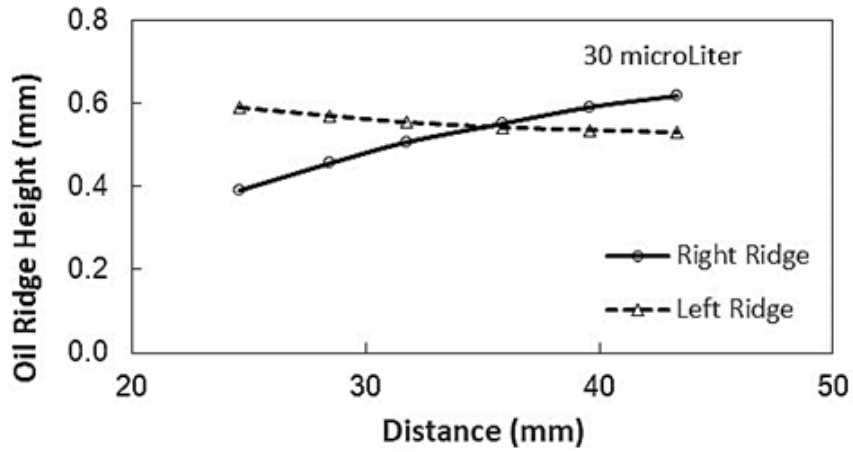
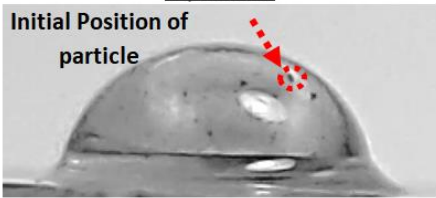
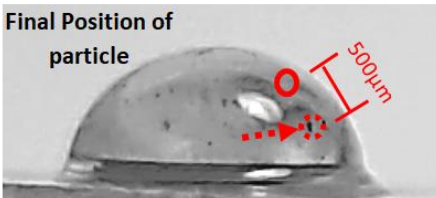
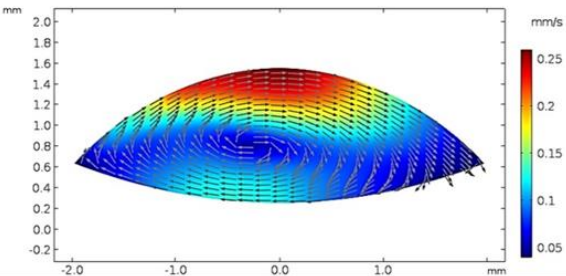


Figure 30 Oil film ridge height in the front side (right ridge) and backside (left ridge) of water droplet for different droplet volumes

In order to evaluate the flow created inside the water droplet during sliding over the oil film, a 3-dimensional simulation of the water droplet behavior in the oil is considered incorporating the experimental conditions Figure 31 show a 3-dimensional view of the droplet on the film. To compare the simulated and experimental flow field, separate experiments were conducted with droplets containing Si nanotubes with the high-speed recording system. The particle's motion was tracked and the velocity field estimated shows a closer comparison with that of the simulations (shown in Table 4).

Table 4 Comparison of velocity field obtained from experiments and simulations for 40 μ L and droplet location of 32 mm from the edge.

Particle #	X (mm)	Y (mm)	Experimental V (mm/s)	Simulation V (mm/s)	
1	0.936	0.679	0.121	0.102	<p style="text-align: center;"><u>Experiment</u></p>  <p style="text-align: center;"><u>Final Position of particle</u></p>  <p style="text-align: center;"><u>Simulations</u></p> 
2	1.409	0.735	0.820	0.861	
3	1.503	0.838	0.915	0.908	
4	1.033	0.870	0.135	0.123	
5	1.225	1.104	0.131	0.142	
6	0.727	1.2	0.297	0.23	
7	-0.50	1.19	0.154	0.147	
8	-1.30	1.120	0.141	0.128	
9	0.130	1.353	0.258	0.25	
10	0.986	1.432	0.240	0.230	

To analyze the flow field in the film and inside the droplet, separate flow images resembling the flow field inside the droplet fluid and film are presented in Figure 32,

Figure 33, and Figure 34. The flow circulations are observed at the cross-section of the droplet at different locations in these figures.

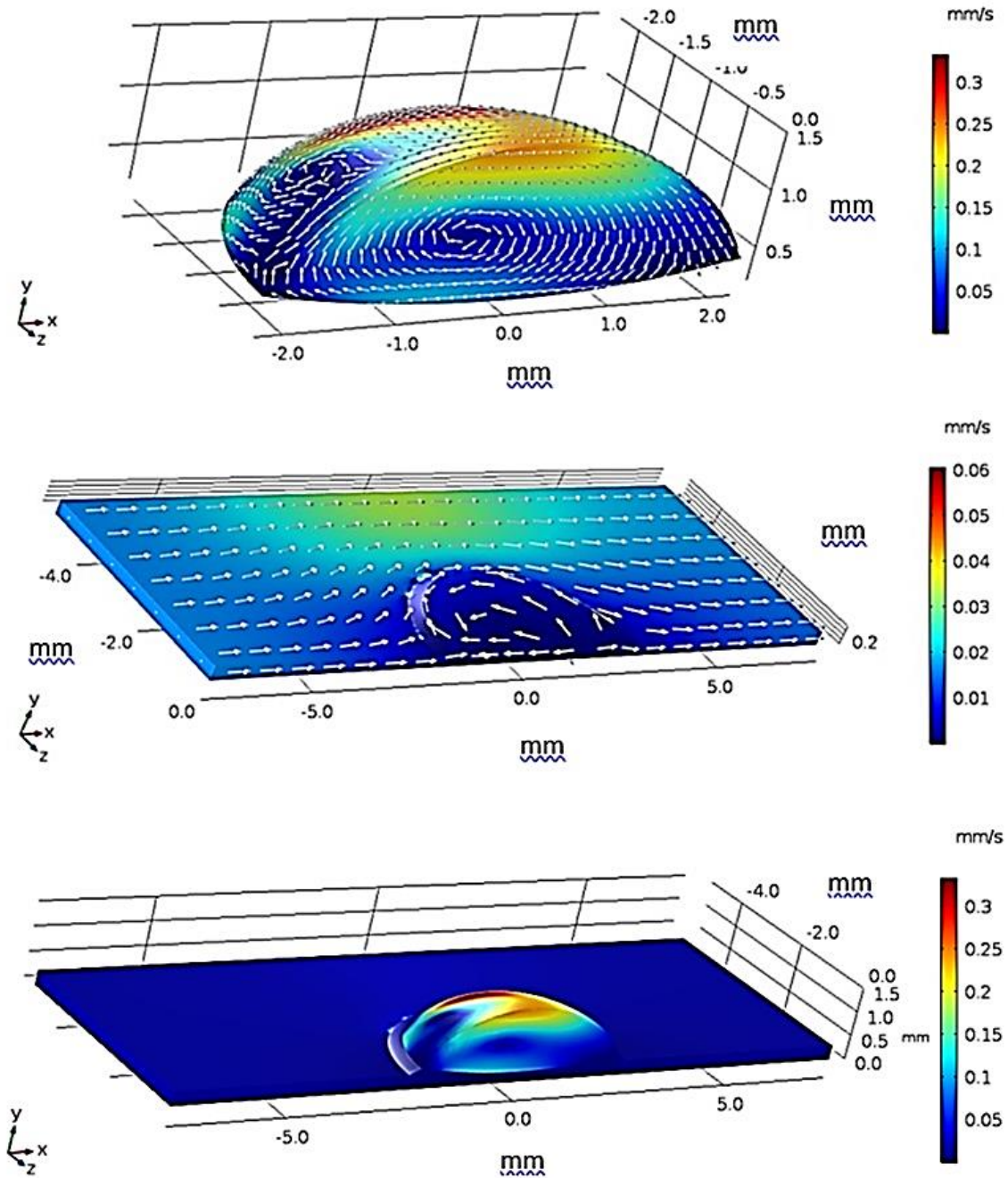


Figure 31 3-dimensional simulation of water droplet velocity on oil film: a) velocity in droplet and film, b) velocity in oil film and c) velocity in the water droplet. Since the maximum velocity magnitude in oil film and droplet are different, they are shown separately to observe flow velocities

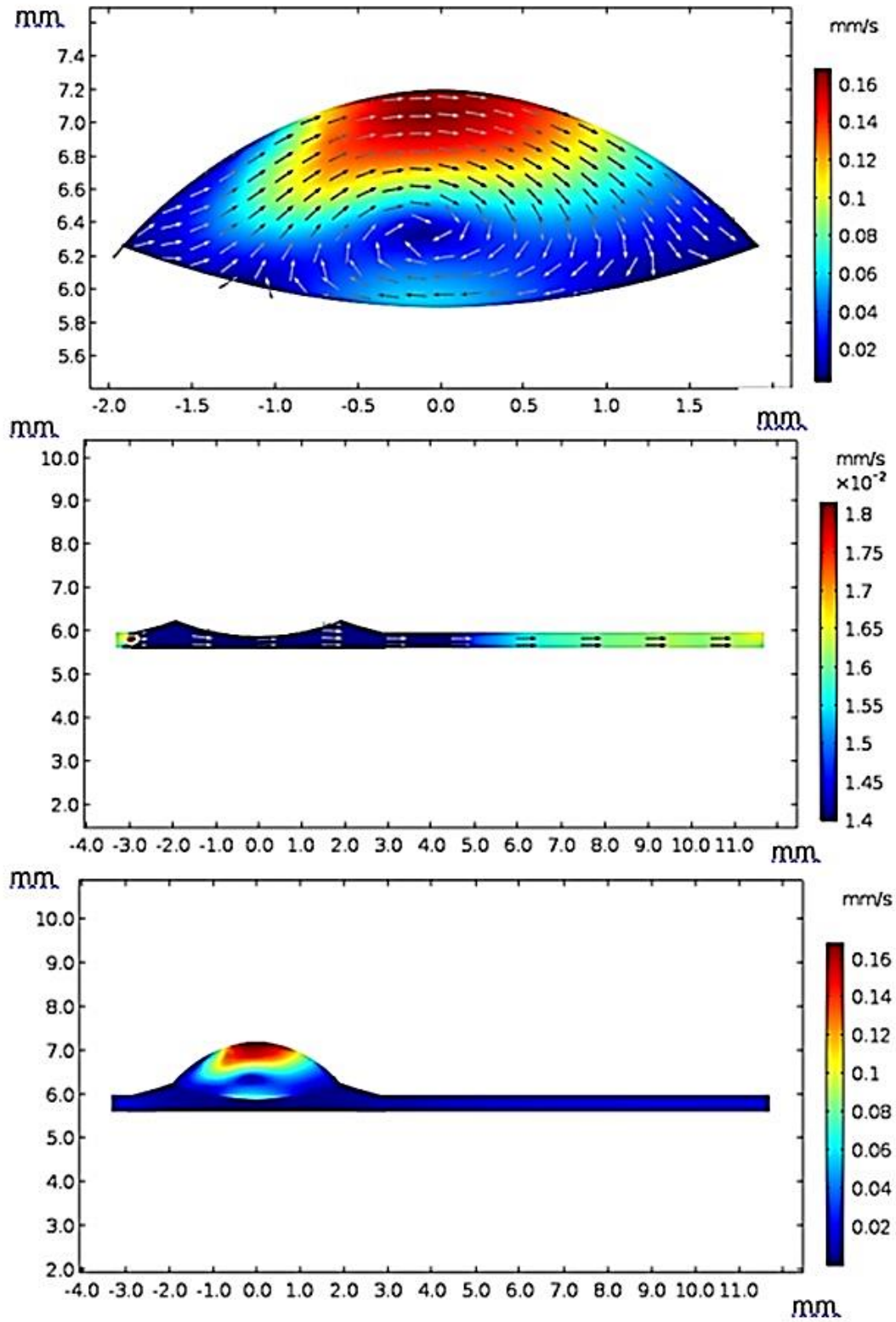


Figure 32 Velocity magnitude over the symmetry plane in water droplet and oil film. The inclination angle of the sample is 40° , the droplet volume is $40 \mu\text{L}$, and the droplet location is at the droplet initial sliding site (i.e. 24 mm from the edge). Since the maximum velocity magnitude in oil film and droplet are different, they are shown separately to observe flow velocities. Simulations are carried out in one solution domain

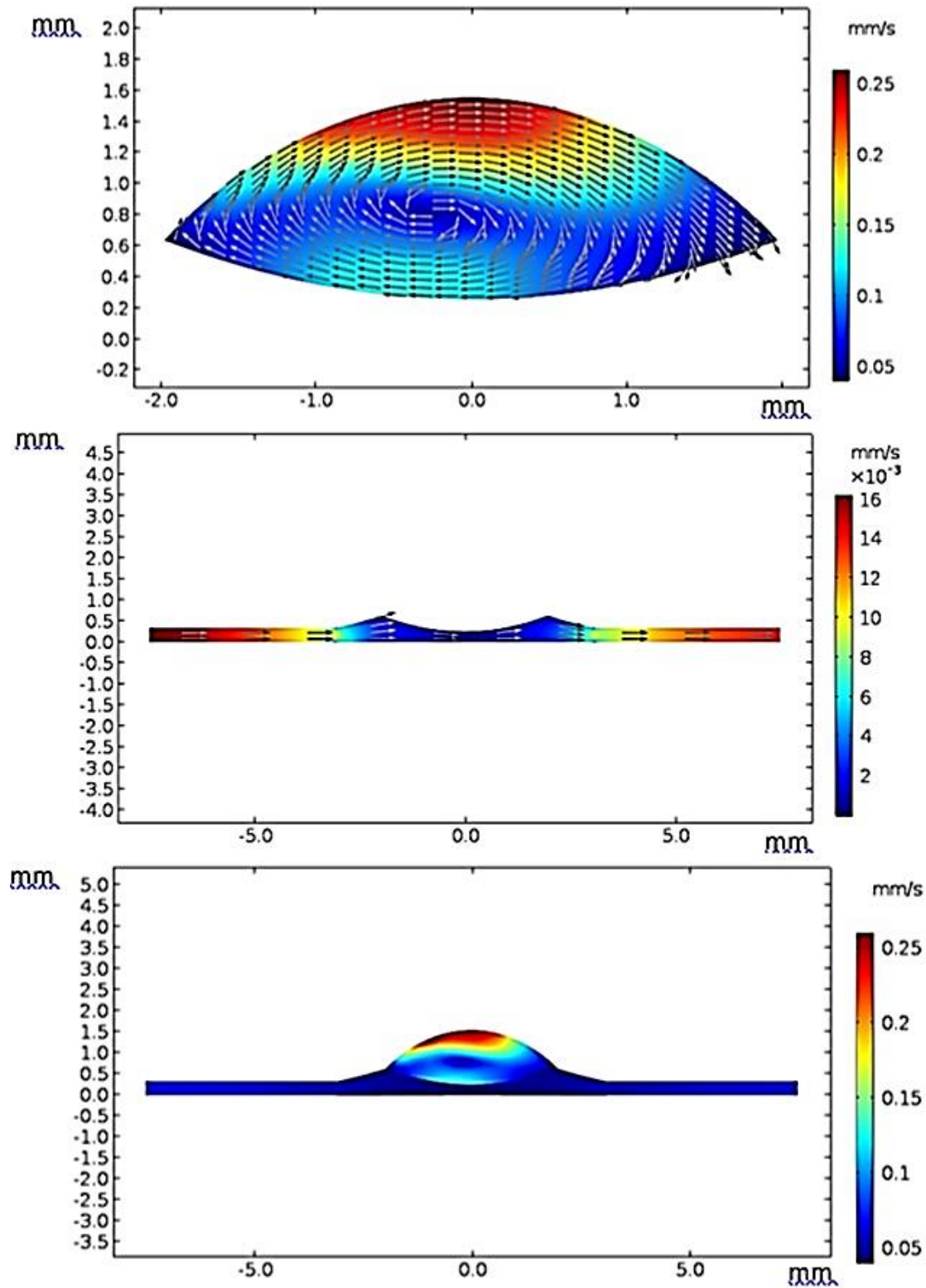


Figure 33 Velocity magnitude over the symmetry plane in the water droplet and oil film. The inclination angle of the sample is 40° , the droplet volume is $40 \mu\text{L}$, and the droplet location is 8 mm from the droplet initial sliding site (i.e. 32 mm from the edge). Since the maximum velocity magnitude in oil film and droplet are different, they are shown separately to observe flow velocities. Simulations are carried out in one solution domain

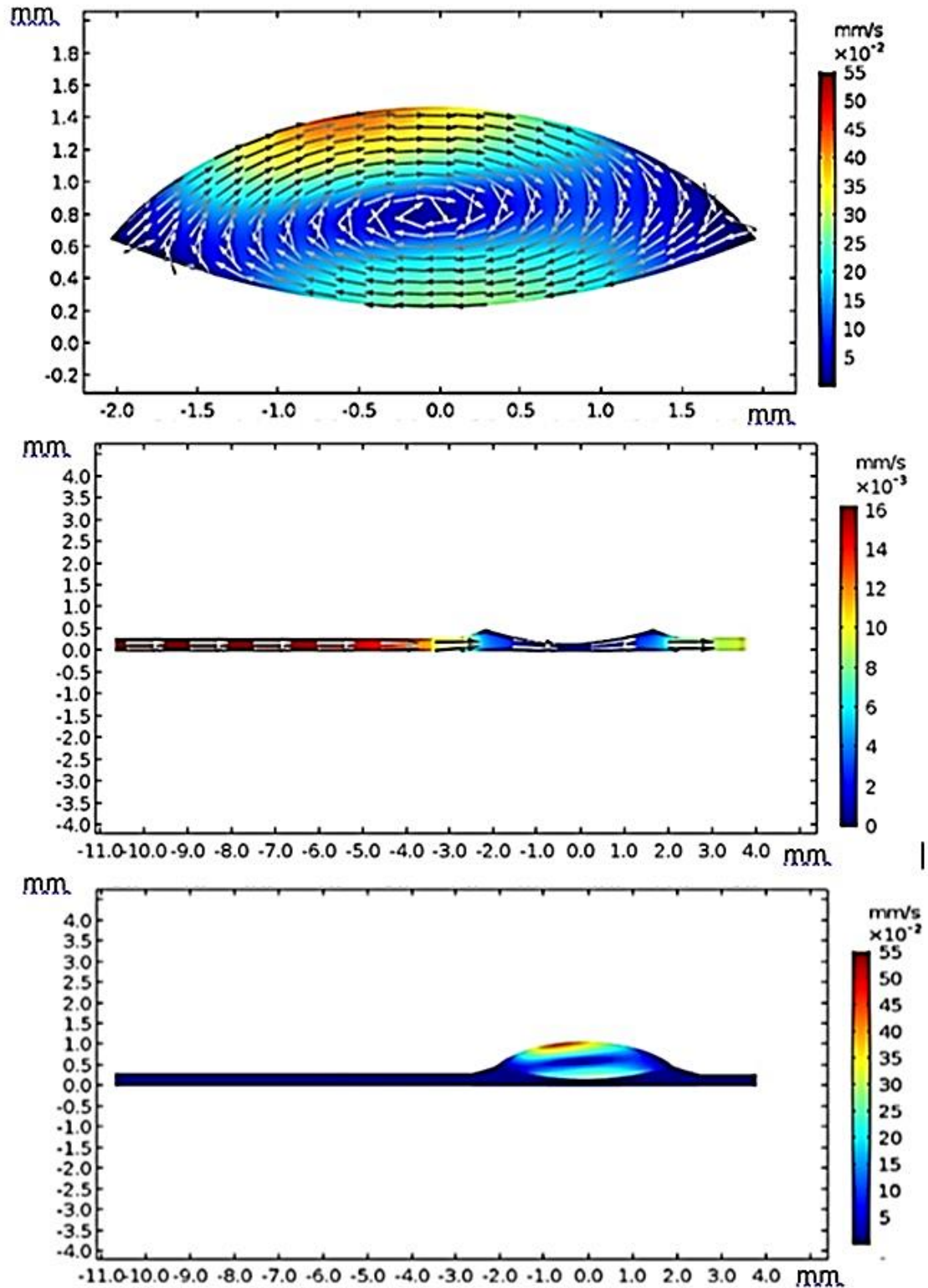


Figure 34 Velocity magnitude over the symmetry plane in the water droplet and oil film. The inclination angle of the sample is 40° , the droplet volume is $40 \mu\text{L}$, and the droplet location is 16 mm from the droplet initial sliding site (i.e. 40 mm from the edge). Since the maximum velocity magnitude in oil film and droplet are different, they are shown separately to observe flow velocities. Simulations are carried out in one solution domain

The Marangoni and buoyancy influences on the flow inside the droplet are considered to be minimum because of almost isothermal flow being created inside the droplet. Here, it is worth mentioning that during the droplet motion, energy dissipated due to the interfacial shear generated in air, and oil contributes to the heat generation inside the droplet and oil. However, this contribution does not yield a notable temperature increase in the oil and the water droplet. Consequently, the flow generated in the oil film and the droplet is related to the shearing rate formed around the droplet in the film and the air. In this case, air drag over the droplet cap and interfacial friction around the oil rim and inside the oil (because of partial immersion of the droplet) create flow fields, which change along the length of the oil film. The inclination of the oil film on the sample surface creates a flow field in the oil film and yet gravitation influence on the droplet creates similar flow behavior inside the droplet having a different velocity than the oil film. The interfacial flow resistance alters locally the rate of fluid stain within the oil film and the droplet fluid. This creates a complicated flow structure involving fluid rotation. Moreover, varying size of the oil rim around the droplet contributes to the local shearing effect on the flow as the droplet and oil film moves on the sample surface. Since the droplet velocity is larger than the oil film velocity, the droplet motion disturbs the oil film flow. The flow created inside the droplet fluid and disturbance of oil film flow by the sliding droplet creates a circulatory flow in the film below the droplet, which can be seen from Figure 31.b. Moreover, to demonstrate the effect of viscous shearing on the flow field, the flow within the cross-section of the droplet and the oil film is shown in Figure 32, Figure 33, and Figure 34 at three different locations on the film for 40 μ L droplet. The circulatory flow is developed in the droplet having a large velocity in the region of

the droplet cap. The center of the circulation occurs away from the centroid of the droplet for the case when the droplet is in the initial sliding location on the oil film ($s = 0$, s being the distance within the oil surface) as observed from Figure 32. The formation of circulation occurs because of the interfacial shear between the oil and the droplet at the droplet-oil contacted regions. In addition, the droplet motion disturbs the air around the droplet cap while causing the interfacial shear resistance over the droplet free boundary, which enriches the shear strain in the upper section of the droplet cap because of the high droplet velocity. This generates varying shear rates along with the droplet cap, particularly in the region of the cup tip. This also contributes to the formation of flow inside the droplet fluid. As the droplet moves further on the oil film, the structure of the circulating flow changes slightly (Figure 33) and as the droplet slides further along the oil film, the flow structure is further modified (Figure 34). The peak velocity in the droplet fluid increases as the droplet slides over the oil. In this case, the mismatch between the oil velocity and droplet velocity increases resulting in increased shear rates in the immersed part of the water droplet. Similarly, the interfacial shear rate also increases around the cap region of the droplet because of the increased droplet velocity while enhancing the frictional drag.

5.2 Mitigation of Dust Particles

Sliding water droplet on silicone oil-infused crystallized polycarbonate is examined and the flow characteristics in the silicone oil and the droplet are analyzed. The surface characteristics of the crystallized PC surface and the properties of the dust particle are investigated. The cloaking procedure of the water droplet, oil film, and dust particles are examined. The effect of oil film thickness on the cloaking of the water droplet and the dust removal mechanism is explored. The experimental tests are conducted and water droplet mobility on the impregnated surface is recorded using the high-speed monitoring system and droplet velocity is analyzed utilizing the tracker program.

5.2.1 Crystallized Polycarbonate Surface and Dust Properties

The solution treatment (30% concentration acetone) is used to crystallize polycarbonate surfaces via immersing technique. Figure 35.a and Figure 35.b show top views of crystallized surfaces. The crystallized surface has a texture, which consists of globules (Figure 35.a) and fibers like whiskers (Figure 35.b) emanating from the surface of the globules. The formation of whiskers is related to the secondary branching from the initially formed crystal sites [170]. The whiskers act like nano-pins over the textured surface and contribute to the mobility of the liquid droplet, i.e. it creates a Lotus effect on the surface. The size of the globules varies on the textured surface; however, they create a hierarchical texture morphology. Figure 36.a and Figure 36.b show the surface image (Figure 36.a) and texture profile (Figure 36.b) of the crystallized surface obtained from an atomic force microscope. The globules on the surface are apparent from the profile peaks. The average roughness of the surface is 3.2 μm and the surface roughness

parameter (ratio of area covered by globulus over the projected area) is about 0.56. The wetting state of the surface prior to and after the crystallization is evaluated using a Goniometer) via measuring contact angle and hysteresis. The contact angle of water is measured as $132^\circ \pm 4^\circ$ on the crystallized surface while the hysteresis is $38^\circ \pm 5^\circ$. Hence, the crystallized surface demonstrates hydrophobic behavior; however, the droplet adheres to the surface due to high hysteresis. To evaluate the opaqueness of the textured samples, optical transmittance measurement is carried out. Figure 37 shows optical transmittance of the textured and as received polycarbonate surfaces. The transmittance of the crystallized sample reduces significantly because of the texture; in which case, incident electromagnetic radiation diffuses and scatters at the crystallized surface. In this case, spherules and fibrils on the crystallized surface cause diffuse reflection and partial absorption of incident UV visible radiation while resulting in scattering of incident radiation and lowering specular transmittance (wavelength-dependent transmittance). The increasing wavelength of incident optical radiation lowers diffuse reflection and absorption from the crystallized surface. In order to enhance optical transmittance, the surface is impregnated with silicone oil. To cover the surface with a complete oil film, spreading factor of silicone oil on crystallized polycarbonate surface (S_{o-pc}) becomes important. The oil spreading is related to the surface tension of oil (γ_o), interfacial-shear at the oil-crystallized surface interface (γ_{pc-o}), and surface free energy of crystallized surface (γ_{pc}). This yields [171], [172]:

$$S_{o-pc} = \gamma_{pc} - \gamma_{pc-o} - \gamma_o \quad (5.5)$$

The surface free energy of the crystallized sample is evaluated by Yilbas et al., which is $\gamma_{pc} \cong 36.2 \text{ mJ/m}^2$ [173] and the surface tension of silicone oil is $\gamma_o \cong 0.0187 \text{ N/m}$

[174]. The interfacial tension between oil and the crystallized surface can be evaluated through the Hemi-Wicking condition [175], i.e. it becomes:

$$\gamma_{pc-o} = \gamma_s - \frac{\gamma_o \cos \theta_{pc-o}}{r} \quad (5.6)$$

where $\cos \theta_{pc-o}$ is the droplet contact angle on the crystallized sample. The interfacial tension (γ_{pc-o}) is estimated as 4.3 mN/m. Hence, the spreading factor (S_{o-pc}) for silicone oil on the crystallized surface becomes 13.2 mN/m, which is greater than zero. This demonstrates that silicone oil spreads over the crystallized surface. Hence, the silicone oil is spread over the crystallized surface under the controlled laboratory environment and, later, the oil film thickness is evaluated. Two extreme film thicknesses, 50 μm and 700 μm , are considered in the experiments. It is worth mentioning that as the oil film thickness reduces beyond 50 μm on the crystallized surface, the continuation of the oil film is not observed; rather, oil forms islands like wet regions on the surface than developing a continuous film.

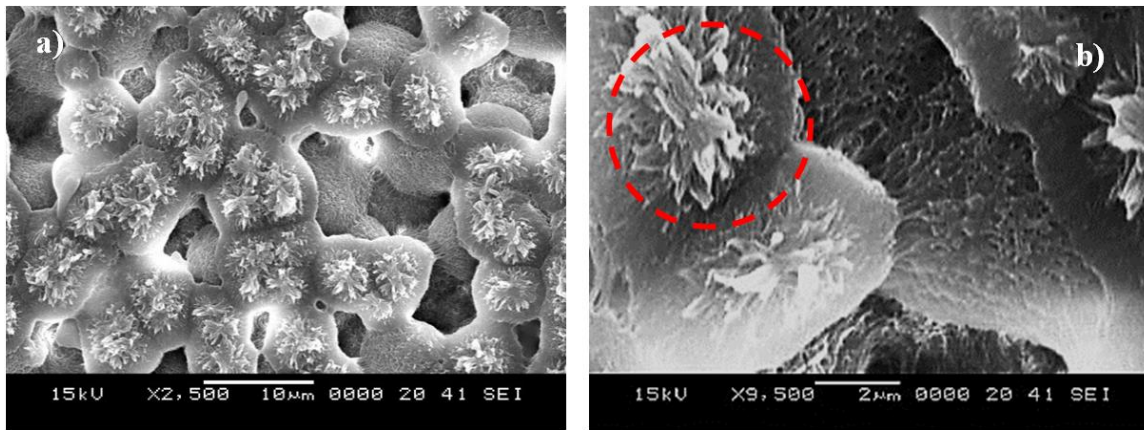


Figure 35 SEM images of crystallized surface: a) micro size spherules, which represent the crystallized structures. Increasing acetone concentration or immersion duration, micro-size spherules become congested while lowering surface contact angle considerably and b) fibrils on spherules (in the red dotted circle). Fibrils are formed from the crystallized sites and they create the Lotus effect reducing contact angle hysteresis

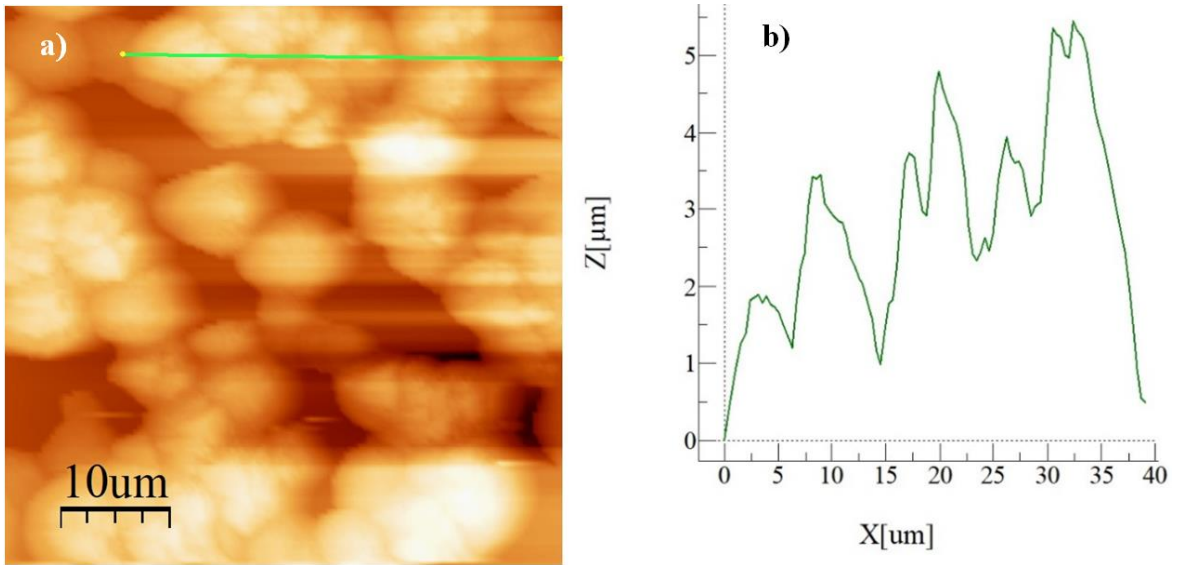


Figure 36 AFM surface image and line scan: a) micro-image of the surface. The small bright spots represent the spherules and brightness is related to the height of the spherules (brighter the spot corresponds to higher the spherules), and b) line scan, which is taken over the crystallized surface. It is shown as a green line in Figure 36a. It provides information on the height of the spherules

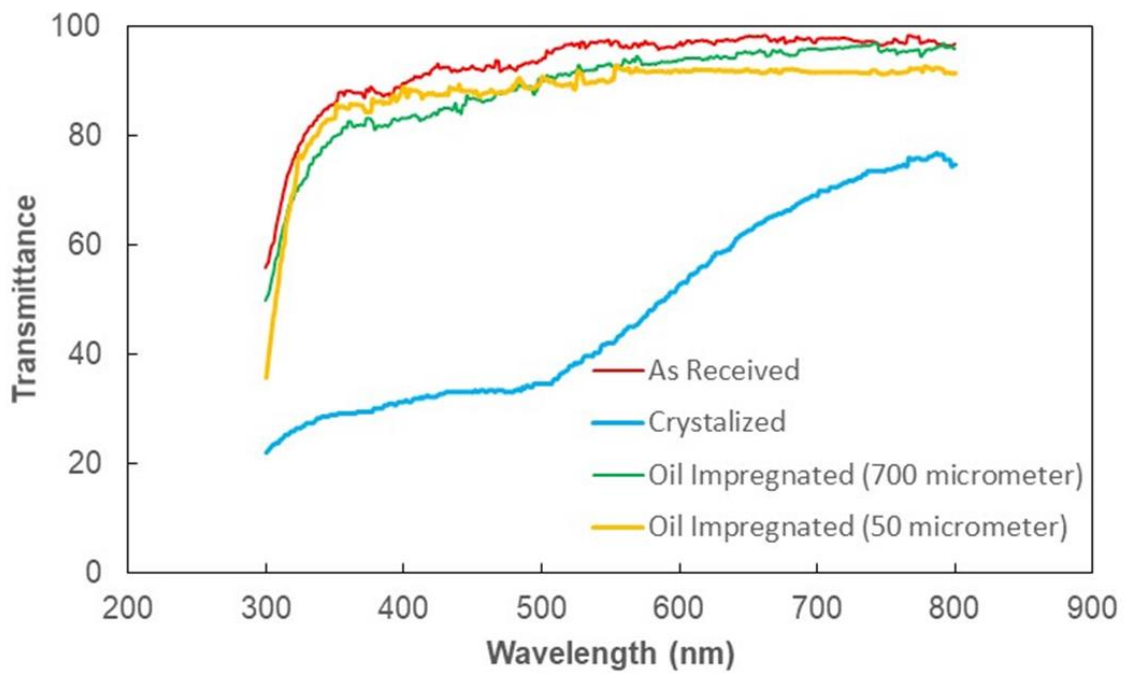


Figure 37 Optical transmittance of untreated, crystallized, and crystallized-oil impregnated polycarbonate. Spherules and fibrils on the crystallized surface cause diffuse reflection and partial absorption of incident UV visible radiation while lowering specular transmittance (wavelength-dependent transmittance). The increasing wavelength of incident optical radiation lowers diffuse reflection and absorption from the crystallized surface

The dust particles have varying shapes and sizes, and the average dust particle is assessed via particle analyzer (Malvern Panalytical, Mastersizer 3000), which is about 1.2 μm .

Figure 38 shows dust particles, which are composed of small and large sizes. Small particles adhere to the large particle surface, which is because of the non-stoichiometric composition for the compounds (NaCl and KCl) formed in the dust. This is noted from Table 5, in which elemental constituents of dust is given. For small dust particles ($\leq 2.5 \mu\text{m}$), the stoichiometric ratio of elements for NaCl and KCl does not satisfy, which in turn creates charges on the particles while contributing to the attachment of small particles to the large ones (Figure 38). The small size dust particles can adhere to the surface the charges and extra efforts are needed for mitigating the dust from the dry crystallized sample surface. Therefore, the use of silicone oil may reduce the dust particle adhesion over the crystallized surface and sliding droplets can be able to pick up the dust from the oil film surface. The optical transmittance of the oil-impregnated surface is reassessed and findings are shown in Figure 37. The optical transmittance of the crystallized surface enhances notably after oil spreading; however, the influence of the oil film thickness (700 μm and 50 μm) is not significant on the optical transmittance, i.e. optical transmittance remains high for both impregnated surfaces.

Table 5 Elemental constitute of dust particles (wt%). Increasing dust particle size causes reduction in alkaline earth metal (Ca) and silicone (Si); however, alkaline metals (Na and K) and chlorine (Cl)

Size	Si	Ca	Na	S	Mg	K	Fe	Cl	O
$\geq 1.2 \mu\text{m}$	11.6	8.5	2.1	1.1	2.5	0.8	1.2	0.4	Balance
$< 1.2 \mu\text{m}$	10.4	7.7	2.5	2.1	1.8	1.2	1.1	1.1	Balance

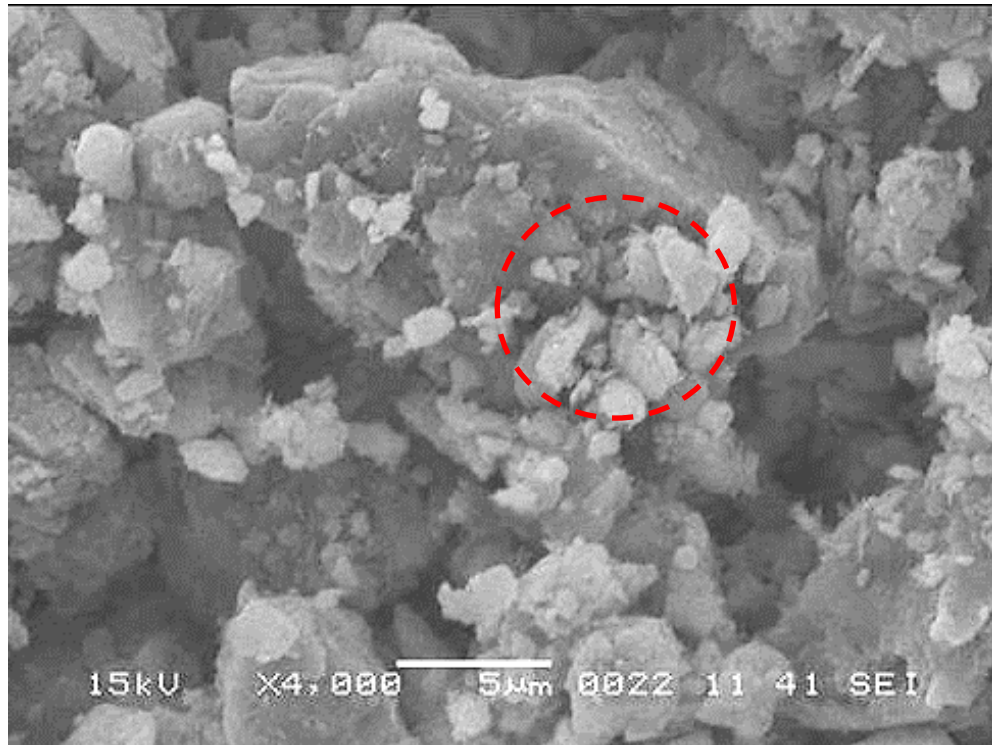


Figure 38 SEM Micro-image of dust particles. Dust particles have various shapes and sizes. Small dust particles adhere to large size particles forming clustering-like structures as shown in the red dotted circle. The attachment of small particles demonstrates that these particles have increased polar forces

5.2.2 Cloaking Procedure of Oil and Water over Dust Particles

Mitigating dust from the oil film by a sliding water droplet is challenging because of the oil and water infusions (cloaking) on the dust particle. It is worth mentioning that water droplets can cloak over the dust particle surface during the course of sliding transition over the oil surface. In order to determine the liquid (water and oil) infusion velocity over the dust particles, many experimental tests are conducted and temporal progression of water and oil height over the dust particle surface is recorded via the high-speed facility. Figure 39.a and Figure 39.b show the optical images of the stationary dust particle prior and after oil infusion with time, respectively, while Figure 40 shows infusion (cloaking) velocity of water and silicone oil on the stationary dust particle. It is worth mentioning that the tracker program is used to obtain infusion velocity from high-speed data. Infusion

height of the water over the particle ($\sim 30 \mu\text{m}$) is larger than that of silicone oil infusion height in the early period, i.e. water infusion takes place at a faster rate than that of silicone oil. This results in a larger water infusion velocity over the dust surface than that corresponding to silicone oil. As time progress, the water and oil infusion velocities reduce and they become almost the same (silicone oil and water). Moreover, the decay of the infusion velocity is associated with the time, i.e. $V_{\text{inf}} \sim t^{-n}$, here V_{inf} is the infusion velocity of the liquid and it takes the value of about 1/4 [176]. Although silicone oil and water can spread over the dust particle surface, because of positive spreading coefficient (S), energy dissipation, due to viscous effect on the particle surface and gravitational pull over the particle height, slows down the liquid infusion on the surface [176]. Liquid infusion over dust surface is associated with Joos' law [177]. The liquid energy used during the infusion is related to the Ohnesorge number ($Oh = \mu/\sqrt{\rho a \gamma_L}$), where a represents the particle size [178]. The Ohnesorge number takes different values for water and silicone oil because of density and viscosity of the fluids, i.e. density of water is 1000 kg/m^3 , viscosity is $0.7644 \times 10^{-3} \text{ Pa.s}$, and surface tension is 72.3 mN/m while the density of silicone oil is 935 kg/m^3 , viscosity is $0.92 \times 10^{-2} \text{ Pa.s}$, and surface tension is 35 mN/m . Hence, the Ohnesorge number takes the values of 0.082 and 0.016 for water infusion on the dust particle sizes of $1.2 \mu\text{m}$ and $30 \mu\text{m}$, respectively while it takes values of 1.47 and 0.294 for silicone oil for the same sizes dust particles. Hence, energy dissipated by the silicone oil becomes larger than water during the complete infusion (cloaking) over the dust particle surface. This becomes more evident for the large size dust particle. Hence, the temporal behavior of the infusion height of the silicone oil over the dust particle surface becomes gradual as compared to that of water.

Once the liquid droplet is created on the surface, droplet height reduces because of the bulging of droplet volume under gravity while causing droplet puddling on the surface. Once a water droplet is formed on the oil surface, a similar response is observed; however, silicone oil spreads over the water droplet surface due to the lower surface tension of silicone oil as compared to water. It is worth mentioning that the interfacial resistance between oil and water is lower as compared to water surface tension. This causes oil infusion over the water droplet surface. The water droplet free surface (exposed to air) can be approximated by a spherical cap with a radius of r_o which can be estimated using Eq. 4.14 [164]. The forces can be encountered due to the droplet pinning under interfacial shear across the boundary of water and oil. The force equilibrium for the droplet, which is partially floating in the oil film, is estimated using Eq. 4.15 [164]. Rearrangement of the vertical force balance yields Eq. 4.16 where an approximation leads to;

$$2r_o\gamma_{w-si}\sin(\theta_c + \alpha) - \frac{h_o^2}{3}(3r_d - h_o)\rho_{Si}g = 0 \quad (5.7)$$

here γ_{w-si} is water-silicone oil interface tension, ρ_{Si} is silicone oil density, and g is gravity [164]. The experimental data demonstrate that $h_o \cong 0.92$ mm for 20 μ L droplet, which agrees with the value estimated from the vertical force balance ($h_o \cong 1.02$ mm). Moreover, as the oil-impregnated surface is inclined, both the water droplet and the oil film flow in the direction of gravity. The state of the film velocity ($\frac{\partial h_f}{\partial t}$) on the tilted sample with the tilt angle of $\delta \leq \pi/2$ is connected to the capillary number, $Ca = \frac{\mu_s u}{\gamma_s}$, where u is the velocity of the oil film and μ_s viscosity of oil [179]. The liquid velocity of the film on the tilted surface is formulated by Yilbas et al. which is demonstrated in Eq.

4.17 [179]. The numerical solution of the equation for the film velocity yields the film velocity is 0.02 mm/s for the film thickness 700 μm and the tilt angle of 5° . The film velocity obtained by a tracker program using the high-speed recorded data is about 0.017 mm/s, which is closer to the numerical prediction. Moreover, since the crystallized surface, where the oil film is deposited, has a hydrophobic texture with 3.2 μm average roughness, slip conditions can occur across the textured surface and the oil film. The slip velocity can be formulated through the slip length which is estimated using Eq. 4.5 [180]. The solid fraction of the crystallized surface is evaluated via AFM and SEM micrographs and it is estimated at about $\phi = 0.35$. Incorporating the viscosity of silicone oil (0.92×10^{-2} Pa.s) and water (0.89×10^{-3} Pa.s), film thickness (700 μm), and a solid fraction, the slip length yields about $b = 44$ μm . Moreover, the slip velocity can be found from Eq. 4.20 [175], which can be further simplified after considering a Couette flow in clearance between the bottom of the droplet and oil. Hence, the slip velocity in terms of film velocity and the slip length yields Eq. 4.21. Moreover, the velocities of the partially immersed droplet and the oil film are different, which creates a shear resistance across the droplet and the oil. The frictional stress can be estimated via Eq. 4.22 [181]. It is also known that shear stress in between the textured surface and the oil can be approximated via Eq. 4.23. The shear stresses on the droplet and on the oil at the interface have similar orders (stress continuity). This yields the relation between the slip and the droplet velocities which is demonstrated in Eq. 4.24. This equation, further, proves that the droplet velocity becomes much larger than the film velocity ($V_d > u_f$). Moreover, energy dissipated by the sliding water droplet on the oil film via shear resistance is related to the shear rate created at the ridges due to oil infusion over the droplet surface, the air drag

acting on the droplet cap in the air, and the lateral component of the surface tension around the droplet rim. The dissipated energy is formulated in Eq. 4.33 by Yilbas et al. [175]. In addition, work is done by the sliding droplet towards overcoming the droplet pinning, which can be counted for the droplet's additional energy dissipation. The work required to overcome the pinning is estimated via Eq. 4.34 [164]. The potential and kinetic energy changes along the incremental length scale are estimated using Eq. 4.37 and Eq. 4.35, respectively. Therefore, the change of droplet potential energy along the incremental length scale overcomes the frictional energy dissipation and the work required for pinning, and, in addition, the kinetic energy for creating the droplet motion on the oil surface. The potential energy change of the droplet per unit droplet mass along the length scale of 44 mm of 10° inclined surface with 700 μm thick oil is 0.075 J/kg while the kinetic energy is 3.125×10^{-3} J/kg. Hence, a large amount of energy is dissipated in the course of droplet sliding, i.e. almost 96% of droplet potential energy is dissipated to overcome shear resistance and pinning of the droplet

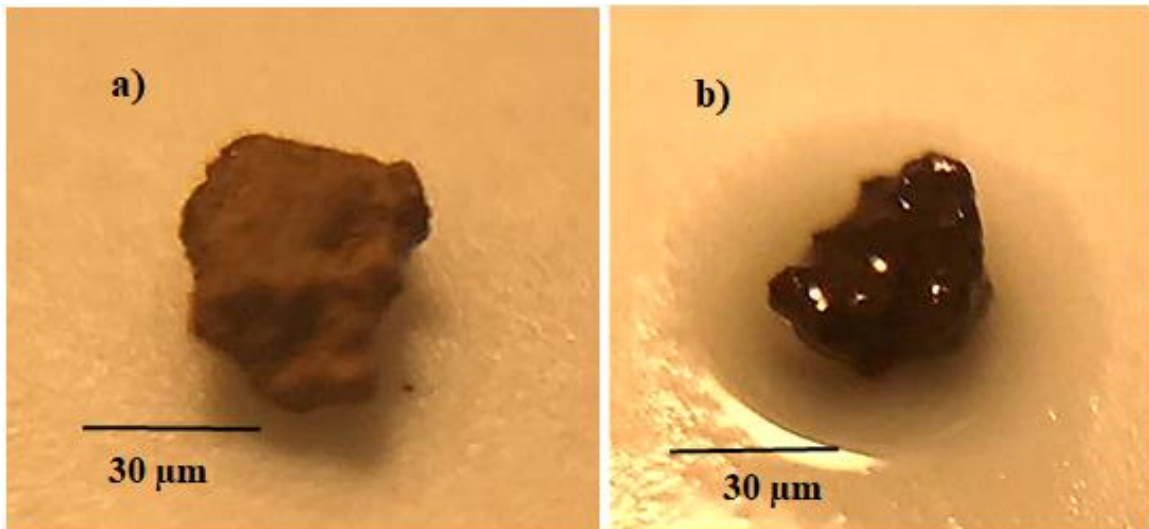


Figure 39 Optical image of dust particle: a) before oil infusion and b) after oil infusion. Infused oil totally covers the dust particle surface, which indicates the positive spreading coefficient of oil over the particle surface

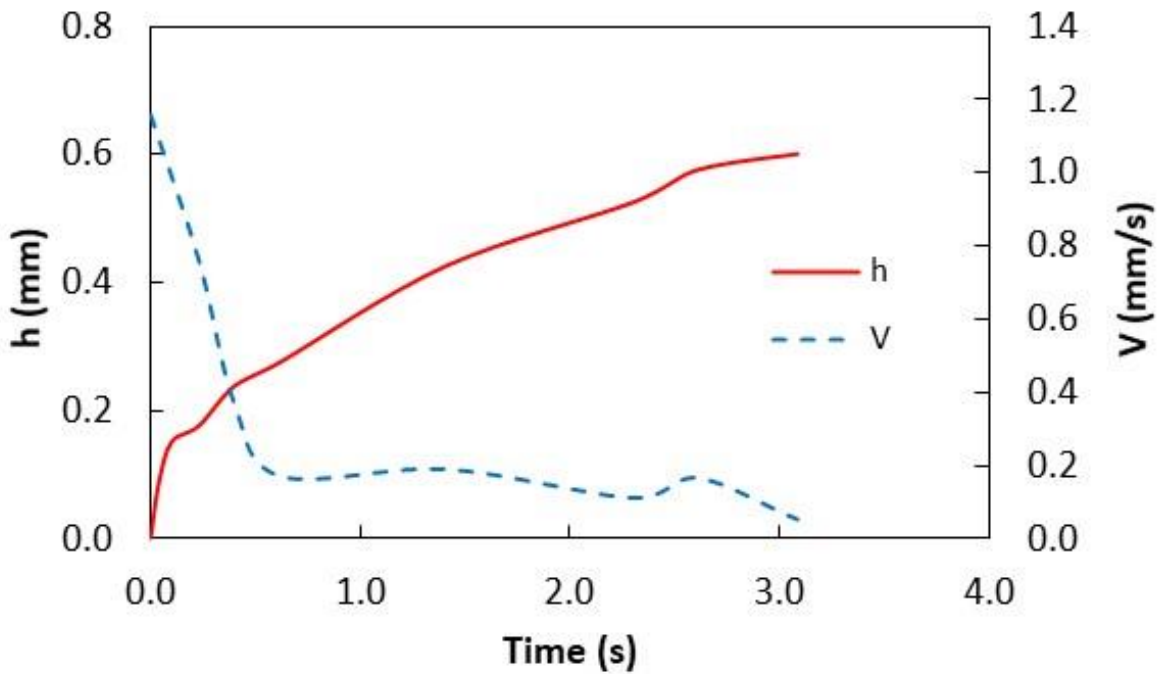
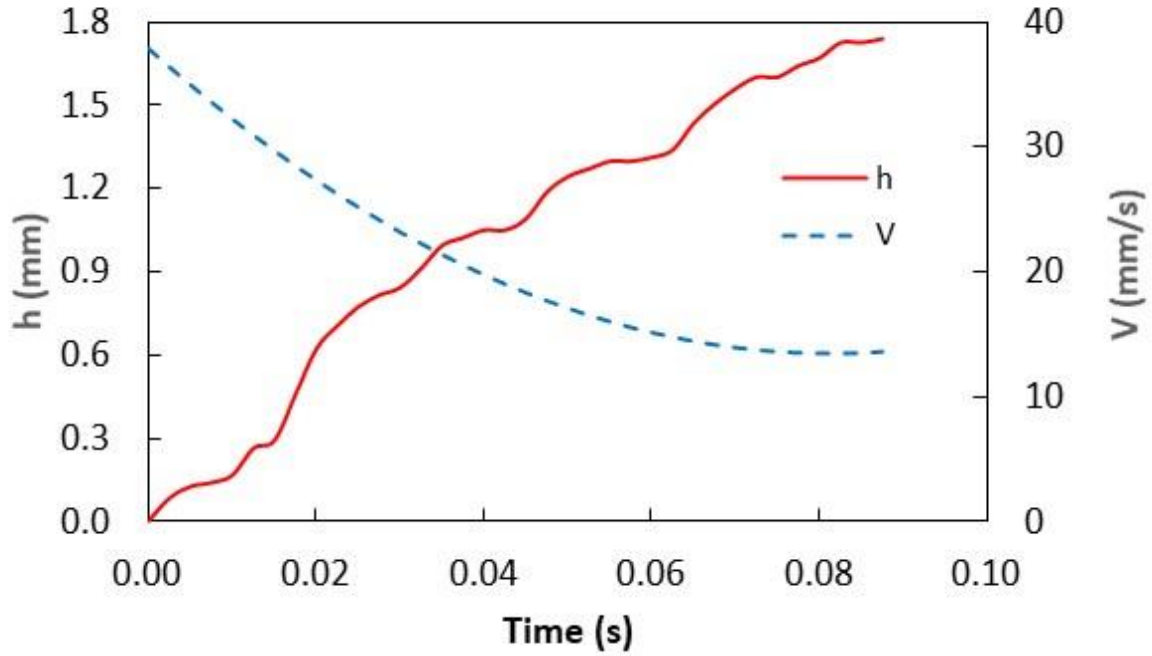


Figure 40 Infusion height and infusion velocity with time: a) water, and b) silicone oil. h represents infusion height on dust surface and V is the infusion velocity

5.2.3 Oil Film Thickness Influence

Figure 41.a and Figure 41.b depict images of the droplet over the thin ($50\ \mu\text{m}$) and thick oil ($700\ \mu\text{m}$) films at which the oil ridge is formed around the water droplet rim because of oil infusion over the water droplet surface, particularly for large oil film thickness ($700\ \mu\text{m}$). The oil ridge height is about $\sim 0.32\ \text{mm}$ around the droplet rim (three-phase-contact-line) for $700\ \mu\text{m}$ thick oil film; however, it becomes $\sim 0.09\ \text{mm}$ for $50\ \mu\text{m}$ thick oil film. Hence, thinning the oil film thickness reduces the ridge height around the droplet.

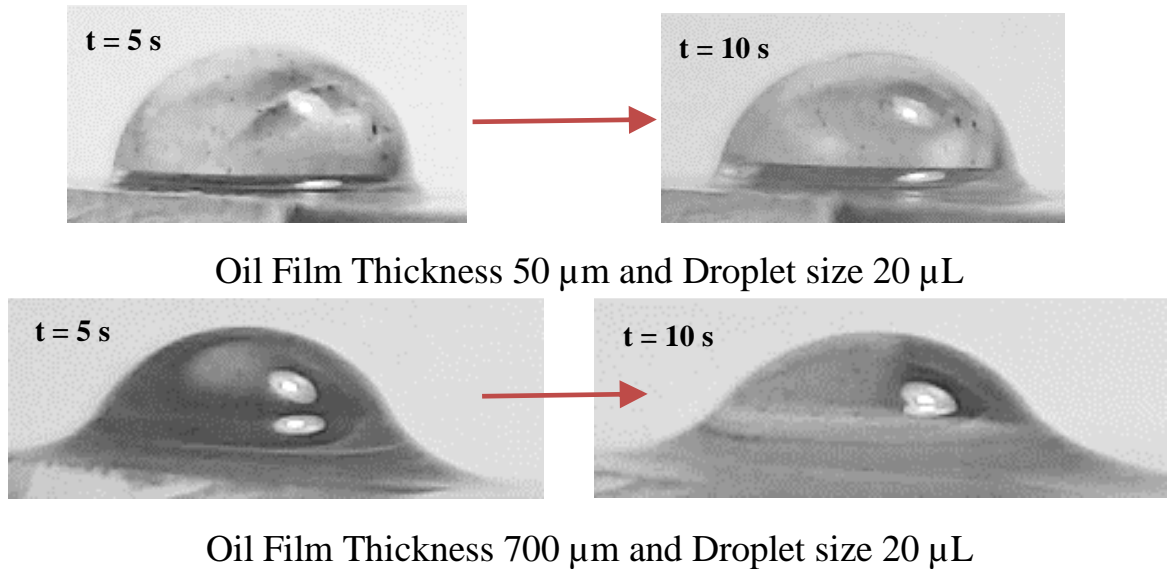


Figure 41 Optical image of silicone oil infusion on water droplets at different times. The time of droplet motion is started and recorded as the droplet is dispensed on the oil-impregnated sample surface

Figure 42 shows droplet velocity on the thin oil film ($50\ \mu\text{m}$ thick) with distance for two volumes and two tilt angles. In the early period of sliding, the velocity increases to attain maximum and as the droplet sliding continues along the inclined film, the velocity

decreases gradually. This behavior is observed for both inclination angles and droplet volumes. This is mainly related to the oil ridge formation in the droplet neighborhood through oil infusion on the water droplet. Oil infusion in the early sliding period is small preventing the oil ridge formation. As the droplet sliding progresses, the oil ridge forms around the droplet because of the oil infusion during the droplet sliding. Hence, the interfacial fluid resistance between the oil and the droplet liquid increases along the droplet circumference, which causes slowing down the droplet motion along the inclined surface. Moreover, as the droplet size increases, interfacial resistance along the droplet ridge increases because of the increased droplet diameter with increasing droplet volume. However, increased droplet inertial force, because of the droplet mass increase, enhances the droplet velocity despite the fact that interfacial resistance at oil droplet along with the ridge increases. In the case of the thick silicone oil film ($\sim 700 \mu\text{m}$) impregnated sample surface, the sliding velocity of the droplet increases to reach its maximum, and, later, it decreases gradually along the inclined surface (Figure 43). This behavior is similar to the thin oil film case (Figure 42). The sliding velocity attains larger values for the thick oil film case than that of the thin film case. It is worth noting that the droplet immersion becomes more as the film thickness becomes larger ($\sim 700 \mu\text{m}$). Hence, it is expected that the fluid resistance around the immersed area of the droplet is to increase. However, the attainment of the large velocity on the thick oil film suggests that the droplet on the thin film ($\sim 50 \mu\text{m}$) penetrates into the oil film and makes physical contact on the crystallized surface. This increases the shear resistance at the droplet bottom. In addition, the droplet located on the thick oil film floats in the oil film and creates a slip condition at the droplet bottom, which in turn reduces the shear resistance across the film and the droplet.

Therefore, the velocity of the droplet attains higher values for the large thickness oil-impregnated sample surface.

Figure 44 and Figure 45 show droplet sliding velocity on the inclined thin and thick oil films ($\sim 50 \mu\text{m}$ and $700 \mu\text{m}$) with the presence of the dust particle over the oil surface for two droplet volumes and two tilting angles of the sample. Figure 46 depicts the optical images of different stages of the dust particle mitigated by the sliding water droplet on the inclined oil film. It is worth mentioning that the dust particle size selected is large enough to be recorded by a high-speed facility; hence, the selected particle size is $75 \mu\text{m}$.

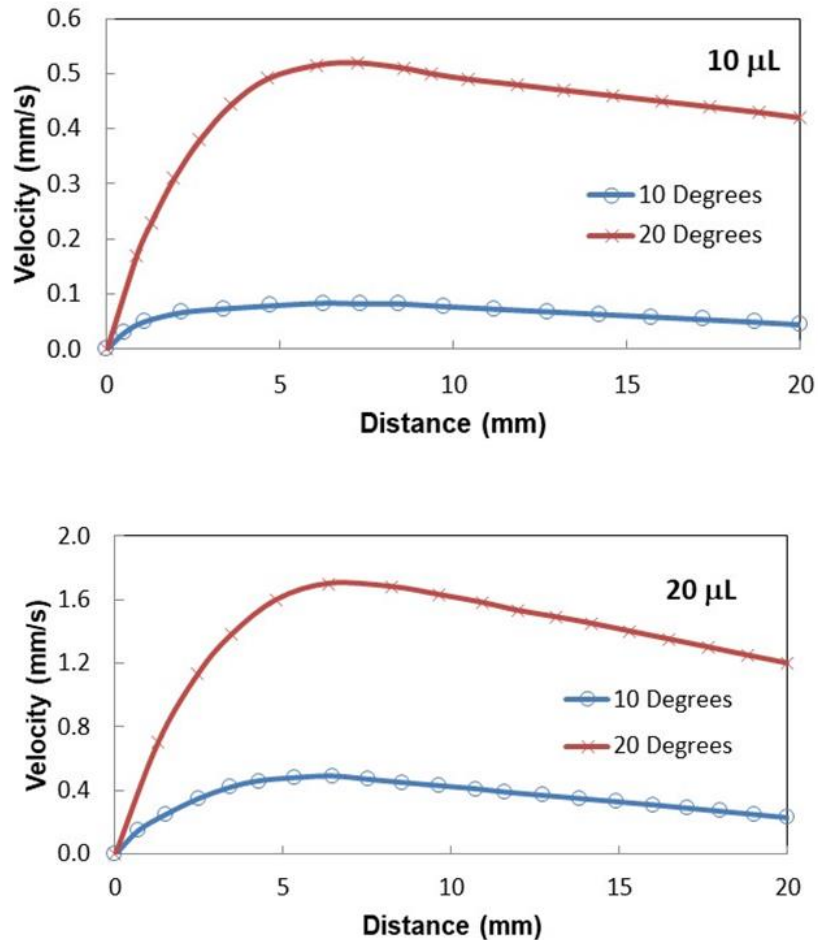


Figure 42 Droplet sliding velocity on the inclined oil-impregnated surface for two droplet volume and inclination angles. Oil film thickness is $50 \mu\text{m}$

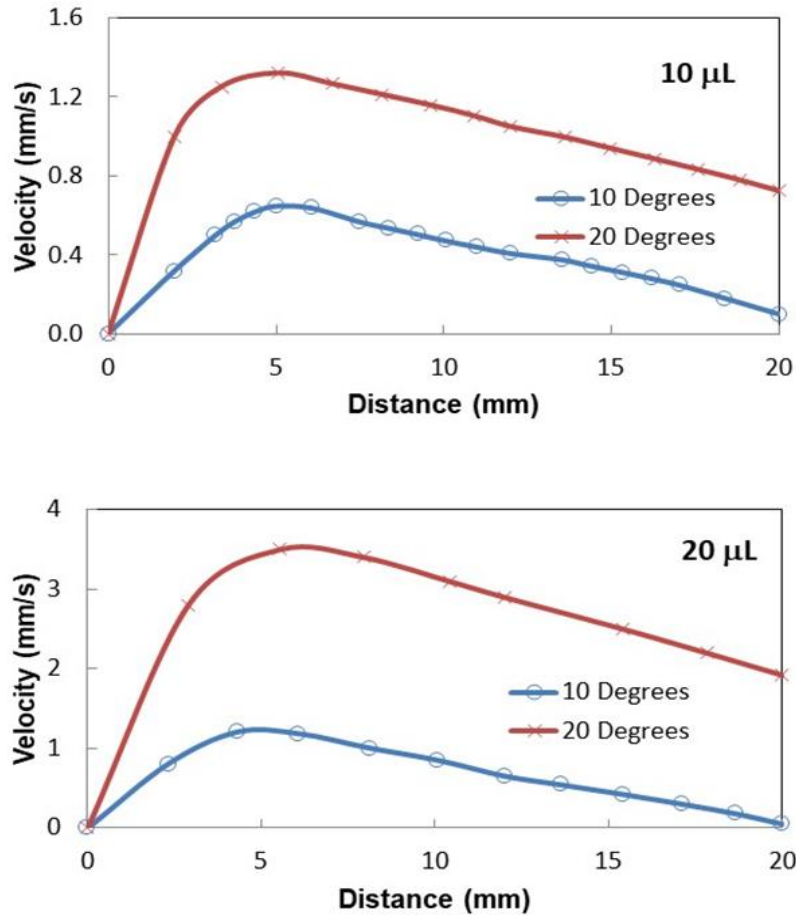


Figure 43 Droplet sliding velocity on the inclined oil-impregnated surface for two droplet volume and inclination angles. Oil film thickness is 700 μm

As the sliding droplet approaches the vicinity of the dust particle, the oil ridge around the droplet first contacts the dust particle surface. However, the dust particle height is larger than the oil ridge height, the infusion of oil from the oil ridge towards the dust particle surface is expected to be negligible. In addition, the contact duration between the oil ridge and the dust particle is short, which reduces the amount of oil-infused over to the dust particle surface. Moreover, once the droplet fluid wets the dust particle on the oil surface, droplet sliding velocity reduces, and the part of the dust particle surface, which is not infused by the oil, is infused by the fluid of the droplet. In the course of fluid infusion over the particle surface, the sliding velocity of the droplet reduces further. Once the

droplet liquid cloaks over the dust, the particle is picked up by the droplet fluid and the particle is reoriented inside the sliding droplet, which can be observed from Figure 46. During the dust particle reorientation, the sliding droplet mass increases slightly and the inertia force increases while causing droplet sliding velocity to increase along the inclined surface. However, as the dust particle is oriented at the droplet trailing edge, which is opposing to the droplet front edge in the sliding direction, the droplet velocity reduces considerably. This situation can be observed in Figure 46. Moreover, it becomes true for all volumes of the droplet, the tilting angle of the sample, and oil film thickness. The possible explanation of this behavior is that the dust particle in the droplet trailing edge immerses into the oil and it is anchored by the oil film. This creates the pinning influence on the sliding droplet, which gradually ceases sliding on the oil film, i.e. sliding motion terminates and the sliding velocity becomes zero on the oil film. The inclination angle has a significant influence on the droplet sliding velocity. In this case, reducing the inclination angle from 20° to 10° lowers the sliding speed from 0.98 mm/s to 2.02 mm/s. For a small inclination angle (10°), the dust particle position in the sliding droplet has a considerable effect on the sliding velocity. In this case, droplet sliding velocity attains high values as the dust particle is located in the central region of the droplet. As the dust particles move towards the trailing edge of the droplet, the sliding velocity reduces considerably. Hence, the dust particles are partially immersed in the oil film at the droplet edge while creating the anchoring effect on the droplet sliding velocity.

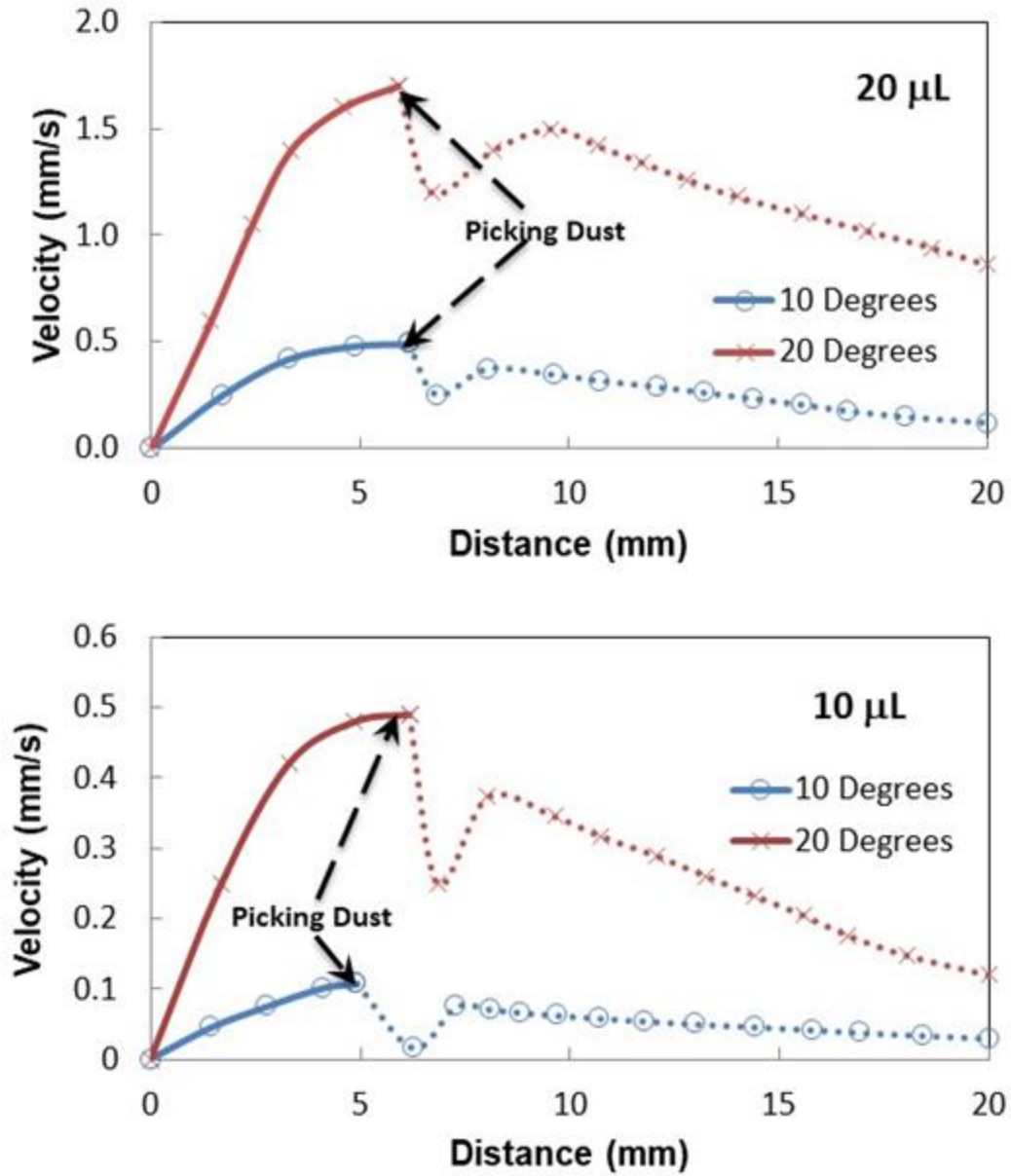


Figure 44 Droplet sliding velocity on the inclined oil-impregnated surface with the large dust particle presence for two droplet volumes and tilting angles. Oil film thickness is 50 μm

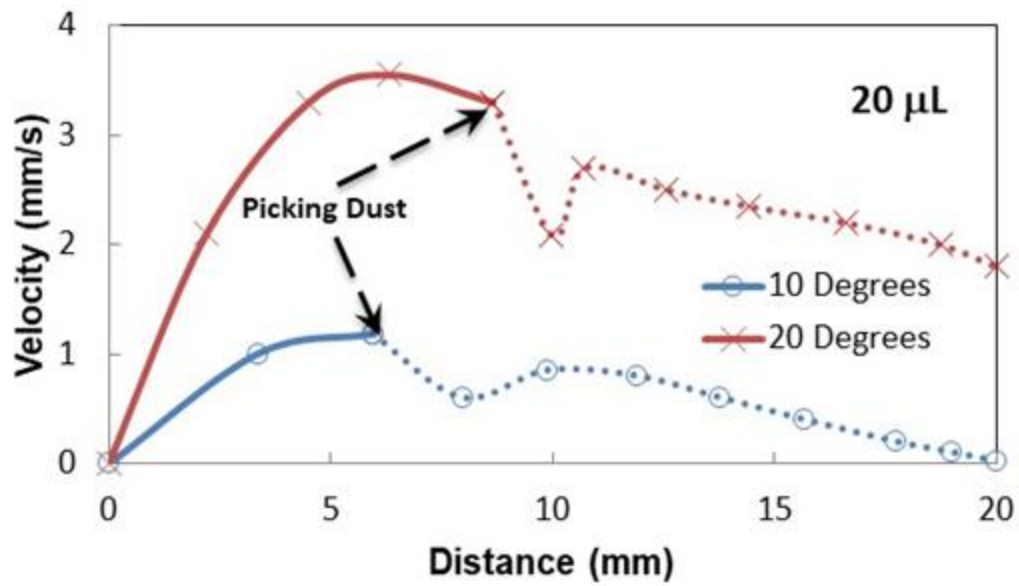
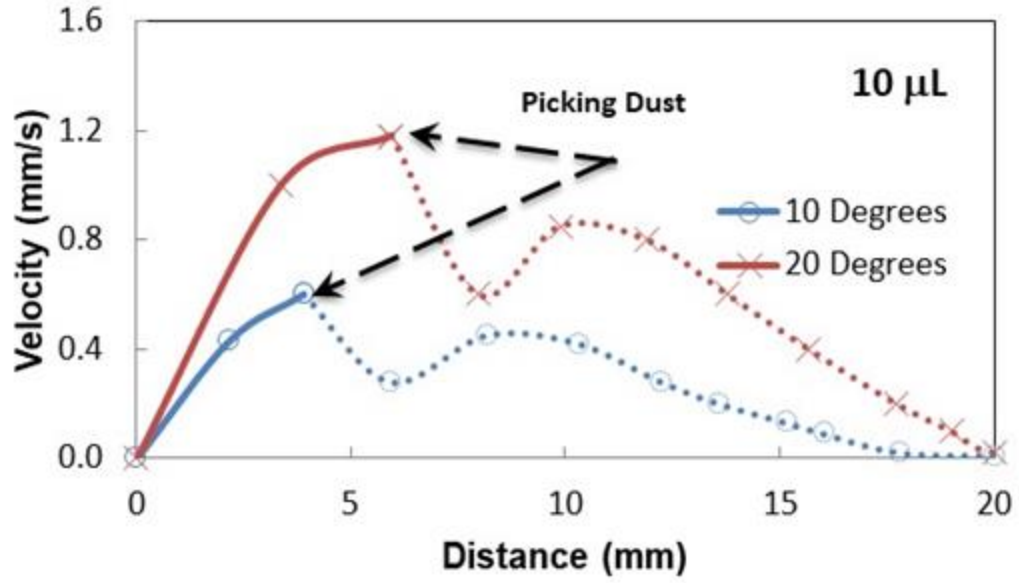


Figure 45 Droplet sliding velocity on the inclined oil-impregnated surface with large dust particle presence for two droplet volumes and tilting angles. Oil film thickness is 700 μm

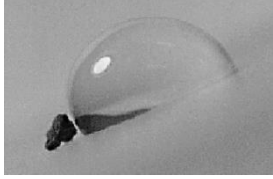









Oil Thickness = 50 μm Inclination: 20° Size: 20 μL Droplet	Oil Thickness = 700 μm Inclination: 20° Size: 20 μL Droplet
 <p>V= 1.65 mm/s</p>	 <p>V= 3.40 mm/s</p>
 <p>V= 1.21 mm/s</p>	 <p>V= 2.35 mm/s</p>
 <p>V= 1.41 mm/s</p>	 <p>V= 2.78 mm/s</p>
 <p>V= 1.26 mm/s</p>	 <p>V= 2.24 mm/s</p>
 <p>V= 0.98 mm/s</p>	 <p>V= 2.02 mm/s</p>

Figure 46 Stages of the droplet on inclined oil film for two oil film thicknesses. The dark color represents the dust particle

5.3 Carbonated Water Droplet on Dusty Hydrophobic Surface

Glass surfaces are hydrophobized and the behavior of the droplet formed by carbonated water on the dusty hydrophobic surface is examined. The motion of bubbles formed in a sessile droplet and the droplet fluid (carbonated water) interactions with the dust particles are analyzed. The dust removal rate from the hydrophobic surface is evaluated.

5.3.1 Properties of Hydrophobized Glass Surface and Dust Particles

Glass surfaces are hydrophobized through the depositing of functionalized silica particles. Figure 47.a depicts an SEM micrograph of the coated glass surface while Figure 47.b shows the atomic force microscope line scan on the coated surface. The coated surface possesses closely located and agglomerated nano-size silica-particles. Agglomeration of the particles form cluster-like textures with some small porous-like structures in between clusters. The particles agglomeration is attributed to the condensing monomers, which can grow faster than the nucleation rate [182]. However, the maximum and the minimum texture heights difference is small (Figure 47.b). The average roughness of the surface is about 150 nm while the roughness parameter (ratio of area covered by pillars over the projected area) is about 0.51. The coating surface free energy is evaluated using the droplet method while utilizing water, glycerol, and ethylene glycol[183], [184]. The surface free energy of the coated surfaces is determined as 35.51 mJ/m². The contact angle of the water droplet on the coated surface is about 150° ± 2° and the contact angle hysteresis of 8° ± 2°. Hence, coating results in a hydrophobic wetting state on the sample surfaces.

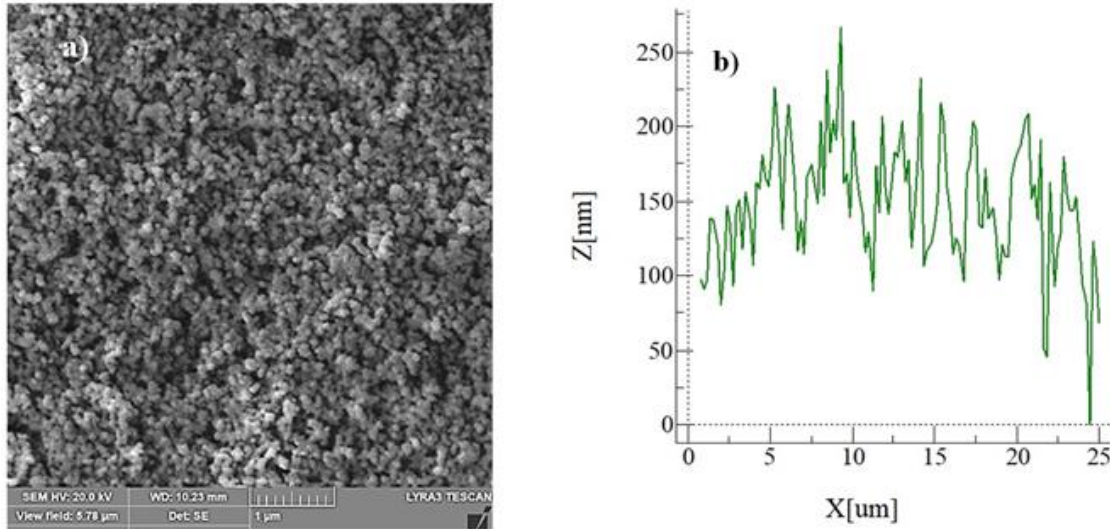


Figure 47 SEM micrograph and AFM line scan of functionalized silica particles deposited surface: a) SEM micrograph and b) AFM line scan

Figure 48.a and Figure 48.b show SEM micrograph of the dust particles while Figure 48.c shows the size distribution of the dust particles obtained from the particle size analyzer (Microtrac Nanotrac Wave Nanotechnology Particle Size Analyzer). Dust particles have different sizes and shapes where the average dust particle is about 1.2 μm. Small size dust particles agglomerate and form a clusters-like appearance (Figure 47.a) and small size dust particles adhere to the large size particle surface (Figure 47.b). The electrostatic charges developed on the small particles are responsible for the adhesion on the large size particles [185]. Figure 49 depicts an X-ray diffractogram of dust particles while Table 6 gives the dust particles elemental constituents. The peaks in Figure 49 demonstrate that alkaline (Na, K) and alkaline earth (Ca) metals form compounds with chlorine (Cl). This is related to the salt compound's presence in the near region of the gulf area since Dammam (where dust is collected) is in the near region of the Gulf. Sulphur is related to calcium, which takes the form of anhydrite or gypsum (CaSO_4). Iron is related to clay-aggregated hematite (Fe_2O_3). EDS data (Table 6) demonstrates that iron, calcium, silicon, chlorine, sodium, potassium, and oxygen are present in the dust

particles. However, elemental composition changes slightly as the size of the dust changes, i.e. small dust particles possess relatively higher oxygen content as compared to larger dust particles. The surface free energy of the dust particles is assessed using the droplet method [183]. The contact angle of the liquids used (water, glycerol, and ethylene glycol) are measured using the Washburn technique [186]. The dust particles are put into a 3 mm diameter glass tube, which enables to draw-up the liquid due to the capillary action. The rate of increase of mass inside the tube is associated with the Washburn formula

$$\frac{(\Delta m)^2}{\Delta t} = \frac{c \cdot \rho^2 \gamma \cos \theta}{\mu} \quad (5.8)$$

where Δm is the mass gain, Δt represents the duration for the mass gain (flow time), c corresponds to the capillary constant of the dust, ρ is the fluid density, θ is the contact angle, μ is the fluid viscosity. The capillary constant for the dust particles is evaluated using n-hexane since it results in zero contact angle ($\theta = 0$). Several tests were carried out to secure the accurate result for the capillary constant. The capillary constant for the dust particles is determined as $5.82 \times 10^{-16} - 6.54 \times 10^{-16} \text{ m}^{-5}$. The variation of the capillary constant is because of the effect of the dust particle sizes and the shapes. Moreover, solid pellets are made from dust particles via slight compression. The contact angle measured for water incorporating dust pellet is $38.2^\circ \pm 3^\circ$, however, the Washburn technique results in $37.4^\circ \pm 3^\circ$. Hence, both methods result in almost similar water droplet contact angles. The surface free energy of the dust is evaluated from a solid-liquid system [183], [184], [187], which is:

$$\gamma_L (\cos \theta + 1) = 2\sqrt{\gamma_S^L \cdot \gamma_L^L} + 2\sqrt{\gamma_S^+ \cdot \gamma_L^-} + 2\sqrt{\gamma_S^- \cdot \gamma_L^+} \quad (5.9)$$

The subscripts S and L represent solid and liquid phases, respectively, γ_s corresponds to the solid surface free energy, γ_{SL} is the interfacial solid-liquid free energy, γ_L represents the liquid surface tension, θ is the contact angle, γ^+ and γ^- are the electron acceptor and electron donor parameters of acid-base component of the solid and liquid surface free energy, respectively. Table 7 provides the Lifshitz-van der Waals components and electron-donor parameters used in the surface free energy assessments [183], [184], [187]. The surface free energy measured for the dust is about 111.5 ± 7.5 mJ/m². The experiments are repeated eight times to satisfy the repeatability of the measurements and the error estimate is about 7%.

Table 6 Elemental composition of dust particles (wt%)

	Si	Ca	Na	S	Mg	K	Fe	Cl	O
Size ≥ 1.2 μm	11.8	8.3	2.2	1.3	2.5	0.8	1.2	0.4	Balance
Size < 1.2 μm	10.2	7.3	2.7	2.5	1.3	1.2	1.1	1.1	Balance
Dust Residues	9.5	7.1	1.9	1.3	2.4	0.9	0.9	0.4	Balance

Table 7 Lifshitz-van der Waals components and electron-donor parameters used in the simulation [185], [186], [189]

	γ_L (mJ/m ²)	γ_L^L (mJ/m ²)	γ_L^+ (mJ/m ²)	γ_L^- (mJ/m ²)
Water	72.8	21.80	25.5	25.5
Glycerol	63.3	33.11	10.74	21.23
Ethylene glycol	48.2	31.09	6.59	11.16

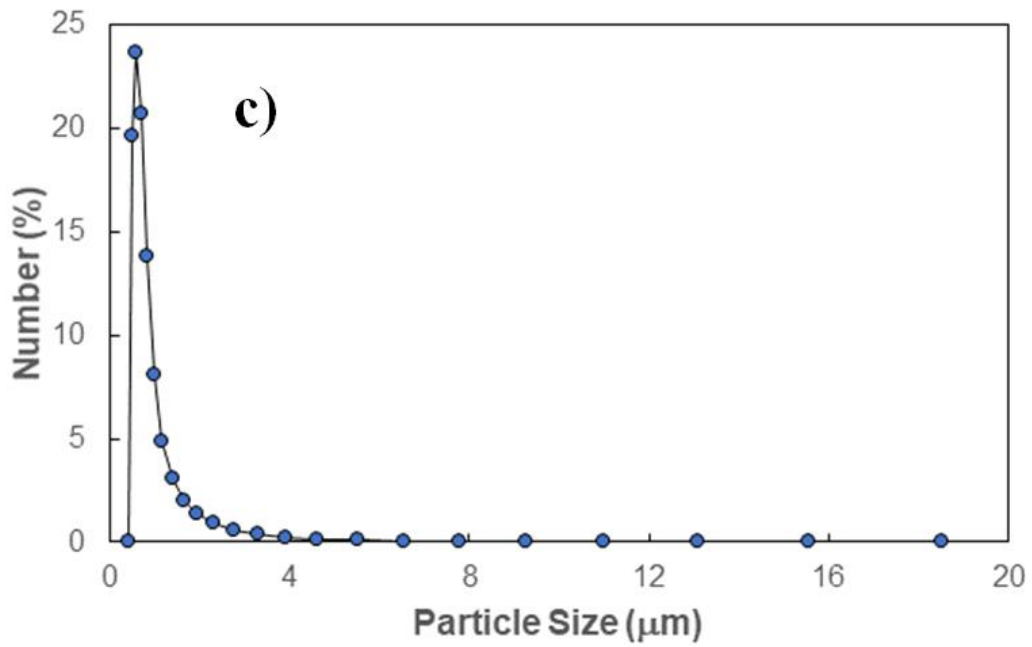
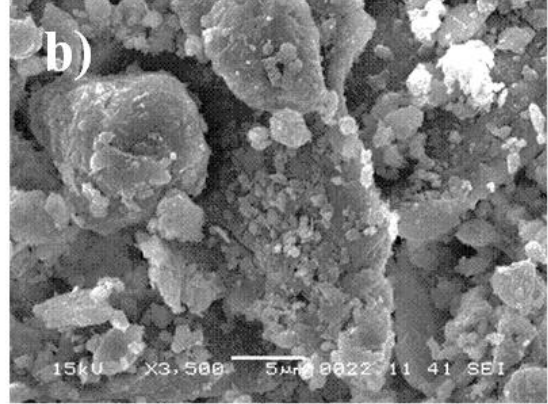
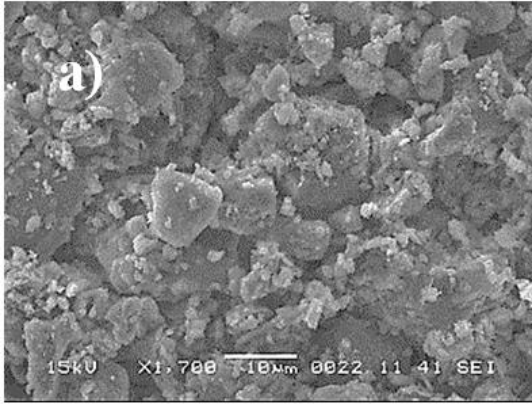


Figure 48 SEM micrograph and size distribution of dust particles: a) SEM micrograph showing various shapes and sizes of dust particles, b) SEM micrograph of dust particles showing small dust particles attachment at large particle surfaces, and c) size distribution of dust particles

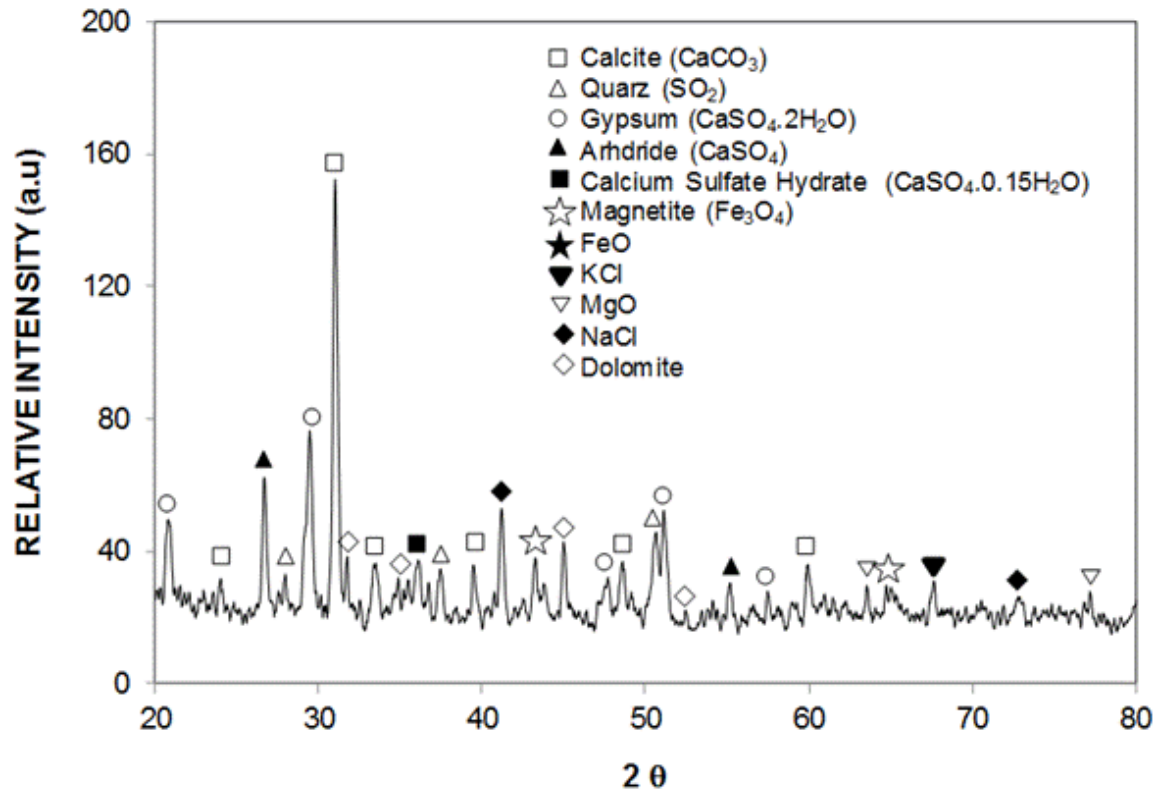


Figure 49 X-ray diffractogram of dust particles

5.3.2 Cloaking Procedure for Carbonated Water

Several tests are carried out to evaluate the infusion of carbonated water (cloaking) on the dust particle surface. Since the dust particle contains alkaline and alkaline earth compounds, these compounds dissolve in water while increasing the surface tension of the liquid [188]. In addition, salt reaction with carbonated water results in excessive gas bubble formation in the region of the dust particles. The fluid behavior in the close region of the dust particle is altered by the bubbles formed in this region. This locally generates fluid acceleration because of the bubble motion. Hence, the fluid infusion (cloaking) on the dust particle becomes different for carbonated water than that of the desalinated water. Figure 50 shows the cloaking velocity with time for carbonated and desalinated water. It is worthy to note that the fluids resulting in a positive spreading rate ($S > 0$) on

the irregularly shaped particle surfaces, such as dust particles, cause cloaking of the particle surface [189]. The carbonated water results in increased cloaking velocity, which is related to the bubbling of the water in the near vicinity of the dust particles. The spreading rate of water on the dust satisfies the energy balance, i.e.:

$$S = \gamma_s - \gamma_L - \gamma_{s-L} \quad (5.10)$$

here, γ_s is the surface free energy of dust, γ_L is water surface tension, and γ_{s-L} is the interfacial tension between water and dust. The interfacial tension between the dust pellet and water was evaluated via introducing the Hemi-Wicking criterion. [190],[191]. The relation for interfacial tension results in

$$\gamma_{s-L} = \gamma_s - \frac{\gamma_L}{r} \cos\theta_w \quad (5.11)$$

Here, θ_w is the water contact angle on the pellet and r is the roughness parameter of pellet surface, which corresponds to the ratio of the area covered by the texture pillars over the projected surface area. The roughness parameter is obtained from AFM data and it is about 0.51, and the water droplet contact angle (θ) was $38.2^\circ \pm 3^\circ$. Therefore, the interfacial tension was 13.68 mJ/m^2 . Inserting the values in Eq. 5.5 results in $S = 25.82 \text{ mJ/m}^2$, which is greater than zero ($S > 0$). Hence, water spreads over dust and infuses (cloaks) on the dust surface. The spreading rate calculations and experiments are repeated for carbonated water (sparkling water). The findings revealed that the spreading rate for the carbonated water is about $S = 28.5 \text{ mJ/m}^2$, which is similar to the desalinated water. Hence, carbonated water infuses and cloaks on the dust surface. The cloaking velocity changes with time for desalinated and carbonated (Figure 50). The relation between the cloaking velocity and time is found to be in the form of $\sim kmt^{1/4}$. At the initial stage of cloaking, a single water layer forms on the surface of the dust and as the spreading

progresses, cloaking occurs in accordance with Joos' law [192]. The energy dissipated in the liquid during infusion is related to the Ohnesorge number ($Oh = \mu/\sqrt{\rho a \gamma_L}$), where, μ is the fluid viscosity, ρ , is the fluid density, γ_L is the surface tension of water and a is the particle size [193]. Using the dust particle size within the range of $1.2 \mu\text{m} - 20 \mu\text{m}$, the values of Ohnesorge number becomes smaller than one, which is within the range of $Oh \sim 0.025 - 0.105$). This demonstrates that the energy dissipated by water during infusion on the dust particle surface is small.

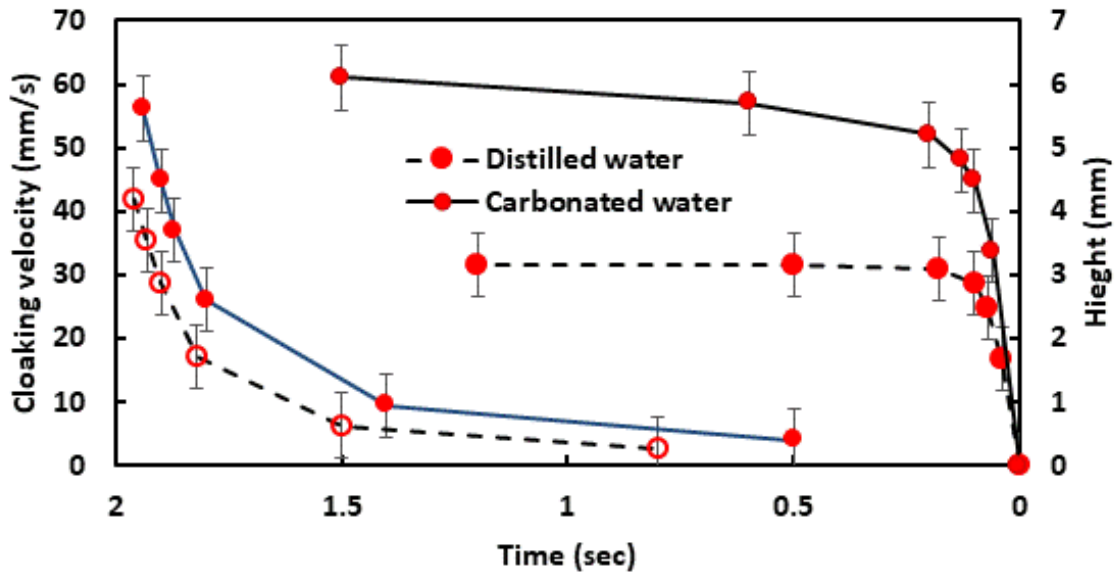


Figure 50 Distilled and carbonated water cloaking velocity and cloaking height on dust particle surface with time

5.3.3 Bubble Behaviour Inside Water Droplet

The bubble formation in the carbonated water droplet on the hydrophobic surface is related to Henry's law:

$$C_s = k_H P_g \quad (5.12)$$

where C_s is the saturation concentration of dissolved gas in water, K_H is Henry's constant and it depends on temperature, P_g partial pressure of gas phase) and the molecular diffusion described by Fick's law

$$J = -D\nabla C \approx D \frac{\Delta C}{\lambda} \quad (5.13)$$

here J is desorbed gaseous flux, D is the diffusion coefficient of the gas,

$$\Delta C = C_L - C_s \quad (5.14)$$

dissolved gas concentration difference between the water bulk (C_L) and the bubble interface in Henry's equilibrium (C_s), λ is the thickness of diffusive boundary layer at which dissolved gas gradient is present [194]. In line with Henry's law, the cavities of the texture on the hydrophobic surface cause saturation concentration at the ambient pressure of the dissolved gas, which is lower than the dissolved gas pressure in the bulk of the droplet fluid. The molecular diffusion results in net flux towards the cavity while causing nucleation of a growing bubble. As the gas bubble in the cavity site reaches a size at which the buoyancy force becomes larger than the pinning force, the bubble departs from the nucleated site while leaving a small gas bubble in the cavity. This causes a bubbling cycle starting over again. As the bubble departs in a quiescent droplet liquid, the relative velocity of the bubble-liquid interface improves the mass transfer, and the growth of the rising bubble increases at a higher rate than that formulated by the Epstein-Plesset equation

$$\frac{dR}{dt} = D\Lambda \left(\frac{P_L}{P_o} - 1 \right) \left(\frac{1}{R} + \frac{1}{\sqrt{\pi D t}} \right) \quad (5.15)$$

here R is the bubble radius, D is the diffusion coefficient of the desorbed gas, Λ is the Ostwald constant ($\Lambda = K_H R_o T$, R_o is the universal gas constant and T is temperature), P_L is the pressure in the liquid, P_o is the ambient pressure) [194]. On the other hand, the

moderate values of the bubble Reynolds number (0.35 – 12), the drag force can be approximated by the Stokes' law, which takes the form

$$F_D \sim \mu R v_b \quad (5.16)$$

where μ is the liquid viscosity, v_b is the bubble rising velocity [194]. Moreover, the velocity of the bubble can be approximated as:

$$v_b \approx \frac{2\Delta\rho g R^3}{9\mu} \quad (5.17)$$

where $\Delta\rho$ is the density difference between water and gas inside the bubble, g is the gravitational acceleration [195]. Hence, the velocity of the bubble with a diameter of 7.89×10^{-3} mm is estimated to be 0.013 mm/s using Eq. 5.17. However, the velocity formulation reported in the early study relies on the quasi-steady droplet bubble behavior, which differs from that of the transiently rising bubbles inside the droplet fluid. Therefore, further analysis for the interpretation of the bubble velocity needs to be considered. Since the bubble diameter is small (0.1 – 0.3 mm), Reynolds number (0.35 – 12), the Bond number is about 5.5×10^{-3} , and Morton number is 1.65×10^{-11} , the bubble is considered to be a spherical shape inside droplet fluid [196]. The force balance about the rising bubble inside the carbonated water droplet results in acceleration of the bubble, which can be expressed as:

$$m_b a_b = F_B - F_D - F_g \quad (5.18)$$

where a_b is the bubble acceleration, m_b is the bubble mass

$$m_b = \frac{4}{3} \pi R^3 \rho_b \quad (5.19)$$

here R is bubble radius, ρ_b is gas density inside the bubble), F_B is the buoyancy force

$$F_B = \frac{4}{3} \pi R^3 \rho_0 g \quad (5.20)$$

here ρ_0 is carbonated water density and , g is gravitational acceleration), F_D is the viscous drag force [194], [197],

$$F_D = 4\pi\mu Rv_b \quad (5.21)$$

here μ is the carbonated water viscosity and v_b is the bubble velocity), and F_g is the gravitational force

$$F_g = \frac{4}{3}\pi R^3 \rho_b g \quad (5.22)$$

The Reynolds number of the bubble remains low during its transition inside the droplet; hence, the Stokes' flow formulation can be adopted to estimate the drag force [194], [197]. It is worth mentioning that the weight of the bubble is much smaller than the buoyancy force because of the small gas density as compared to the surrounding fluid density displaced by the bubble during its transition. Nevertheless, it is included in Eq. 5.18 for completeness of the formulation. The inertia force, from Eq. 5.18, on the transiting gas bubble (CO_2), can be expressed as:

$$\frac{4}{3}\pi R^3 \rho_b g \cdot a_b = \frac{4}{3}\pi R^3 \rho_0 g - 4\pi\mu Rv_b - \frac{4}{3}\pi R^3 \rho_b g \quad (5.23)$$

After the rearrangement of Eq. 5.18, it yields:

$$\frac{\rho_b}{\rho_0} \cdot \frac{a_b}{g} = 1 - \frac{\rho_b}{\rho_0} - \frac{12\pi\mu R}{4\pi\rho_0 R^2 \sqrt{gR}} \cdot \frac{v_b}{\sqrt{gR}} \quad (5.24)$$

or

$$a = \frac{dv}{dt} = \frac{1-\rho}{\rho} - \frac{3\mu}{\rho_p \sqrt{gR^3}} \cdot v \quad (5.25)$$

where $\rho = \frac{\rho_b}{\rho_0}$, $a = \frac{a_b}{g}$, and $v = \frac{v_b}{\sqrt{gR}}$ are the normalized quantities.

The solution to Eq. 5.25 can be obtained incorporating the integrating factor, i.e.

$\exp\left(\int \frac{3\mu}{\rho_p \sqrt{gR^3}} dt\right)$, The solution of Eq. 5.25 yields:

$$v = \frac{\rho_p \sqrt{gR^3}}{3\mu} \left(\frac{1-\rho}{\rho} \right) + C \cdot e^{-\frac{3\mu}{\rho_p \sqrt{gR^3}} t} \quad (5.26)$$

Incorporating the boundary conditions of $v = 0$ at $t = 0$, the constant (C) can be found as:

$$C = -\frac{\rho_p \sqrt{gR^3}}{3\mu} \left(\frac{1-\rho}{\rho} \right) \quad (5.27)$$

Hence, the normalized velocity of the bubble can be expressed as:

$$v = \frac{\rho_p \sqrt{gR^3}}{3\mu} \left(\frac{1-\rho}{\rho} \right) \left(1 - e^{-\frac{3\mu}{\rho_p \sqrt{gR^3}} t} \right) \quad (5.28)$$

Buoyancy dominates over weight and drag forces, i.e. for 0.2 mm diameter bubble with 20 mm/s rising velocity, the buoyancy force is in the order of 3.29×10^{-7} N while drag and gravitational forces are in the order of 4.47×10^{-8} N and 3.94×10^{-10} N, respectively. Moreover, Eq. 5.28 remains true as the gas bubble is replaced with the oil droplet with the same size of bubble inside the carbonated water droplet. In this case, gravitational force becomes considerable depending on the specific gravity of the oil. Figure 51 shows the bubble velocity predicted from Eq. 5.28 and obtained from the experiments, when carbonated water droplet is formed on a clean hydrophobic surface, for three droplet volumes. It is worth mentioning that the bubble radius obtained from the experiments is incorporated in Eq. 5.28. As comparing the experimental findings with the results obtained from Eq. 5.28 for the bubble velocities, both results are in good agreement. The small differences are related to the texture of the hydrophobic surface, which alters the bubble formation and its departure from the hydrophobic surface. However, as comparing the average bubble velocity obtained from Eq. 5.28 and that obtained from the previous formulation [194]. the findings differ notably, i.e. the bubble velocity for the bubble

diameter of 7.89×10^{-3} mm is 0.013 mm/s while Eq. 5.28 results in 17 mm/s. It is worth mentioning that the predictions of Eq. 5.28 are almost consistent with the experimental data. On the other hand, the diffusion coefficient of CO₂ in water (carbonated water) at 20 °C is $D = 1.8 \times 10^{-9}$ m²/s [197], and the CO₂ concentration in carbonated water is $C_s = 4.53$ g/L, which corresponds to the Henry's constant of about 4.485×10^{-5} g/L.Pa. Moreover, incorporating the desorb gas (CO₂) diffusion and force balance around a bubble, the growth rate of the bubble can be approximated as:

$$\frac{dR}{dt} \sim \Lambda \left(\frac{P_L}{P_0} - 1 \right) (Dg)^{1/3} Sc^{-1/3} \quad (5.29)$$

where Sc is the Schmidt number ($Sc = \frac{\mu}{\rho D}$ and it is about 500 for the CO₂ gas bubble) [194]. Hence, the rate of bubble growth $\left(\frac{dR}{dt}\right)$ becomes 6.8×10^{-5} m/s during its departure from the hydrophobic surface in the droplet fluid. This shows a considerably small increase in the size of a single bubble in the droplet fluid. However, the experimental findings for the averaged bubble growth rate is about 5×10^{-4} m/s. The difference between the droplet growth rate is due to the previous formulation [194]. and the experimental findings can be related to the closely spaced micro/nano-cavities on the textured hydrophobic surface, i.e. some of the bubbles formed around the close texture widths can share a common surface (in contact) in the close region of the hydrophobic surface and their departure from the hydrophobic surface alters the bubble size. In addition, as two bubbles share a common surface in the close texture widths, they cannot be easily apart due to the polarization interactions. The mechanisms of two-contacting bubbles can be governed by either of the interfacial boundaries between the bubbles being destroyed and two bubbles can merge forming a large bubble, or the interfacial film remains stable and the bubbles can participate in a bubble foam. Moreover, the bubbles forming the foam-

like structure take place in the top region of the liquid droplet. This can be seen from Figure 52.a, in which a high-speed camera image of the gas bubbles (40 μL) forming the foam-like structure in the top region of the carbonated water droplet. The large bubbles formed from CO_2 gas molecules in the top section of the droplet can escape from the droplet surface (outgassing) depending on the partial pressure of CO_2 in the neighborhood ambient air. The partial pressure of CO_2 in an open atmosphere is in the order of 0.04 kPa [198]. The corresponding concentration of dissolved CO_2 ($C_{\text{eq}} = K_{\text{H}}P_{\text{CO}_2}^{\text{Atm}}$) is about 0.7×10^{-3} g/L, which is considerably small. Hence, the outgassing of CO_2 from the droplet top surface may take several hours. In addition, the bubble lifetime is governed by the draining mechanism of the film around the bubble under gravity, i.e. thinning of bubble film causes bubble-bursting due to imbalance between the pressure and the surface tension forces. The shape and the size of the bubble remain critical for tearing the bubble surface (bursting) [199]. The Bond number ($\text{Bo} = \frac{\rho g R^2}{\gamma}$ where ρ is density, g is gravity, γ is surface tension, or $\text{Bo} = \frac{R^2}{\kappa^2}$, where κ is the capillary length ($\kappa = \sqrt{\frac{\gamma}{\rho g}}$). For small diameter bubbles for which the Bond number remains much less than unity ($\text{Bo} \ll 1$), the gas bubble remains in the liquid due to surface tension domination over the gravity. As the bubble size increases so that the Bond number, the bubbles can protrude from the liquid surface. [194]. For the bubble size of 0.3 mm, the Bond number is about $\text{Bo} = 0.12$; hence a single bubble can stay at the top region of the droplet. However, as the bubble foam is formed in the top region of the carbonated water droplet (Figure 52.a), tearing of interfacial films between the attaching bubbles gradually causes the formation of a large-size bubble(s) in this region (Figure 52.b). The modeling of the

droplet bursting has been introduced previously and the solution for the small Bond number yields:

$$\frac{h}{h_0} = \left(1 + \frac{16}{\sqrt{3}} \frac{t_{rup} g \rho R}{\mu} \sqrt{\frac{h_0}{R}}\right)^{-2} \quad (5.30)$$

where h is the bubble thickness of the film onset of bursting, h_0 is the bubble film initial thickness, and t_{rup} is the bubble rupturing time [200]. Figure 52 shows the optical image of the droplet where the small CO_2 gas bubbles are forming the large bubble in the top region of the carbonated water droplet while Figure 52 shows optical images of the bubble bursting from the top surface of the droplet and after bursting, respectively. It should be noted that the optical images of the bursting bubble are obtained from a high-speed recording system. The time measured for busting of the large bubble in the droplet top region is in the order of 2.6 s and as the initial of the bubble thickness at the top of the droplet is considered to be $\sim 150 \mu\text{m}$ [201]. then, using Eq. 5.30, the resulting thinning (h/h_0) of the bubble film becomes about 0.021%. In addition, the surface evaporation can cause the thinning of the bubble formed in the top region of the droplet. The transient evaporation of the droplet surface can be approximated by incorporating the evaporation coefficient $\varphi = 25 - 19v_{air}$, here v_{air} is the air velocity above the droplet surface in m/s [202]. The amount of mass evaporated from the surface can be expressed as

$$m_{eva} = \varphi A(x_s - x)/3600 \quad (5.31)$$

here, A is droplet free surface area (m^2), x_s is the maximum humidity ratio of saturated air at the same temperature as the droplet surface ($\text{kg H}_2\text{O}$ in kg Dry Air), and x is the humidity ratio of air ($\text{kg H}_2\text{O}$ in kg Dry Air) [202]. Since the experiments were carried out in the laboratory environment at 300 K temperature, 101.325 kPa pressure, and 85% of the air relative humidity, the mass loss from 40 μL droplet is about 0.28×10^{-6} gram,

which is almost 0.7% of the total mass of the droplet. Hence, thinning of the bubble skin due to evaporation becomes considerably small. Although thinning of the bubble formed in the droplet top region is small, imbalance of forces, due to surface tension and the bubble pressure, result in the bursting of the bubble after 2.6 s of its formation.

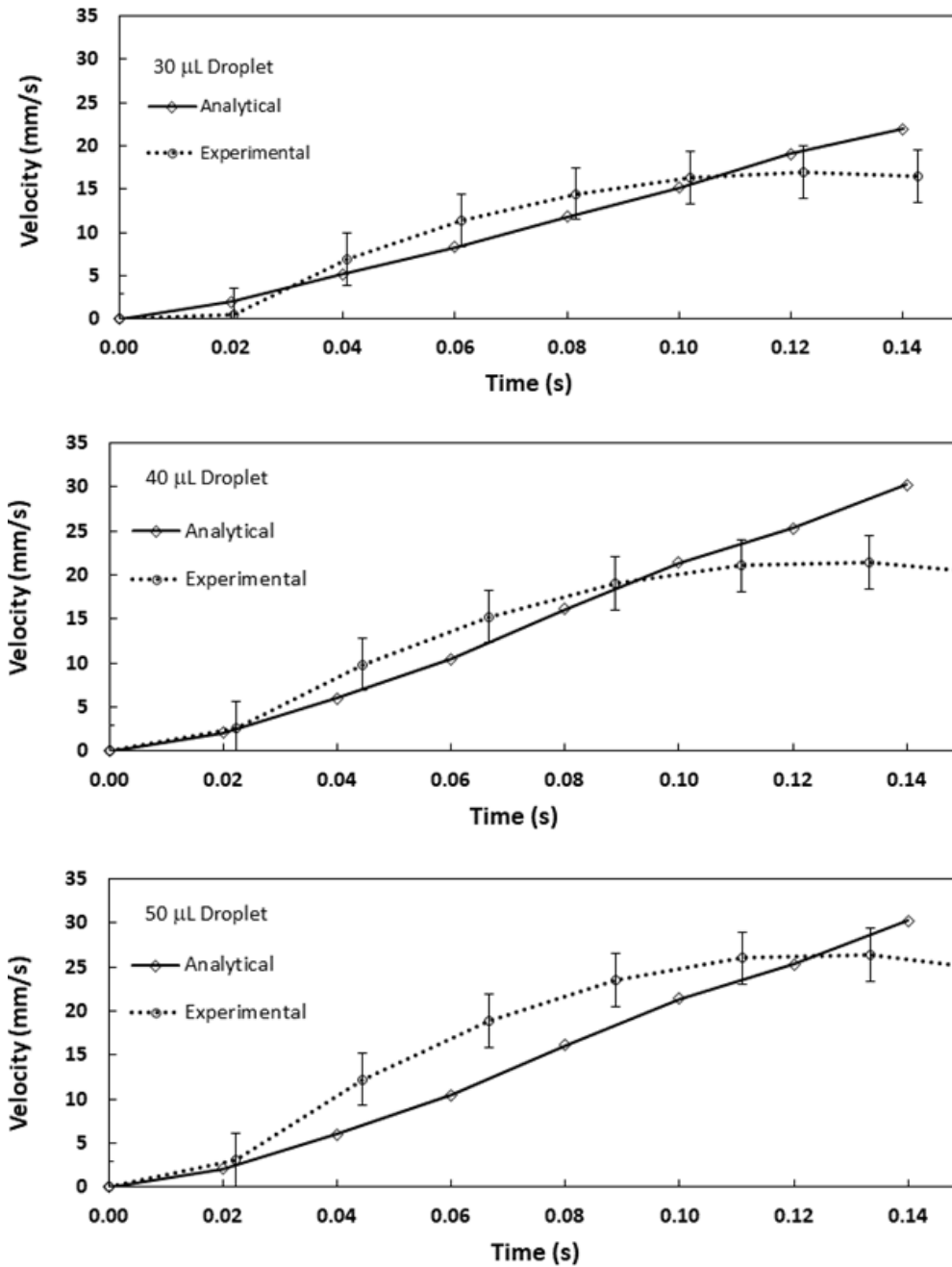


Figure 51 Bubble velocity inside the droplet predicted from analytical formulation and obtained from experiment for various droplet sizes

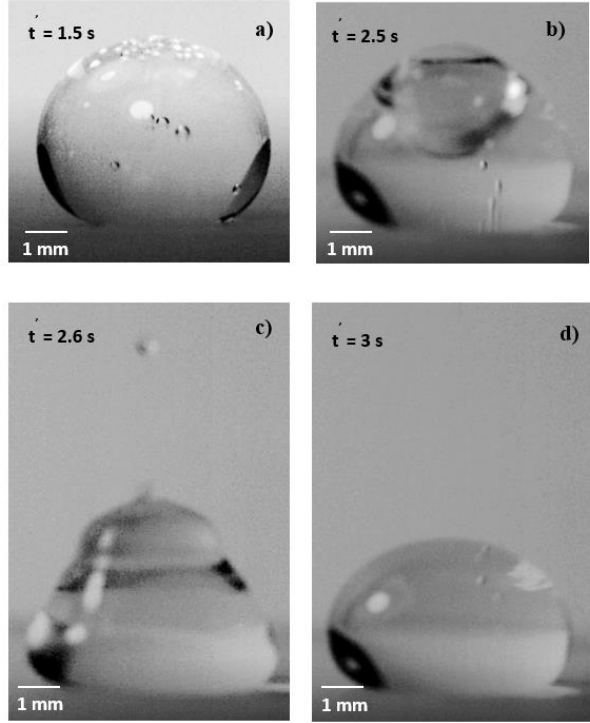


Figure 52 High-speed camera images of 40 μL bursting bubble: a) Foam-like bubbles formed in the top region of the droplet, b) large bubble is formation, c) bursting of the large bubble, and d) droplet after large bubble bursting

On the other hand, the dust particles can adhere to the hydrophobic surface under the interfacial forces (van der Waals forces). [203],[204]. The pinning force between the dust particles and the surface can be evaluated by incorporating the atomic force microscope (AFM) measurements. The deflection of the AFM probe in the friction mode can provide the pinning force data, i.e. the pinning force for the dust particle is related to $F = k\sigma_d\Delta V$, where k represents the probe tip spring constant (N/m), σ_d corresponds to the slope of the probe deflection on the friction mode ($\Delta z/\Delta V$, m/V), and ΔV is the voltage (mV) recorded from AFM due to probe deflection during the probe scanning. The AFM probe has a linear spring constant and the product of slope of the probe deflection and the probe spring constant is $k\sigma_p = 0.960908 \times 10^{-5}$ nN/mV. For an average dust particle (1.2

μm) on the hydrophobic surface, the voltage due to probe deflection is measured as ~ 21 mV. Hence, the pinning force is estimated as 20.1791×10^{-5} nN.

5.3.4 Effect of Carbonated Water on Dust Removal from the Surface

The dust particle contains elements including Ca, Na, K, Cl, S, Fe, Mg, and O and the alkaline (Na, K) and alkaline earth metal (Ca, Mg) compounds, which dissolve in water [205]. The compounds of alkaline and alkaline earth metals are non-uniformly distributed on the surface of the dust particles, which can be observed from energy dispersive spectroscopy data (Table 6). Hence, as the carbonated droplet is formed onto the dust particles, the dissolution of these compounds acts like nucleation centers for the bubble formation within the surface vicinity of the dust particles. Since the compounds of alkaline and alkaline earth metals are distributed non-uniformly on the dust surface, the location of the bubble formations becomes non-uniform on the dust surface [192]. This can be observed from Figure 53, in which the optical images of the bubbles formed on the dust particle's surface are shown. The bubbles grow with time and large bubbles are formed on the dust surface with progressing time (Figure 53). The large size bubbles attaching or emanating from the dust particles surface can cause imbalance forces acting on the dust particle while causing the reorientation of the dust particles on the hydrophobic surface (Figure 53). Hence, the balance of the forces between gravity, buoyancy, and pinning results in net force reorienting the dust particle. For the average dust particle ($1.2 \mu\text{m}$) the pinning force is estimated as $\sim 20.1791 \times 10^{-5}$ nN (as measured from AFM), and the weight of the dust particle is $\sim 18.452 \times 10^{-5}$ nN. The buoyancy force acting on the dust particle is $\sim 7.1 \times 10^{-5}$ nN (density of the dust is about 2800 kg/m^3) [186], [206], therefore, the net force required to reorient the dust particle in the

carbonated water droplet on the hydrophobic surface should be, at least, a greater or similar order of 31.531×10^{-5} nN. It is worth mentioning that pinning and gravitational force acts opposite to the buoyancy force. This indicates that the bubbles formed on the dust surface, which can reorient the dust particles, create a significant force on the dust particle located in the carbonated water on the hydrophobic surface.

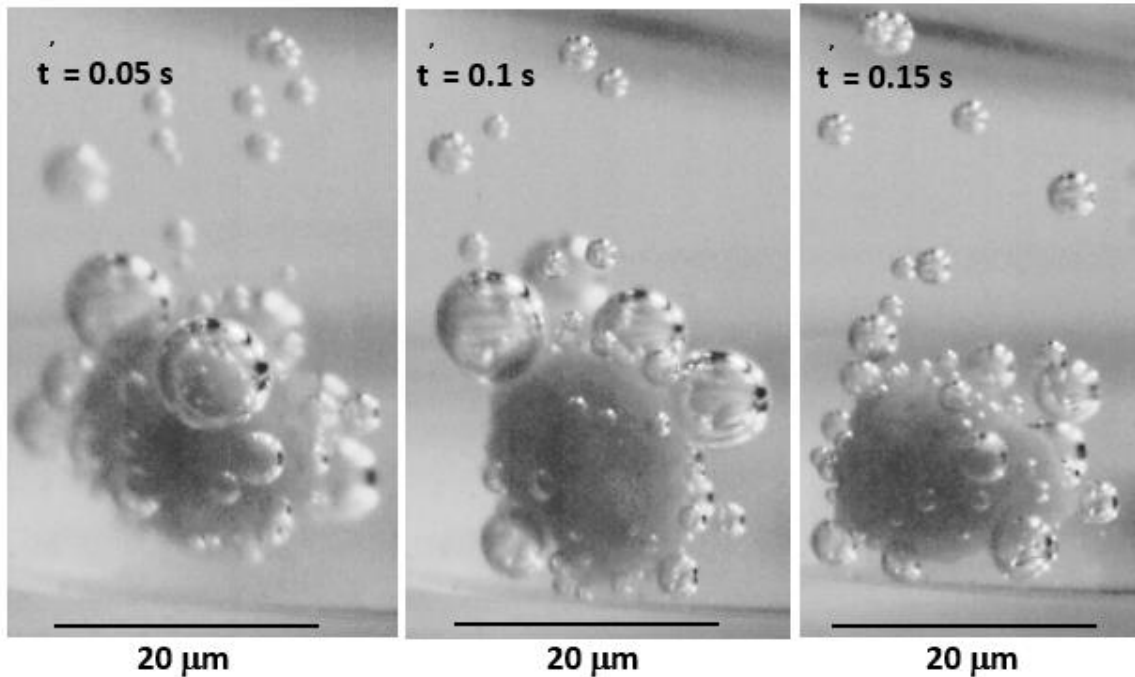


Figure 53 High-speed camera images of bubbles formed around dust particle and reorientation of dust particle due to bubble size and number changing with time on the dust particle surface

Figure 55.a and Figure 55.b show images of the water droplets, which are formed from carbonated and distilled water with the dust particles inside the droplet fluid as obtained from high-speed recording. The dust particles spread inside the droplet fluid while occupying the upper part of the droplet (close to the top surface) for carbonated water (Figure 55.a); however, the dust particles are mainly situated in the lower part of the droplet (close to the hydrophobic surface) for distilled water (Figure 55.b)). This behavior is associated with the bubbles formed around the dust particles inside the droplet for the

carbonated water. In order to assess the number of dust particles mixed with the fluid inside the droplet formed from the carbonated and distilled water, the volume occupancy of the dust particles in the droplet fluid is determined from the images of the high-speed camera records. Figure 54 shows the volume ratio of dust particles in the droplet fluid formed from carbonated and distilled water with time. The volume ratio is determined from the ratio of the volume occupied by the dust particles inside the carbonated water droplet over the volume occupied by the dust particles inside the distilled water droplet. The ratio is obtained using high-speed records. The volume ratio becomes large in the early period and the ratio reduces with increasing time. This indicates that in the early periods, the rate of bubble formation is large and several bubbles are formed in the close region of the dust particles. However, CO₂ concentration in the droplet fluid reduces with progressing time; hence, the number of new bubbles formed in the droplet fluid reduces. Since the bubbles formed in the close region of the dust particles enhance the reorientation of the dust particles on the hydrophobic surface (Figure 53.c), the influence of the bubbles on the dust particles motion is limited with the progressing time. This in turn causes a reduction in the volume ratio of the dust particles with progressing time (Figure 54).

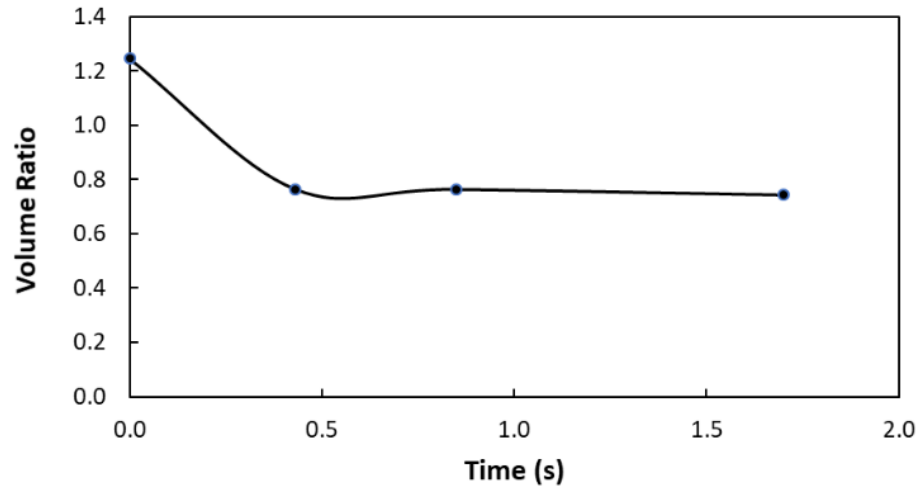


Figure 54 Volume ratio of dust particles inside the droplet. Volume ratio represents total volume occupied by dust particles in the upper part of carbonated water droplet over total volume occupied by dust particles in the upper part of the distilled water droplet

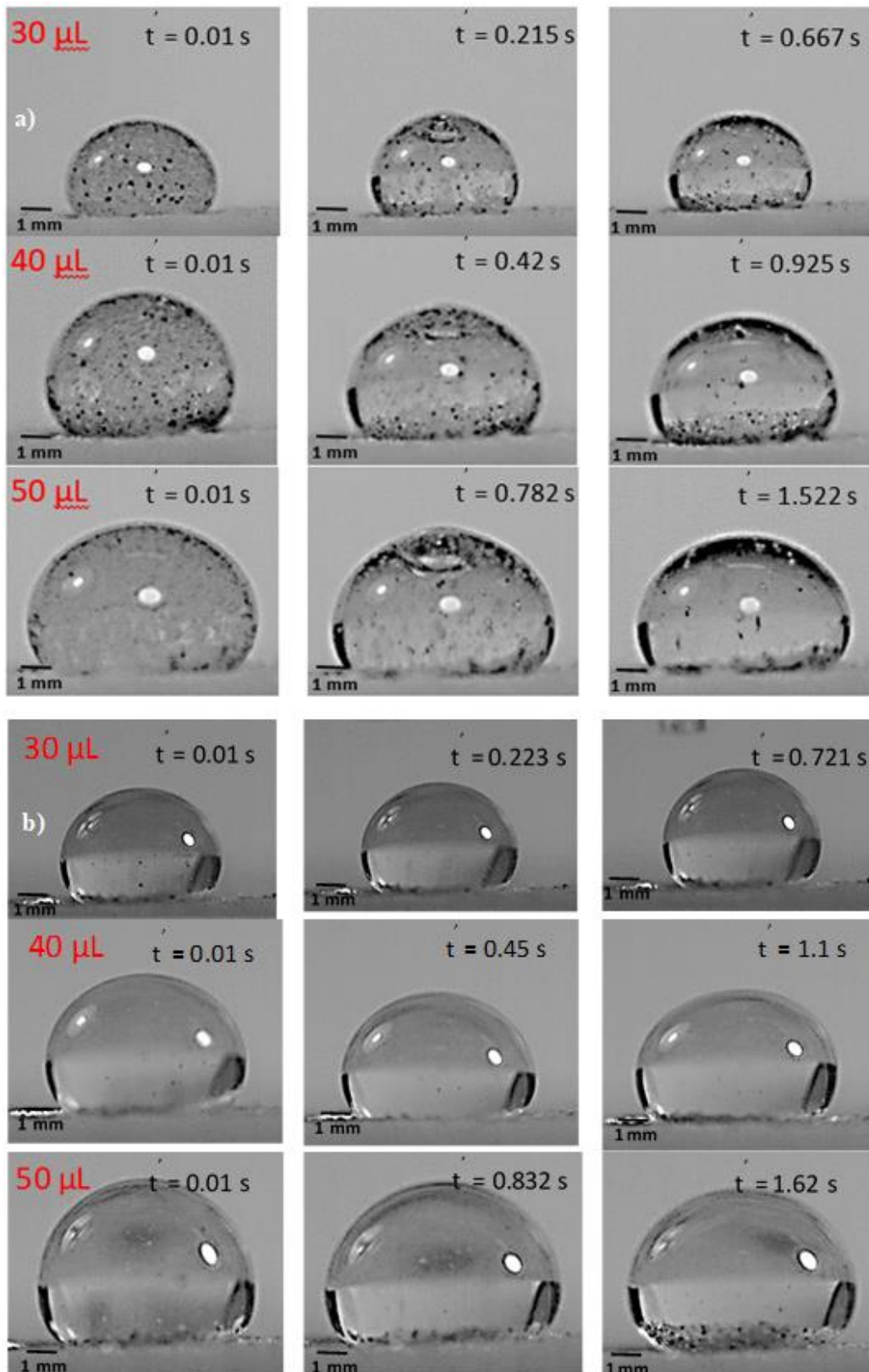


Figure 55 High-speed camera images of dust particles inside droplet: a) carbonated water droplet, and b) distilled water droplet

To assess the bubble velocity in the droplet with and without the presence of the dust particles inside the droplet, further analysis is adopted examining the high-speed recording data. A tracking program is used to determine the bubble velocity inside carbonated water droplets with and without the presence of dust particles. Figure 56.a and Figure 56.b shows the temporal behavior of the bubble velocities obtained from the cases with and without dust particles in the droplet fluid for three bubble volumes. The bubble velocity increases at a higher rate for the presence of the dust particles on the hydrophobic surface than that of the clean hydrophobic surface during the early period. The occurrence of high bubble velocity for the dusty hydrophobic surface is related to the number of initial bubble formations, which remains larger as compared to that created on the clean hydrophobic surface. This can also be seen from Figure 57.a and Figure 57.b, in which the temporal variation of the growing bubble diameter emanating from the dusty and clean hydrophobic surfaces is shown for three droplet volumes. Since the force balance for bubbles, acceleration is related to buoyancy, drag, and weight, buoyancy force becomes important particularly for large size bubbles. It is worth mentioning that the buoyancy force is related to

$$F_B \sim \frac{3}{4} \pi R_b^3 \rho_f g \quad (5.32)$$

where R_b is the radius of the bubble, ρ_f is water density and g is the gravity, while the drag force is related to Stoke's law and it takes the form

$$F_D \sim 4\pi R_b v_b \quad (5.33)$$

where v_b is the bubble velocity. Hence, the buoyancy force becomes larger than the drag force due to the large bubble diameter formed in the early periods, i.e. $F_B \sim R_b^3$ while $F_D \sim R_b$ and v_b remains low in the early periods. This gives rise to a rapid rise of the

bubble velocity in the early period. As time progresses, the bubble diameter increases for the case of the clean hydrophobic surface because of a slightly high concentration of CO₂ in the carbonated droplet fluid due to initially less desorption of CO₂ in the droplet fluid for the clean hydrophobic surface. It should be noted that on the dusty hydrophobic surface, CO₂ desorption remains high due to the dissolution of alkaline and alkaline earth metal compounds in water, which act-like nucleation centers for bubble formations. Hence, CO₂ concentration in carbonated water becomes high for clean hydrophobic surfaces and desorbing of CO₂ during bubble rising inside the droplet fluid enhances the droplet diameter for the clean hydrophobic case. This also increases the buoyancy force acting on the bubbles while causing larger bubble velocity for the clean hydrophobic surface than the dusty hydrophobic surface during the late periods (Figure 57). Figure 58 shows the dust particles velocity inside the droplet formed from carbonated and distilled water for three droplet volumes. It should be noted that the velocities of the dust particles are obtained from the tracker program while utilizing the high-speed recorded data. The velocity of the dust particles in the droplet attains higher values for the carbonated water than that corresponding to the distilled water in the early durations (< 0.1 s). This demonstrates that the bubbles formed around the dust particles contribute significantly to the dust removal from the hydrophobic surface, i.e. bubbles formed to contribute to the dust particles transition from the surface into the droplet fluid. Increasing droplet volume slightly enhances the dust particle velocity, particularly in the early periods (~ 0.025 s).

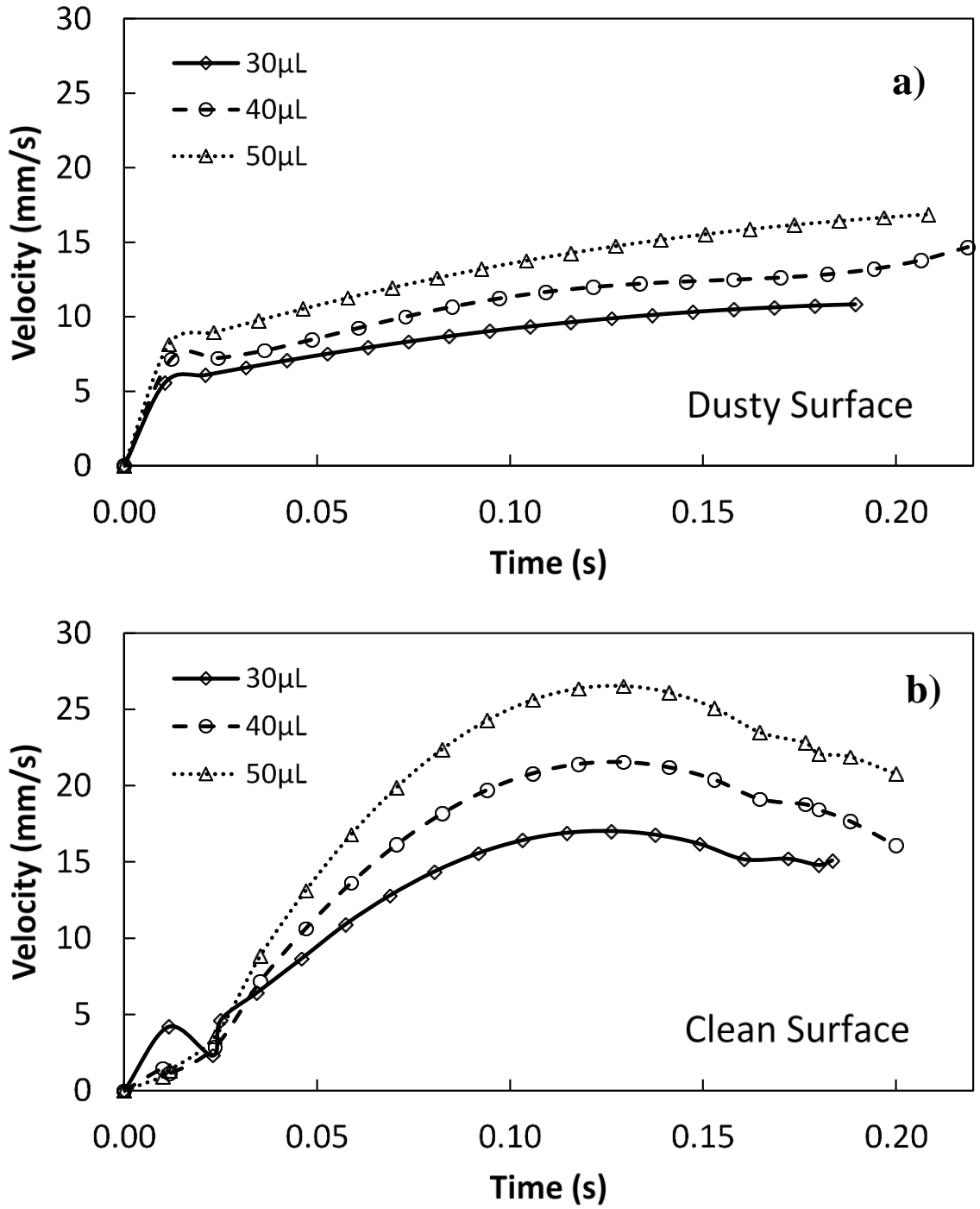


Figure 56 Bubble velocity with time for different droplet volumes: a) on dusty hydrophobic surfaces, and b) on the clean hydrophobic surface

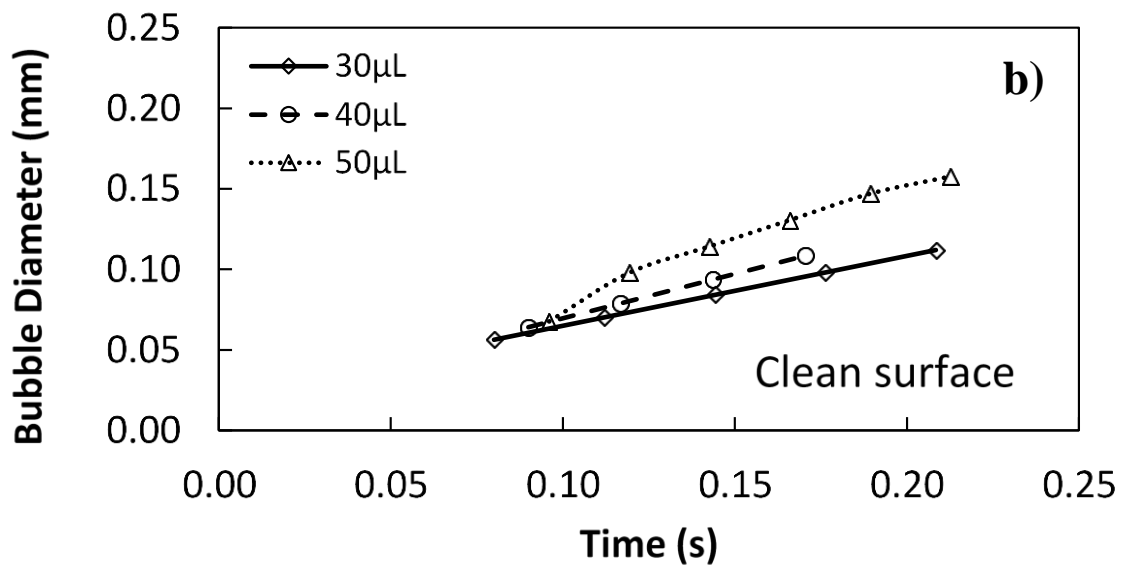
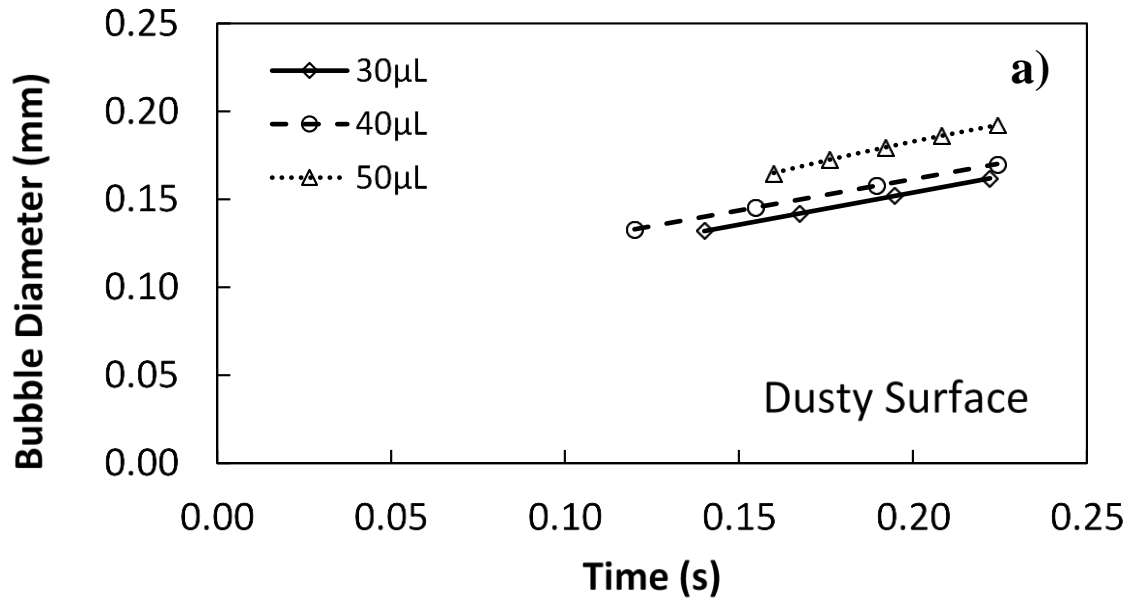


Figure 57 Bubble diameter inside droplet with time for different droplet volumes: a) a) on dusty hydrophobic surfaces and b) on the clean hydrophobic surface

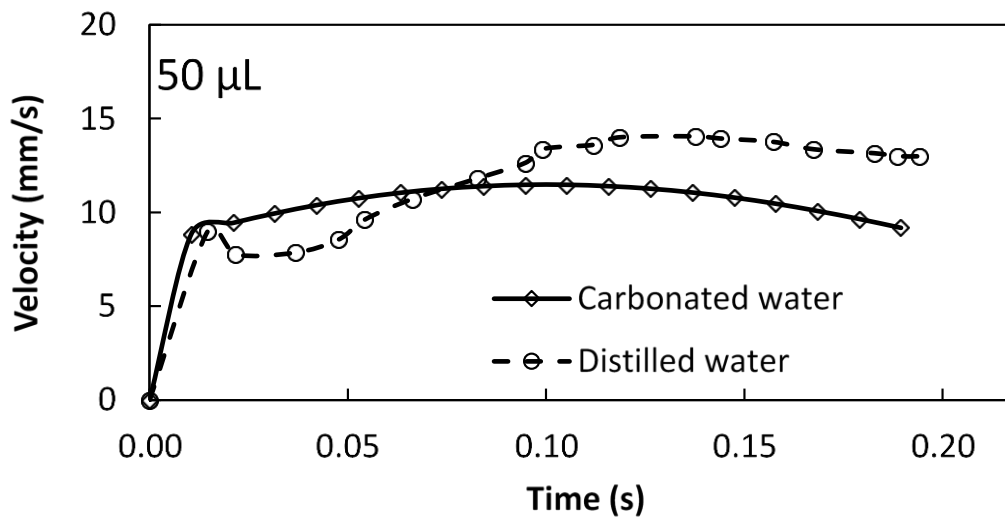
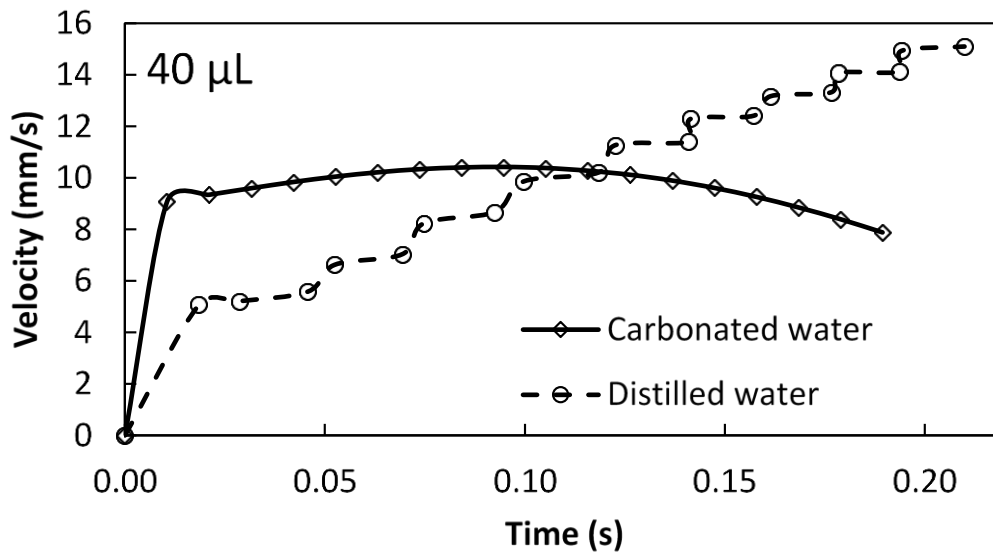
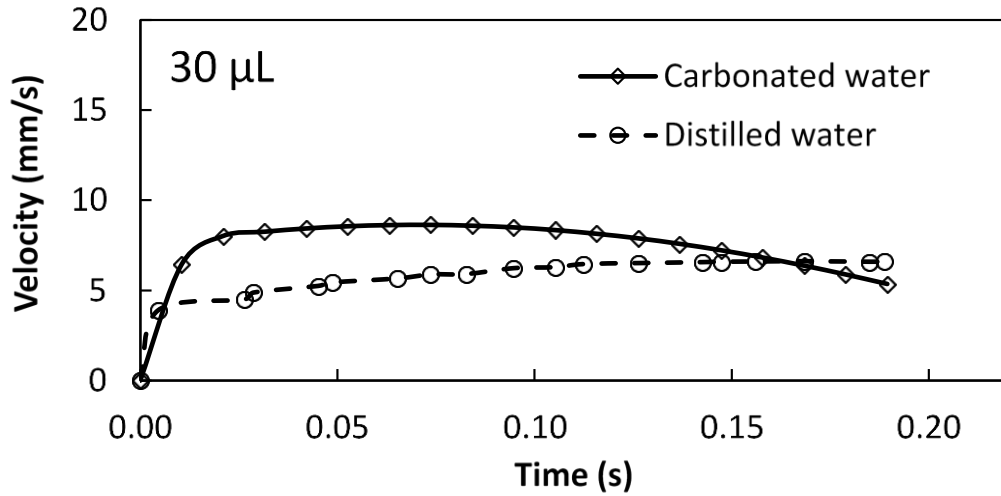


Figure 58 Dust particle velocity inside droplet with time for different carbonated and distilled water droplet volumes

CHAPTER 6

CONCLUSIONS

6.1 Dynamics of a Water Droplet on Silicone Oil Film Surfaces

Sliding water droplet on silicone oil-infused solution crystallized polycarbonate surface is examined. The polycarbonate surface is crystallized by using an acetone bath at 30% volume concentration. Silicone oil is used to impregnate the crystallized sample surface and the uniform oil film thickness of about 0.7 μm is obtained on the crystallized surface. Desalinated water droplets of 30 μL , 40 μL , and 50 μL are used to evaluate the sliding dynamics of the droplets. The high-speed recording system and tracker program are utilized to record and determine the droplet geometric appearance and droplet velocity during sliding. The findings reveal that solution crystallized polycarbonate samples possess a surface texture composed of spherules and fibrils, which give rise to the contact angle of $132^\circ \pm 4^\circ$ with hysteresis $38^\circ \pm 5^\circ$. Silicone oil impregnation improves the optical transmittance of the crystallized surface by three times for 250 nm to 500 nm wavelength range and almost 1.5 times after 500 nm to 850 nm optical spectrum. The droplet sliding on the oil film is numerically simulated using the experimental conditions and, later, predictions are validated through their counterparts of the experiments. It is observed that the sliding velocity of water droplets resulting from the simulations agrees with the data of experiments. The oil rim formed around the water droplet enlarges as the droplet slides over the film. In addition, an oil ridge is formed around the oil rim because of oil infusion on the droplet. The size of the oil ridge differs

in size at the droplet frontal and back regions. Hence, the height of the oil ridge becomes larger in the droplet frontal region than that corresponding to the back region. The height of the oil ridge also changes as the droplet slides over the oil film. The shear rate created, due to interfacial friction, and the droplet pinning, under interfacial tension, contributes to droplet behavior on the oil film. However, this effect is only about 12% of the total potential energy variation of the sliding droplet on the oil film. The gravitational influence dominates the frictional and pinning influences of the sliding droplet. A circulatory flow is created inside the sliding droplet fluid, which is related to the local shear rates created around the droplet interfaces. The peak velocity inside the droplet fluid increases as the droplet slides away from the initial sliding point on the oil surface.

6.2 Sliding Water Droplet on Oil Impregnated Surface and Dust Particle Mitigation

The sliding motion of a water droplet over a silicone oil-impregnated sample is investigated. The influence of the tilting angle of the surface, oil film thickness, and droplet size on the droplet sliding behavior is analyzed. Polycarbonate surface is solution crystallized, using 30% concentrated acetone solution, to create surface texture resulting in the hydrophobic wetting state. The solution crystallization of the surface gives rise to low optical transmittance of the samples. Silicone oil impregnation improves the optical transmittance of the samples and enables water droplets to slide over the surface. Impregnated oil film thickness influences the sliding velocity of the droplet; hence, the sliding velocity becomes lower for the small thickness oil film ($\sim 50 \mu\text{m}$) than that corresponding to the large oil film thickness ($\sim 700 \mu\text{m}$). This is related to the interfacial

resistance at the droplet bottom, i.e. slip velocity at the interface across the oil film and droplet fluid becomes small and it is also likely that the droplet bottom becomes in contact with the crystallized surface (touching) rather than floating in the oil film. As the film thickness increases, the droplet floats within the oil film, which increases the sliding velocity over the film. The oil ridges formed over the circumference of the droplet contribute adversely to the sliding over the inclined oil film due to fluid resistance occurring at the inter-boundary of the droplet fluid and the oil around the ridge sites. The dust particle located on the oil film is partially cloaked by the oil, which makes it difficult to remove by the sliding droplet. Nevertheless, the sliding droplet cloaks and removes the particle from the oil film. Once the dust particle is removed by the droplet fluid, the orientation of the dust particle inside the droplet fluid changes during the sliding. This causes the first reduction and later enhances the velocity of the droplet over the film. As the dust particle picked up settles in the trailing edge of the sliding droplet, the sliding velocity decreases gradually. In this case, the particle in the trailing edge of the droplet is partially immersed in the oil film while creating a pinning effect on the sliding droplet. Nevertheless, the pinning influence of the dust particle does not cease the droplet motion on the surface for thin oil film (50 μm); however, the droplet sliding ceases for the thick oil film (μm). The present study provides a detailed analysis of water droplet sliding behavior on the inclined oil-impregnated crystallized polycarbonate surface and explores the water droplet sliding conditions and environmental dust mitigation from the inclined oil-impregnated surface.

6.3 Carbonated Water Droplet on Dusty Hydrophobic Surfaces

Bubble behavior inside the carbonated water droplet formed on the plane and dusty hydrophobic surfaces is examined. Glass surfaces are hydrophobized via depositing functionalized silica particles. The hydrophobized surface results in a contact angle of about $150^\circ \pm 2^\circ$ with the hysteresis of $8^\circ \pm 2^\circ$. Environmental dust particles are collected and analyzed to assess the elemental composition/compounds, size distribution, and surface free energy. The average dust particle size is about $1.2 \mu\text{m}$ and dust particles have various shapes. The surface free energy of the dust is about $111.5 \pm 7.5 \text{ mJ/m}^2$ and the water spreading coefficient is $S = 28.5 \text{ mJ/m}^2$ while demonstrating that water infuses (cloaks) onto the dust particles. Carbonated water droplet forms bubbles of various sizes on the hydrophobic surface and the size of the bubbles increases as they depart from the hydrophobic surface towards the droplet fluid. The rate of size of bubble increase ($\frac{dR}{dt}$) determined from the high-speed recorded data, which is about $5 \times 10^{-4} \text{ m/s}$. As the size of the merging bubbles in the top region of the droplet increases, the bubble size increases and bursts at almost 26 s. The average velocity of the bubbles increases as the droplet size increases; in which case, the maximum bubble velocity is about 17 mm/s for 30 μL droplet and increases to almost 26 mm/s for 50 μL droplet. The number of bubbles formed on the dusty hydrophobic surface is larger than that of the clean hydrophobic surface. Since dust particles contain alkaline and alkaline earth metals, they dissolve in carbonated water while creating bubble nucleation centers in the vicinity of the dust particles. The bubble velocity remains higher for the dusty hydrophobic surface than for the clean hydrophobic surface in the early periods (0.025 s). As the bubbles transition

into the droplet fluid progresses, the bubble velocity for the clean hydrophobic surface attains larger values than that correspond to the dusty surface, i.e. it increases from 15 mm/s to 25 mm/s. This can be attributed to the CO₂ concentration in the carbonated water, which becomes high for the clean hydrophobic surface, i.e. bubble size increases in the carbonated droplet fluid so that the buoyancy force; bubble velocity increases with progressing time. In addition, the dust particles, which emanates from the hydrophobic surface and participate in the droplet fluid can cause further desorption of CO₂ in the droplet fluid while reducing CO₂ concentration in the droplet fluid and forming small size bubbles rather than enhancing the size of the previously formed bubbles in the droplet fluid, i.e. the buoyancy force remains smaller than that corresponding to those formed for the clean hydrophobic case. Some of the bubbles formed on the dust particle surface remain attached to the surface while contributing to the dust elevation from the surface via buoyancy force. The dust particle removal rate from the dusty hydrophobic surface by a droplet with the carbonated fluid is much larger than that of the droplet formed from the distilled water; hence, the volume occupied by the dust particles in the carbonated droplet fluid becomes almost 1.5 to 2.5 folds of that of the distilled water. Consequently, introducing carbonated water for forming the droplet on the dusty hydrophobic surface significantly improves the dust removal rate from the surface. This study provides insight into the bubble behavior in the droplet formed from carbonated water on the dusty hydrophobic surface and provides useful information on the comparison of the dust removal by the carbonated and distilled water droplets from the hydrophobic surface.

6.4 Future Work

The main factor in enhancing the efficiency of PV panels is increasing the incident solar light reaching the PV cell surface. The incident solar radiation suffers from the environmental surroundings, deposited dust particles, and surface characteristics of the PV panel. The environmental impact comes from the presence of suspended dust particles and water vapor in the panel surroundings which can reflect, absorb or scatter some of the incident solar radiation. This impact can be elevated by selecting a location of the PV panel where the effect of these factors is negligible. Hence, the minimization of the environmental effect of PV panel surfaces is to be studied in depth.

The dust picking mechanism can be further studied as there are many variables concerning dust deposition. The distribution and orientation of dust particles on the deposited surface are examples of such variables. Oil coating of panel surfaces can be extended to include the effect of viscosity and surface tension on the dust removal rate by a sliding droplet.

Patterning the hydrophobic surface can route the water droplet while further enhancing the dust picking efficiency. The dust picking procedure can further optimize towards minimizing the water consumption during dust removal. Carbonated water can be used to enhance dust mitigation efficiency via the creation of gas bubbles around the dust particles.

References

- [1] Statistical Review of World Energy: Energy economics: Home. (n.d.). Retrieved August 19, 2020, from <https://www.bp.com/en/global/corporate/energy-economics/statistical-review-of-world-energy.html>
- [2] Mekhilef, S., Saidur, R., & Safari, A. (2011). A review on solar energy use in industries. *Renewable and Sustainable Energy Reviews*, 15(4), 1777-1790. doi:10.1016/j.rser.2010.12.018
- [3] Grossmann, W., Steininger, K. W., Schmid, C., & Grossmann, I. (2012). Investment and employment from large-scale photovoltaics up to 2050. *Empirica*, 39(2), 165-189. doi:10.1007/s10663-012-9185-8
- [4] Saidan, M., Albaali, A. G., Alasis, E., & Kaldellis, J. K. (2016). Experimental study on the effect of dust deposition on solar photovoltaic panels in desert environment. *Renewable Energy*, 92, 499-505. doi:10.1016/j.renene.2016.02.031
- [5] Wagner, T., Neinhuis, C., & Barthlott, W. (1996). Wettability and Contaminability of Insect Wings as a Function of Their Surface Sculptures. *Acta Zoologica*, 77(3), 213-225. doi:10.1111/j.1463-6395.1996.tb01265.x
- [6] Parker, A. R., & Lawrence, C. R. (2001). Water capture by a desert beetle. *Nature*, 414(6859), 33-34. doi:10.1038/35102108
- [7] Gao, X., & Jiang, L. (2004). Water-repellent legs of water striders. *Nature*, 432(7013), 36-36. doi:10.1038/432036a
- [8] Byun, D., Hong, J., Saputra, Ko, J. H., Lee, Y. J., Park, H. C., . . . Lukes, J. R. (2009). Wetting Characteristics of Insect Wing Surfaces. *Journal of Bionic Engineering*, 6(1), 63-70. doi:10.1016/s1672-6529(08)60092-x

- [9] Koch, K., Bhushan, B., & Barthlott, W. (2008). Diversity of structure, morphology and wetting of plant surfaces. *Soft Matter*, 4(10), 1943. doi:10.1039/b804854a
- [10] Azimi, G., Dhiman, R., Kwon, H., Paxson, A. T., & Varanasi, K. K. (2013). Hydrophobicity of rare-earth oxide ceramics. *Nature Materials*, 12(4), 315-320. doi:10.1038/nmat3545
- [11] Ritchie, H., & Roser, M. (2014, March 28). Energy. Retrieved August 22, 2020, from <https://ourworldindata.org/energy>
- [12] Squires, V.R. (2007) Physics, mechanics and processes of dust and sandstorms. Adelaide University, Wikipedia, Internet data.
- [13] Sissakian, V. K., Al-Ansari, N., & Knutsson, S. (2013). Sand and dust storm events in Iraq. *Natural Science*, 05(10), 1084-1094. doi:10.4236/ns.2013.510133
- [14] Baghdad. (2020, July 21). Retrieved August 22, 2020, from <http://www.unesco.org/new/en/iraq-office/natural-sciences/water-sciences/water-in-iraq>
- [15] Potter, S. (2011). Retrospect: April 14, 1935: Black Sunday. *Weatherwise*, 64(2), 10-11. doi:10.1080/00431672.2011.551590
- [16] Hamidi, M., Kavianpour, M. R., & Shao, Y. (2013). Synoptic analysis of dust storms in the Middle East. *Asia-Pacific Journal of Atmospheric Sciences*, 49(3), 279-286. doi:10.1007/s13143-013-0027-9

- [17] Al-Ansari, N. A. (2013). Management of Water Resources in Iraq: Perspectives and Prognoses. Engineering, 05(08), 667-684. doi:10.4236/eng.2013.58080
- [18] Al-Ansari, N.A. and Knutsson, S. (2011) Toward prudent management of water resources in Iraq. Journal of Advanced Science and Engineering Research, 1, 53-67.
- [19] Al-Ansari, N.A., Knutsson, S. and Ali, A. (2012) Restoring the Garden of Eden, Iraq. Journal of Earth Science and Geotechnical Engineering, 2, 53-88
- [20] Cloughton, R. (2011) A water crisis awaits Iraq. <http://blogs.independent.co.uk/2011/10/26/a-water-crisis-awaits-iraq/>
- [21] Wilson, R. (2012) Water-shortage crisis escalating in the tigris-euphrates basin, future directions international, strategic analysis paper. [http://www.futuredirections.org.au/files/FDI_Strategic_Analysis_Paper_-_28_August_2012\(1\).pdf](http://www.futuredirections.org.au/files/FDI_Strategic_Analysis_Paper_-_28_August_2012(1).pdf)
- [22] Kami, A. (2011) Iraq may suffer clean water crisis in 15- 20 years, Reuters. <http://www.reuters.com/article/2011/09/21/iraq-water-idUSL5E7KL5YZ20110921>
- [23] Sands, P. and Latif, N. (2009) Iraq's new war is a fight for water, the national. <http://www.thenational.ae/news/world/middle-east/iraqs-new-war-is-a-fight-for-water>
- [24] IRIN (2013) IRAQ: Water shortage leads people to drink from rivers. <http://www.irinnews.org/report/70243/iraq-water-shortage-leads-people-to-drink-from-rivers>

- [25] Lorenz, F.M. (2008) Strategic water for Iraq: The need for planning and action. <http://webcache.googleusercontent.com/search?q=cache:NDIb-nCjaE-AJ:www.wcl.american.edu/journal/ilr/24/documents/Lorenz.pdf+&cd=1&hl=sv&ct=clnk&gl=se>
- [26] Raphael, N. (2009) Water crisis in Iraq: The growing danger of desertification, investors Iraq. <http://www.investorsiraq.com/showthread.php?132306-Water-Crisis-in-Iraq-The-Growing-Danger-of-Desertification>
- [27] UNESCO-Iraq (2013) Iraq's water in the International Press. <http://www.unesco.org/new/en/iraq-office/natural-sciences/water-sciences/water-in-iraq/>
- [28] Chulov, M. (2009) Water shortage threatens two million people in southern Iraq, The Gurdian. <http://www.theguardian.com/world/2009/aug/26/water-shortage-threat-iraq>
- [29] DTF (Integrated Desert Terrain Forecasting for Military Operations) (2013) Earth and ecosystem sciences. Inter- net data.
- [30] 7-Day Dust Prediction. (2020, March 03). Retrieved August 22, 2020, from <http://dafc.cimh.edu.bb/dust-prediction/>
- [31] Mani, M., & Pillai, R. (2010). Impact of dust on solar photovoltaic (PV) performance: Research status, challenges and recommendations. *Renewable and Sustainable Energy Reviews*, 14(9), 3124-3131. doi:10.1016/j.rser.2010.07.065
- [32] El-Shobokshy, M. S., & Hussein, F. M. (1993). Degradation of photovoltaic cell performance due to dust deposition on to its surface. *Renewable Energy*, 3(6-7), 585-590. doi:10.1016/0960-1481(93)90064-n

- [33] Maghami, M. R., Hizam, H., Gomes, C., Radzi, M. A., Rezadad, M. I., & Hajjghorbani, S. (2016). Power loss due to soiling on solar panel: A review. *Renewable and Sustainable Energy Reviews*, 59, 1307-1316. doi:10.1016/j.rser.2016.01.044
- [34] Syafiq, A., Pandey, A., Adzman, N., & Rahim, N. A. (2018). Corrigendum to “Advances in approaches and methods for self-cleaning of solar photovoltaic panels” [*Solar Energy* 162 (2018) 597–619]. *Solar Energy*, 165, 147. doi:10.1016/j.solener.2018.03.019
- [35] Ben-Naim, A. (1983). *Hydrophobic interactions*. New York: Plenum Press.
- [36] Akhavan, B., Jarvis, K., & Majewski, P. (2013). Hydrophobic Plasma Polymer Coated Silica Particles for Petroleum Hydrocarbon Removal. *ACS Applied Materials & Interfaces*, 5(17), 8563-8571. doi:10.1021/am4020154
- [37] Chieng, B. W., Ibrahim, N. A., Daud, N. A., & Talib, Z. A. (2019). Functionalization of Graphene Oxide via Gamma-Ray Irradiation for Hydrophobic Materials. *Synthesis, Technology and Applications of Carbon Nanomaterials*, 177-203. doi:10.1016/b978-0-12-815757-2.00008-5
- [38] Han, J. T., Xu, & Cho, K. (2005). Diverse Access to Artificial Superhydrophobic Surfaces Using Block Copolymers. *Langmuir*, 21(15), 6662-6665. doi:10.1021/la051042+
- [39] Shirtcliffe, N. J., Mchale, G., Newton, M. I., Chabrol, G., & Perry, C. C. (2004). Dual-Scale Roughness Produces Unusually Water-Repellent Surfaces. *Advanced Materials*, 16(21), 1929-1932. doi:10.1002/adma.200400315

- [40] Hwang, H. S., Lee, S. B., & Park, I. (2010). Fabrication of raspberry-like superhydrophobic hollow silica particles. *Materials Letters*, 64(20), 2159-2162. doi:10.1016/j.matlet.2010.07.031
- [41] Huang, Y., Wu, J., & Yang, S. (2011). Direct fabricating patterns using stamping transfer process with PDMS mold of hydrophobic nanostructures on surface of micro-cavity. *Microelectronic Engineering*, 88(6), 849-854. doi:10.1016/j.mee.2010.08.006
- [42] Yang, T., Tian, H., & Chen, Y. (2008). Preparation of superhydrophobic silica films with honeycomb-like structure by emulsion method. *Journal of Sol-Gel Science and Technology*, 49(2), 243-246. doi:10.1007/s10971-008-1855-4
- [43] Kinoshita, H., Ogasahara, A., Fukuda, Y., & Ohmae, N. (2010). Superhydrophobic/superhydrophilic micropatterning on a carbon nanotube film using a laser plasma-type hyperthermal atom beam facility. *Carbon*, 48(15), 4403-4408. doi:10.1016/j.carbon.2010.07.056
- [44] Lathe, S. S., Imai, H., Ganesan, V., & Rao, A. V. (2009). Superhydrophobic silica films by sol-gel co-precursor method. *Applied Surface Science*, 256(1), 217-222. doi:10.1016/j.apsusc.2009.07.113
- [45] Ma, M., Mao, Y., Gupta, M., Gleason, K. K., & Rutledge, G. C. (2005). Superhydrophobic Fabrics Produced by Electrospinning and Chemical Vapor Deposition. *Macromolecules*, 38(23), 9742-9748. doi:10.1021/ma0511189
- [46] B. S. Yilbas, M. Khaled, N. Abu-Dheir, N. Al-Aqeeli, S. A. M. Said, A. O. M. Ahmed, K. K. Varanasi, and Y. K. Toumi, "Wetting and other physical

characteristics of polycarbonate surface textured using laser ablation,” *Applied Surface Science*, vol. 320, pp. 21–29, 2014.

- [47] Zhang, X., Guo, Y., Zhang, P., Wu, Z., & Zhang, Z. (2010). Superhydrophobic CuO@Cu₂S nanoplate vertical arrays on copper surfaces. *Materials Letters*, 64(10), 1200-1203. doi:10.1016/j.matlet.2010.02.050
- [48] Yilbas, B. S., Ali, H., Al-Aqeeli, N., Khaled, M., Abu-Dheir, N., & Varanasi, K. K. (2016). Solvent-induced crystallization of a polycarbonate surface and texture copying by polydimethylsiloxane for improved surface hydrophobicity. *Journal of Applied Polymer Science*, 133(22). doi:10.1002/app.43467
- [49] Ghanem, H. M., Saq'An, S. A., Saadi, M. A., & Jawad, S. M. (2011). On the Electrical and Optical Properties of Polycarbonate /MnCl₂ Composite. *Journal of Modern Physics*, 02(12), 1553-1559. doi:10.4236/jmp.2011.212189
- [50] Grebowicz, J. S. (1996). Thermal properties of polycarbonate grade bisphenol A. *Journal of Thermal Analysis*, 46(3-4), 1151-1166. doi:10.1007/bf01983626
- [51] Sung, Y. T., Fasulo, P. D., Rodgers, W. R., Yoo, Y. T., Yoo, Y., & Paul, D. R. (2011). Properties of polycarbonate/acrylonitrile-butadiene-styrene/talc composites. *Journal of Applied Polymer Science*, 124(2), 1020-1030. doi:10.1002/app.35147

- [52] Lee, C., Kato, M., & Usuki, A. (2011). Preparation and properties of bio-based polycarbonate/clay nanocomposites. *Journal of Materials Chemistry*, 21(19), 6844. doi:10.1039/c1jm10087d
- [53] G. H. McTainsh and J. R. Pitblado, "Dust storms and related phenomena measured from meteorological records in Australia," *Earth Surf. Process. Landforms*, vol. 12, no. 4, pp. 415–424, 1987.
- [54] Gemma Shepherd, U. K. Enric Terradellas, Alexander Baklanov, S. N. William A. Sprigg, and A. A.-D. Ali Darvishi Boloorani, *Global Assessment of Sand and Dust Storms*. 2016.
- [55] H. TSOAR and K. PYE, "Dust transport and the question of desert loess formation," *Sedimentology*, vol. 34, no. 1, pp. 139–153, 1987, doi: 10.1111/j.1365-3091.1987.tb00566.x.
- [56] B. Marticorena, "Dust production mechanisms," in *Mineral Dust*, Springer, 2014, pp. 93–120.
- [57] Y. Shao, *Physics and modelling of wind erosion*, vol. 37. Springer Science & Business Media, 2008.
- [58] H. Lu and Y. Shao, "Toward quantitative prediction of dust storms: an integrated wind erosion modelling system and its applications," *Environ. Model. Softw.*, vol. 16, no. 3, pp. 233–249, 2001, doi: [https://doi.org/10.1016/S1364-8152\(00\)00083-9](https://doi.org/10.1016/S1364-8152(00)00083-9).
- [59] S. D. Kalev and G. S. Toor, "Chapter 3.9 - The Composition of Soils and Sediments," B. Török and T. B. T.-G. C. Dransfield, Eds. Elsevier, 2018, pp. 339–357.

- [60] I. Yolcubal, M. L. Brusevay, J. F. Artiola, P. Wierenga, and L. G. Wilson, "12 - ENVIRONMENTAL PHYSICAL PROPERTIES AND PROCESSES," J. F. Artiola, I. L. Pepper, and M. L. B. T.-E. M. and C. Brusevay, Eds. Burlington: Academic Press, 2004, pp. 207–239.
- [61] P. W. Unger and T. M. McCalla, "Conservation tillage systems," in *Advances in Agronomy*, vol. 33, Elsevier, 1980, pp. 1–58.
- [62] K. Deneff and J. Six, "Clay mineralogy determines the importance of biological versus abiotic processes for macroaggregate formation and stabilization," *Eur. J. Soil Sci.*, vol. 56, no. 4, pp. 469–479, 2005.
- [63] S. Chatterjee, K. K. Bandyopadhyay, S. Pradhan, R. Singh, and S. P. Datta, "Effects of irrigation, crop residue mulch and nitrogen management in maize (*Zea mays* L.) on soil carbon pools in a sandy loam soil of Indo-gangetic plain region," *Catena*, vol. 165, pp. 207–216, 2018.
- [64] R. L. Blevins and W. W. Frye, "Conservation Tillage: An Ecological Approach to Soil Management," vol. 51, D. L. B. T.-A. in A. Sparks, Ed. Academic Press, 1993, pp. 33–78.
- [65] R. L. Baumhardt and R. C. Schwartz, "CRUSTS | Structural," D. B. T.-E. of S. in the E. Hillel, Ed. Oxford: Elsevier, 2005, pp. 347–356.
- [66] J. E. Bullard et al., "Preferential dust sources: A geomorphological classification designed for use in global dust-cycle models," *J. Geophys. Res. Earth Surf.*, vol. 116, no. F4, 2011.
- [67] N. Middleton, "The Human Impact," in *Arid Zone Geomorphology: Process, Form and Change in Drylands*, 2011, pp. 569–581.

- [68] N. M. Mahowald et al., “Observed 20th century desert dust variability: Impact on climate and biogeochemistry,” *Atmos. Chem. Phys.*, vol. 10, no. 22, pp. 10875–10893, 2010, doi: 10.5194/acp-10-10875-2010.
- [69] T. Stanelle, I. Bey, T. Raddatz, C. Reick, and I. Tegen, “Anthropogenically induced changes in twentieth century mineral dust burden and the associated impact on radiative forcing,” *J. Geophys. Res.*, vol. 119, no. 23, pp. 13,513–526,546, 2014, doi: 10.1002/2014JD022062.
- [70] S. A. M. Said and H. M. Walwil, “Fundamental studies on dust fouling effects on PV module performance,” *Sol. Energy*, vol. 107, pp. 328–337, 2014.
- [71] G. A. Mastekbayeva and S. Kumar, “Effect of dust on the transmittance of low density polyethylene glazing in a tropical climate,” *Sol. Energy*, vol. 68, no. 2, pp. 135–141, 2000.
- [72] J. K. Kaldellis and A. Kokala, “Quantifying the decrease of the photovoltaic panels’ energy yield due to phenomena of natural air pollution disposal,” *Energy*, vol. 35, no. 12, pp. 4862–4869, 2010.
- [73] M. J. Adinoyi and S. A. M. Said, “Effect of dust accumulation on the power outputs of solar photovoltaic modules,” *Renew. energy*, vol. 60, pp. 633–636, 2013.
- [74] S. Boppana, *Outdoor soiling loss characterization and statistical risk analysis of photovoltaic power plants*. Arizona State University, 2015.
- [75] L. Boyle, H. Flinchpaugh, and M. P. Hannigan, “Natural soiling of photovoltaic cover plates and the impact on transmission,” *Renew. Energy*, vol. 77, pp. 166–173, 2015.

- [76] A. A. Hegazy, "Effect of dust accumulation on solar transmittance through glass covers of plate-type collectors," *Renew. energy*, vol. 22, no. 4, pp. 525–540, 2001.
- [77] L. Boyle, H. Flinchpaugh, and M. Hannigan, "Assessment of PM dry deposition on solar energy harvesting systems: measurement–model comparison," *Aerosol Sci. Technol.*, vol. 50, no. 4, pp. 380–391, 2016.
- [78] R. Appels et al., "Effect of soiling on photovoltaic modules," *Sol. energy*, vol. 96, pp. 283–291, 2013.
- [79] H. Jiang, L. Lu, and K. Sun, "Experimental investigation of the impact of airborne dust deposition on the performance of solar photovoltaic (PV) modules," *Atmos. Environ.*, vol. 45, no. 25, pp. 4299–4304, 2011.
- [80] J. J. John, S. Warade, G. Tamizhmani, and A. Kottantharayil, "Study of soiling loss on photovoltaic modules with artificially deposited dust of different gravimetric densities and compositions collected from different locations in India," *IEEE J. photovoltaics*, vol. 6, no. 1, pp. 236–243, 2015.
- [81] performance of photovoltaic generators," *J. Clean. Prod.*, vol. 19, no. 4, pp. 311–317, 2011.
- [82] J. K. Kaldellis, P. Fragos, and M. Kapsali, "Systematic experimental study of the pollution deposition impact on the energy yield of photovoltaic installations," *Renew. Energy*, vol. 36, no. 10, pp. 2717–2724, 2011.
- [83] J. K. Kaldellis and M. Kapsali, "Simulating the dust effect on the energy performance of photovoltaic generators based on experimental measurements," *Energy*, vol. 36, no. 8, pp. 5154–5161, 2011.

- [84] T. Khatib, H. Kazem, K. Sopian, F. Buttinger, W. Elmenreich, and A. S. Albusaidi, "Effect of dust deposition on the performance of multi-crystalline photovoltaic modules based on experimental measurements," *Int. J. Renew. Energy Res.*, vol. 3, no. 4, pp. 850–853, 2013.
- [85] S. A. Sulaiman, H. H. Hussain, N. Leh, and M. S. I. Razali, "Effects of Dust on the Performance of PV Panels," *World Acad. Sci. Eng. Technol.*, vol. 58, no. 2011, pp. 588–593, 2011.
- [86] Z. A. Darwish, H. A. Kazem, K. Sopian, M. A. Al-Goul, and H. Alawadhi, "Effect of dust pollutant type on photovoltaic performance," *Renew. Sustain. Energy Rev.*, vol. 41, pp. 735–744, 2015.
- [87] M. N. Horenstein, M. K. Mazumder, R. C. Sumner, J. Stark, T. Abuhamed, and R. Boxman, "Modeling of trajectories in an electrodynamic screen for obtaining maximum particle removal efficiency," *IEEE Trans. Ind. Appl.*, vol. 49, no. 2, pp. 707–713, 2013.
- [88] C. E. Johnson, P. K. Srirama, R. Sharma, K. Pruessner, J. Zhang, and M. K. Mazumder, "Effect of particle size distribution on the performance of electrodynamic screens," in *Fortieth IAS Annual Meeting. Conference Record of the 2005 Industry Applications Conference, 2005.*, 2005, vol. 1, pp. 341–345.
- [89] L. L. Kazmerski et al., "Fundamental studies of adhesion of dust to PV module surfaces: Chemical and physical relationships at the microscale," *IEEE J. Photovoltaics*, vol. 6, no. 3, pp. 719–729, 2016.
- [90] M. K. Mazumder et al., "Environmental degradation of the optical surface of PV modules and solar mirrors by soiling and high RH and mitigation methods

for minimizing energy yield losses,” in 2015 IEEE 42nd Photovoltaic Specialist Conference (PVSC), 2015, pp. 1–6.

- [91] Y. Kim et al., “Effects of relative humidity and particle and surface properties on particle resuspension rates,” *Aerosol Sci. Technol.*, vol. 50, no. 4, pp. 339–352, 2016.
- [92] D. J. Quesnel et al., “Aspects of particle adhesion and removal,” in *Developments in Surface Contamination and Cleaning*, Elsevier, 2016, pp. 119–145.
- [93] M. S. El-Shobokshy and F. M. Hussein, “Effect of dust with different physical properties on the performance of photovoltaic cells,” *Sol. energy*, vol. 51, no. 6, pp. 505–511, 1993.
- [94] S. Pulipaka, F. Mani, and R. Kumar, “Modeling of soiled PV module with neural networks and regression using particle size composition,” *Sol. Energy*, vol. 123, pp. 116–126, 2016.
- [95] B. Weber, A. Quiñones, R. Almanza, and M. D. Duran, “Performance reduction of PV systems by dust deposition,” *Energy Procedia*, vol. 57, pp. 99–108, 2014.
- [96] J. Tanesab, D. Parlevliet, J. Whale, T. Urmee, and T. Pryor, “The contribution of dust to performance degradation of PV modules in a temperate climate zone,” *Sol. Energy*, vol. 120, pp. 147–157, 2015.
- [97] M. Mani and R. Pillai, “Impact of dust on solar photovoltaic (PV) performance: Research status, challenges and recommendations,” *Renew. Sustain. energy Rev.*, vol. 14, no. 9, pp. 3124–3131, 2010.

- [98] W. Javed, Y. Wubulikasimu, B. Figgis, and B. Guo, "Characterization of dust accumulated on photovoltaic panels in Doha, Qatar," *Solar Energy*, vol. 142, pp. 123–135, 2017, doi: 10.1016/j.solener.2016.11.053.
- [99] M. Saidan, A. G. Albaali, E. Alasis, and J. K. Kaldellis, "Experimental study on the effect of dust deposition on solar photovoltaic panels in desert environment," *Renew. Energy*, vol. 92, pp. 499–505, 2016.
- [100] R. K. Jones et al., "Optimized cleaning cost and schedule based on observed soiling conditions for photovoltaic plants in central Saudi Arabia," *IEEE J. photovoltaics*, vol. 6, no. 3, pp. 730–738, 2016.
- [101] E. Lorenzo, *Solar electricity: engineering of photovoltaic systems*. Earthscan/James & James, 1994.
- [102] M. A. Hamdan and B. A. Kakish, "Solar radiation attenuation caused by atmospheric pollution," *Energy Convers. Manag.*, vol. 36, no. 2, pp. 121–124, 1995.
- [103] P. Denholm, "Solar energy: The largest energy resource. Generating Electricity in a Carbon-Constrained World, FP Sioshansi, ed." Academic Press, California, 2010.
- [104] N. Beattie, R. Moir, S. Roberts, G. Buffoni, P. Graham, and N. Pearsall, "Sand and dust accumulation on photovoltaic modules in dry regions," 2011.
- [105] G. Codato, A. P. Oliveira, and J. F. Escobedo, "Comparative study of solar radiation in urban and rural areas," 2004.
- [106] W. Tian, Y. Wang, J. Ren, and L. Zhu, "Effect of urban climate on building integrated photovoltaics performance," *Energy Convers. Manag.*, vol. 48,

no. 1, pp. 1–8, 2007.

- [107] E. Jauregui and E. Luyando, “Global radiation attenuation by air pollution and its effects on the thermal climate in Mexico City,” *Int. J. Climatol. A J. R. Meteorol. Soc.*, vol. 19, no. 6, pp. 683–694, 1999.
- [108] S. M. Robaa, “A study of ultraviolet solar radiation at Cairo urban area, Egypt,” *Sol. energy*, vol. 77, no. 2, pp. 251–259, 2004.
- [109] E. Asl-Soleimani, S. Farhangi, and M. S. Zabihi, “The effect of tilt angle, air pollution on performance of photovoltaic systems in Tehran,” *Renew. Energy*, vol. 24, no. 3–4, pp. 459–468, 2001.
- [110] A. S. Sánchez, E. Cohim, and R. A. Kalid, “A review on physicochemical and microbiological contamination of roof-harvested rainwater in urban areas,” *Sustain. Water Qual. Ecol.*, vol. 6, pp. 119–137, 2015.
- [111] D. Rekioua and E. Matagne, *Optimization of photovoltaic power systems: modelization, simulation and control*. Springer Science & Business Media, 2012.
- [112] S. Mekhilef, R. Saidur, and M. Kamalisarvestani, “Effect of dust, humidity and air velocity on efficiency of photovoltaic cells,” *Renew. Sustain. energy Rev.*, vol. 16, no. 5, pp. 2920–2925, 2012.
- [113] A. J. Arnfield, “Two decades of urban climate research: a review of turbulence, exchanges of energy and water, and the urban heat island,” *Int. J. Climatol. a J. R. Meteorol. Soc.*, vol. 23, no. 1, pp. 1–26, 2003.
- [114] A. M. El-Nashar, “The effect of dust accumulation on the performance of evacuated tube collectors,” *Sol. Energy*, vol. 53, no. 1, pp. 105–115, 1994.
- [115] A. Whelan, *Polymer technology dictionary*. Springer Science & Business

Media, 2012.

- [116] C. W. Johnson, D. L. Timmons, and P. E. Hall, *Essential laboratory mathematics: concepts and applications for the chemical and clinical laboratory technician*. Cengage Learning, 2003.
- [117] H. K. Elminir, A. E. Ghitas, R. H. Hamid, F. El-Hussainy, M. M. Beheary, and K. M. Abdel-Moneim, "Effect of dust on the transparent cover of solar collectors," *Energy Convers. Manag.*, vol. 47, no. 18–19, pp. 3192–3203, 2006.
- [118] D. Goossens and E. Van Kerschaever, "Aeolian dust deposition on photovoltaic solar cells: the effects of wind velocity and airborne dust concentration on cell performance," *Sol. energy*, vol. 66, no. 4, pp. 277–289, 1999.
- [119] J. Zang and Y. Wang, "Analysis of computation model of particle deposition on transmittance for photovoltaic panels," *Energy Procedia*, vol. 12, pp. 554–559, 2011.
- [120] M. Mazumder et al., "Characterization of electrodynamic screen performance for dust removal from solar panels and solar hydrogen generators," *IEEE Trans. Ind. Appl.*, vol. 49, no. 4, pp. 1793–1800, 2013.
- [121] J. Y. Hee, L. V. Kumar, A. J. Danner, H. Yang, and C. S. Bhatia, "The effect of dust on transmission and self-cleaning property of solar panels," *Energy Procedia*, vol. 15, pp. 421–427, 2012.
- [122] J. Zorrilla-Casanova, "Analysis of dust losses in photovoltaic modules/Zorrilla-Casanova J," 2011.
- [123] E. Cuddihy, C. Coulbert, A. Gupta, and R. Liang, "Electricity from

photovoltaic solar cells: flat-plate solar array project final report. Volume VII: Module encapsulation,” 1986.

- [124] F. M. Zaihidee, S. Mekhilef, M. Seyedmahmoudian, and B. Horan, “Dust as an unalterable deteriorative factor affecting PV panel’s efficiency: Why and how,” *Renewable and Sustainable Energy Reviews*, vol. 65. pp. 1267–1278, 2016, doi: 10.1016/j.rser.2016.06.068.
- [125] H. Khonkar et al., “Importance of cleaning concentrated photovoltaic arrays in a desert environment,” *Sol. Energy*, vol. 110, pp. 268–275, 2014.
- [126] M. A. M. Ramli, E. Prasetyono, R. W. Wicaksana, N. A. Windarko, K. Sedraoui, and Y. A. Al-Turki, “On the investigation of photovoltaic output power reduction due to dust accumulation and weather conditions,” *Renew. Energy*, vol. 99, pp. 836–844, 2016, doi: 10.1016/j.renene.2016.07.063.
- [127] S. S. and S. Darvekar, “Solar Photovoltaic Panels Cleaning Methods A Review,” *Int. J. Pure Appl. Math.*, vol. 118, pp. 1–17, May 2018.
- [128] S. Nishimoto and B. Bhushan, “Bioinspired self-cleaning surfaces with superhydrophobicity, superoleophobicity, and superhydrophilicity,” *Rsc Adv.*, vol. 3, no. 3, pp. 671–690, 2013.
- [129] S. Mekhilef, R. Saidur, and M. Kamalisarvestani, “Effect of dust , humidity and air velocity on efficiency of photovoltaic cells,” *Renew. Sustain. Energy Rev.*, vol. 16, no. 5, pp. 2920–2925, 2012, doi: 10.1016/j.rser.2012.02.012.
- [130] D. Goossens, Z. Y. Offer, and A. Zangvil, “Wind tunnel experiments and field investigations of eolian dust deposition on photovoltaic solar collectors,”

vol. 50, no. 1, pp. 75–84, 1993.

- [131] D. Goossens and E. V. A. N. Kerschaever, “Eolian dust deposition on photovoltaic solar cells: the effects of wind velocity and airborne dust concentration on cell performance,” vol. 66, no. 4, pp. 277–289, 1999.
- [132] G. He, C. Zhou, and Z. Li, “Review of self-cleaning method for solar cell array,” *Procedia Eng.*, vol. 16, pp. 640–645, 2011.
- [133] M. K. Mazumder, R. Sharma, A. S. Biris, J. Zhang, C. Calle, and M. Zahn, “Self-cleaning transparent dust shields for protecting solar panels and other devices,” *Part. Sci. Technol.*, vol. 25, no. 1, pp. 5–20, 2007.
- [134] L. Cao, “Superhydrophobic Surface Design Fabrication and Application,” *Engineering*, p. 111, 2010.
- [135] M. Jang, C. K. Park, and N. Y. Lee, “Modification of polycarbonate with hydrophilic/hydrophobic coatings for the fabrication of microdevices,” *Sensors Actuators B Chem.*, vol. 193, pp. 599–607, 2014.
- [136] G. Soliveri, V. Sabatini, H. Farina, M. A. Ortenzi, D. Meroni, and A. Colombo, “Double side self-cleaning polymeric materials: The hydrophobic and photoactive approach,” *Colloids Surfaces A Physicochem. Eng. Asp.*, vol. 483, pp. 285–291, 2015.
- [137] M. Jiang, J. Liu, S. Wang, M. Lv, and X. Zeng, “Surface modification of bisphenol A polycarbonate using an ultraviolet laser with high-speed, direct-writing technology,” *Surf. Coatings Technol.*, vol. 254, pp. 423–428, 2014.
- [138] Y. Zhou, Y. Dan, L. Jiang, and G. Li, “The effect of crystallization on hydrolytic stability of polycarbonate,” *Polym. Degrad. Stab.*, vol. 98, no. 8, pp.

1465–1472, 2013.

- [139] S. D. Bhagat and M. C. Gupta, “Superhydrophobic microtextured polycarbonate surfaces,” *Surf. Coatings Technol.*, vol. 270, pp. 117–122, 2015.
- [140] I. Saarikoski, M. Suvanto, and T. A. Pakkanen, “Modification of polycarbonate surface properties by nano-, micro-, and hierarchical micro–nanostructuring,” *Appl. Surf. Sci.*, vol. 255, no. 22, pp. 9000–9005, 2009.
- [141] D. Yu, Y. Zhao, H. Li, H. Qi, B. Li, and X. Yuan, “Preparation and evaluation of hydrophobic surfaces of polyacrylate-polydimethylsiloxane copolymers for anti-icing,” *Prog. Org. Coatings*, vol. 76, no. 10, pp. 1435–1444, 2013.
- [142] C. K. Söz, E. Yilgör, and I. Yilgör, “Influence of the average surface roughness on the formation of superhydrophobic polymer surfaces through spin-coating with hydrophobic fumed silica,” *Polymer (Guildf.)*, vol. 62, pp. 118–128, 2015.
- [143] Y.-H. Huang, J.-T. Wu, and S.-Y. Yang, “Direct fabricating patterns using stamping transfer process with PDMS mold of hydrophobic nanostructures on surface of micro-cavity,” *Microelectron. Eng.*, vol. 88, no. 6, pp. 849–854, 2011.
- [144] X. Liu, Y. Xu, K. Ben, Z. Chen, Y. Wang, and Z. Guan, “Transparent, durable and thermally stable PDMS-derived superhydrophobic surfaces,” *Appl. Surf. Sci.*, vol. 339, pp. 94–101, 2015.
- [145] R. Kohli and K. L. Mittal, *Developments in Surface Contamination and Cleaning, Volume 4: Detection, Characterization, and Analysis of Contaminants*. William Andrew, 2011.

- [146] P. G. C. Petean and M. L. Aguiar, “Determining the adhesion force between particles and rough surfaces,” *Powder Technol.*, vol. 274, pp. 67–76, 2015, doi: 10.1016/j.powtec.2014.12.047.
- [147] P. S. R. Beeram, “Characterization of ice adhesion strength over different surfaces pertinent to aircraft anti-/de-icing,” 2017.
- [148] G. Whyman, E. Bormashenko, and T. Stein, “The rigorous derivation of Young, Cassie--Baxter and Wenzel equations and the analysis of the contact angle hysteresis phenomenon,” *Chem. Phys. Lett.*, vol. 450, no. 4, pp. 355–359, 2008.
- [149] M. Ambrosia and C.-H. Lee, “A Study of a Hydrophobic Surface: Comparing Pure Water and Contaminated Water,” *J. Environ. Sci. Int.*, vol. 22, Apr. 2013, doi: 10.5322/JESI.2013.22.4.407.
- [150] Bhattacharya, S., Charonko, J. J., and Vlachos, P. P., 2018, “Particle Image Velocimetry (PIV) Uncertainty Quantification Using Moment of Correlation (MC) Plane,” *Meas. Sci. Technol.*, 29(11), p. 115301.
- [151] Smith, J. D., Dhiman, R., Anand, S., Reza-Garduno, E., Cohen, R. E., McKinley, G. H., and Varanasi, K. K., 2013, “Droplet Mobility on Lubricant-Impregnated Surfaces,” *Soft Matter*, 9(6), pp. 1772–1780.
- [152] Al-Sharafi, A., Yilbas, B. S., and Hassan, G., 2019, “Droplet on Oil Impregnated Surface: Temperature and Velocity Fields,” *Int. J. Therm. Sci.*, 146, p. 106054.
- [153] Schwartz, L. W., 1989, “Viscous Flows down an Inclined Plane: Instability and Finger Formation,” *Phys. Fluids A Fluid Dyn.*, 1(3), pp. 443–445.
- [154] Ruyer-Quil, C., and Manneville, P., 1998, “Modeling Film Flows down

- Inclined Planes,” *Eur. Phys. J. B-Condensed Matter Complex Syst.*, 6(2), pp. 277–292.
- [155] Alfrey Jr, T., Gurnee, E. F., and Lloyd, W. G., 1966, “Diffusion in Glassy Polymers,” *Journal of Polymer Science Part C: Polymer Symposia*, Wiley Online Library, pp. 249–261.
- [156] Sanopoulou, M., and Stamatialis, D. F., 2001, “Study of the Transition from Fickian to Case II Sorption Kinetics in the System Poly (Ethyl Methacrylate)–Liquid Methyl Alcohol,” *Polymer (Guildf.)*, 42(4), pp. 1429–1439.
- [157] Brandrup, J., Immergut, E. H., Grulke, E. A., Abe, A., and Bloch, D. R., 1999, *Polymer Handbook*, Wiley New York.
- [158] Van Krevelen, D. W., and Te Nijenhuis, K., 2009, *Properties of Polymers: Their Correlation with Chemical Structure; Their Numerical Estimation and Prediction from Additive Group Contributions*, Elsevier.
- [159] Ng, C.-O., and Wang, C. Y., 2010, “Apparent Slip Arising from Stokes Shear Flow over a Bidimensional Patterned Surface,” *Microfluid. Nanofluidics*, 8(3), pp. 361–371.
- [160] Cao, Z., Stevens, M. J., Carrillo, J.-M. Y., and Dobrynin, A. V., 2015, “Adhesion and Wetting of Soft Nanoparticles on Textured Surfaces: Transition between Wenzel and Cassie–Baxter States,” *Langmuir*, 31(5), pp. 1693–1703.
- [161] Peng, M., Kurokawa, T., Gong, J. P., Osada, Y., and Zheng, Q., 2002, “Effect of Surface Roughness of Hydrophobic Substrate on Heterogeneous Polymerization of Hydrogels,” *J. Phys. Chem. B*, 106(12), pp. 3073–3081.
- [162] Yang, S.-M., 1987, “Motions of a Sphere in a Time-Dependent Stokes

- Flow: A Generalization of Faxen's Law," Korean J. Chem. Eng., 4(1), pp. 15–22.
- [163] Lauritzen Jr, J. I., and Hoffman, J. D., 1960, "Theory of Formation of Polymer Crystals with Folded Chains in Dilute Solution," J. Res. Natl. Bur. Stand. Sect. A, Phys. Chem., 64(1), p. 73.
- [164] Frank, F. C., and Tosi, M., 1961, "On the Theory of Polymer Crystallization," Proc. R. Soc. London. Ser. A. Math. Phys. Sci., 263(1314), pp. 323–339.
- [165] Lafuma, A., and Quéré, D., 2011, "Slippery Pre-Suffused Surfaces," EPL (Europhysics Lett., 96(5), p. 56001.
- [166] Oss, C. J. van, Good, R. J., and Busscher, R. J., 1990, "Estimation of the Polar Surface Tension Parameters of Glycerol and Formamide, for Use in Contact Angle Measurements on Polar Solids," J. Dispers. Sci. and Technology, 11(1), pp. 75–81.
- [167] Van Oss, C. J., Chaudhury, M. K., and Good, R. J., 1988, "Interfacial Lifshitz-van Der Waals and Polar Interactions in Macroscopic Systems," Chem. Rev., 88(6), pp. 927–941.
- [168] El-Hamouz, A., 2007, "Effect of Surfactant Concentration and Operating Temperature on the Drop Size Distribution of Silicone Oil Water Dispersion," J. Dispers. Sci. Technol., 28(5), pp. 797–804.
- [169] Ricci, E., Sangiorgi, R., and Passerone, A., 1986, "Density and Surface Tension of Dioctylphthalate, Silicone Oil and Their Solutions," Surf. Coatings Technol., 28(2), pp. 215–223.
- [170] Lauritzen Jr, J.I.; Hoffman, J.D. Theory of formation of polymer crystals

- with folded chains in dilute solution. *J. Res. Natl. Bur. Stand. Sect. A, Phys. Chem.* 1960, 64, 73.
- [171] Kim, D.; Pugno, N.M.; Ryu, S. Wetting theory for small droplets on textured solid surfaces. *Sci. Rep.* 2016, 6, 37813.
- [172] Anand, S.; Rykaczewski, K.; Subramanyam, S.B.; Beysens, D.; Varanasi, K.K. How droplets nucleate and grow on liquids and liquid impregnated surfaces. *Soft Matter* 2015, 11, 69–80, doi:10.1039/c4sm01424c.
- [173] Yilbas, B.S.; Ali, H.; Al-Aqeeli, N.; Khaled, M.; Abu-Dheir, N.; Varanasi, K.K. Solvent-induced crystallization of a polycarbonate surface and texture copying by polydimethylsiloxane for improved surface hydrophobicity. *J. Appl. Polym. Sci.* 2016, 133.
- [174] Ricci, E.; Sangiorgi, R.; Passerone, A. Density and surface tension of dioctylphthalate, silicone oil and their solutions. *Surf. Coatings Technol.* 1986, 28, 215–223.
- [175] Smith, J.D.; Dhiman, R.; Anand, S.; Reza-Garduno, E.; Cohen, R.E.; McKinley, G.H.; Varanasi, K.K. Droplet mobility on lubricant-impregnated surfaces. *Soft Matter* 2013, 9, 1772–1780, doi:10.1039/C2SM27032C.
- [176] Hassan, G.; Yilbas, B.S.; Al-Qahtani, H. Droplet fluid infusion into a dust layer in relation to self-cleaning. *RSC Adv.* 2020, 10, 32034–32042, doi:10.1039/d0ra05700b.
- [177] Bergeron, V.; Langevin, D. Monolayer spreading of polydimethylsiloxane oil on surfactant solutions. *Phys. Rev. Lett.* 1996, 76, 3152.
- [178] Carlson, A.; Kim, P.; Amberg, G.; Stone, H.A. Short and long time drop

- dynamics on lubricated substrates. *EPL (Europhysics Lett.* 2013, 104, 34008.
- [179] Schwartz, L.W. Viscous flows down an inclined plane: Instability and finger formation. *Phys. Fluids A Fluid Dyn.* 1989, 1, 443–445.
- [180] Ng, C.-O.; Wang, C.Y. Apparent slip arising from Stokes shear flow over a bidimensional patterned surface. *Microfluid. Nanofluidics* 2010, 8, 361–371.
- [181] Yang, S.-M. Motions of a sphere in a time-dependent stokes flow: A generalization of Faxen's law. *Korean J. Chem. Eng.* 1987, 4, 15–22.
- [182] W. Y. D. Yong, Z. Zhang, G. Cristobal and W. S. Chin, *Colloids Surfaces A Physicochem. Eng. Asp.*, 2014, 460, 151–157.
- [183] C. J. Van Oss, R. J. Good and M. K. Chaudhury, *J. Chromatogr. A*, 1987, 391, 53–65.
- [184] B. Jańczuk, W. Wójcik and A. Zdziennicka, *J. Colloid Interface Sci.*, 1993, 157, 384–393.
- [185] B. S. Yilbas, H. Ali, N. Al-Aqeeli, M. M. Khaled, S. Said, N. Abu-Dheir, N. Merah, K. Youcef-Toumi and K. K. Varanasi, *Sci. Rep.*, 2016, 6, 24308.
- [186] S. Chandra and C. T. Avedisian, *Proc. R. Soc. London. Ser. A Math. Phys. Sci.*, 1991, 432, 13–41.
- [187] C. J. van Oss, R. J. Good and R. J. Busscher, *J. Dispers. Sci. andTechnology*, 1990, 11, 75–81.
- [188] B. S. Yilbas, G. Hassan, A. Al-Sharafi, H. Ali, N. Al-Aqeeli and A. Al-Sarkhi, *Sci. Rep.*, 2018, 8, 2984.
- [189] D. J. Preston, Y. Song, Z. Lu, D. S. Antao, and E. N. Wang, *ACS Appl. Mater. Interfaces*, 2017, 9, 42383-42392.

- [190] D. Kim, N. M. Pugno and S. Ryu, *Sci. Rep.*, 2016, 6, 37813.
- [191] S. Anand, K. Rykaczewski, S. B. Subramanyam, D. Beysens and K. K. Varanasi, *Soft Matter*, 2015, 11, 69–80.
- [192] V. Bergeron and D. Langevin, *Phys. Rev. Lett.*, 1996, 76, 3152.
- [193] A. Carlson, P. Kim, G. Amberg and H. A. Stone, *EPL (Europhysics Lett.)*, 2013, 104, 34008.
- [194] R. Zenit and J. Rodríguez-Rodríguez, *arXiv Prepr. arXiv1810.04733*.
- [195] B. M. Smirnov and R. S. Berry, *Chem. Cent. J.*, 2015, 9, 48.
- [196] R. Clift, J.R. Grace, and M.E. Weber, *Bubbles, Drops, and Particles*, Academic Press, New York, 1st edn, 1978.
- [197] E. I. Nedderman, *A-to-Z Guid. to Thermodyn. Heat Mass Transf. Fluids Eng.*
- [198] G. Liger-Belair, in *Trends in Non-alcoholic Beverages*, Elsevier, 2020, pp. 37–62.
- [199] M. A. C. Teixeira, S. Arscott, S. J. Cox and P. I. C. Teixeira, *Langmuir*, 2015, 31, 13708–13717.
- [200] P. D. Howell, *J. Eng. Math.*, 1999, 35, 251–272.
- [201] S. K. Watson, Z. Han, W. W. Su, M. A. Deshusses and E. Kan, *Environ. Technol.*, 2016, 37, 3186–3192.
- [202] A.-T. Chai and V. S. Arpaci, in *NASA Conference Publication, NASA*, 1994, p. 141.
- [203] K. Cooper, A. Gupta and S. Beaudoin, *J. Colloid Interface Sci.*, 2001, 234, 284–292.

- [204] A. Al-Sharafi, B. S. Yilbas, H. Ali and A. Z. Sahin, *Numer. Heat Transf. Part A Appl.*, 2016, 70, 1118–1140.
- [205] G. Abdelmagid, B. S. Yilbas, A. Al-Sharafi, H. Al-Qahtani and N. Al-Aqeeli, *RSC Adv.*, 2019, 9, 3582–3596.
- [206] J.-H. Hao and Z.-J. Wang, *J. Dispers. Sci. Technol.*, 2016, 37, 1208–1213.

Vitae

Name :Saeed Abobakr Bahatab

Nationality :Yemeni

Date of Birth :11/18/1991

Email :Saeedbahatab@gmail.com

Address :KFUPM, Dhahran 31261, Saudi Arabia

Academic Background : MS Mechanical Engineering

December 2021

King Fahd University of Petroleum and Minerals

Dharan 31261, Saudi Arabia

BS Mechanical Engineering

January 2016

King Fahd University of Petroleum and Minerals

Dharan 31261, Saudi Arabia

2021:

1. Sliding Water Droplet on Oil Impregnated Surface and Dust Particle Mitigation

Authors: Bahatab, S; Yilbas, BS; Abubakar, AA; Hassan, G; Mohammed, AS; Al-Qahtani, H; Sahin, AZ; Al-Sharafi, A

Wide Category: Biochemistry & Molecular Biology; Chemistry, Multidisciplinary

Q Class: Q2 | **IF:** 4.411 | **Journal:** MOLECULES

2. Solution Crystallization of Polycarbonate Surfaces for Hydrophobic State: Water Droplet Dynamics and Life Cycle Assessment towards Self-Cleaning Applications

Authors: Yilbas, BS; Abubakar, AA; Al-Qahtani, H; Shuja, SZ; Shaukat, MM; Sahin, AZ; Al-Sharafi, A; Bahatab, S

Wide Category: Polymer Science

Q Class: Q1 | **IF:** 4.329 | **Journal:** POLYMERS

3. Experimental and Model Studies of Various Size Water Droplet Impacting on a Hydrophobic Surface

Authors: Abubakar, AA; Yilbas, BS; A-Qahtani, MH; Hassan, G; Yakubu, M; Bahatab, S; Adukwu, JAE

Wide Category: Engineering, Mechanical

Q Class: Q3 | **IF:** 1.995 | **Journal:** JOURNAL OF FLUIDS ENGINEERING-TRANSACTIONS OF THE ASME

4. Sliding Dynamics of a Water Droplet on Silicone Oil Film Surface

Authors: Yilbas, BS; Mohammed, AS; Abubakar, AA; Bahatab, S; Al-Qahtani, H; Al-Sharafi, A

Wide Category: Engineering, Mechanical

Q Class: Q3 | **IF:** 1.995 | **Journal:** JOURNAL OF FLUIDS ENGINEERING-TRANSACTIONS OF THE ASME

2020:

5. A water droplet-cleaning of a dusty hydrophobic surface: influence of dust layer thickness on droplet dynamics

Authors: Hassan, G; Yilbas, BS; Bahatab, S; Al-Sharafi, A; Al-Qahtani, H

Wide Category: Multidisciplinary Sciences

Q Class: Q1 | **IF:** 4.379 | **Journal:** SCIENTIFIC REPORTS

6. Carbonated water droplets on a dusty hydrophobic surface

Authors: Abubakar, AA; Yilbas, BS; Al-Qahtani, H; Hassan, G; Yakubu, M; Hatab, SB

Wide Category: Chemistry, Physical; Materials Science, Multidisciplinary; Physics, Multidisciplinary; Polymer Science

Q Class: Q2 | **IF:** 3.679 | **Journal:** SOFT MATTER

7. Dust removal from a hydrophobic surface by rolling fizzy water droplets

Authors: Yilbas, BS; Hassan, G; Al-Qahtani, H; Bahatab, S; Sahin, AZ; Al-Sharafi, A; Abubakar, AA

Wide Category: Chemistry, Multidisciplinary

Q Class: Q2 | **IF:** 3.361 | **Journal:** RSC ADVANCES

2019:

8. Environmental Dust Particles Repelling from A Hydrophobic Surface under Electrostatic Influence

Authors: Yilbas, BS; Al-Qahtani, H; Al-Sharafi, A; Bahatab, S; Hassan, G; Al-Aqeeli, N; Kassas, M

Wide Category: Multidisciplinary Sciences

Q Class: Q1 | **IF:** 3.998 | **Journal:** SCIENTIFIC REPORTS

|